ISBN 978-82-471-2034-7 (printed ver.)
ISBN 978-82-471-2036-1 (electronic ver.)
ISSN 1503-8181

Doctoral theses at NTNU, 2010:40

Øystein Olsen

Analysis of Manganese Enhanced MRI of the Normal and Injured Rat Central Nervous System

Doctoral Thesis

Øystein Olsen

Doctoral theses at NTNU, 2010:40

NTNU

NTNU
Norwegian University of
Science and Technology
Thesis for the degree of
philosophiae doctor
Faculty of Medicine
Department of Circulation and Medical Imaging

NTNU
Norwegian University of
Science and Technology

NTNU
Norwegian University of
Science and Technology

Øystein Olsen

Analysis of Manganese Enhanced MRI of the Normal and Injured Rat Central Nervous System

Thesis for the degree of philosophiae doctor

Trondheim, March 2010

Norwegian University of
Science and Technology
Faculty of Medicine
Department of Circulation and Medical Imaging

NTNU
Norwegian University of
Science and Technology

NTNU
Norwegian University of Science and Technology

Thesis for the degree of philosophiae doctor

Faculty of Medicine
Department of Circulation and Medical Imaging

ISBN 978-82-471-2034-7 (printed ver.)
ISBN 978-82-471-2036-1 (electronic ver.)
ISSN 1503-8181

Doctoral Theses at NTNU, 2010:40

Printed by Tapir Uttrykk

Analyse av manganforsterket MRI av sentralnervesystemet til rotte med og uten skade

Skader eller sykdom i sentralnervesystemet som f.eks. ved hjerneslag eller Alzheimers sykdom kan ofte ikke helbredes, og pasienter med slike tilstander har dårlige prognoser. To viktige faktorer ved denne typen skader og sykdom er sentralneversystemets manglende evne til regenerering, samt endringer i transport langs nervebanene. Blant flere sykdommer i sentralnervesystemet er feil i nervebanenes (aksonenes) transportmekanisme den underliggende årsaken til sykdommen. Selv om nerver i sentralnervesystemet ikke repareres etter skade slik som i det perifere nervesystemet finnes det eksperimentelle metoder som fremmer regenerasjon. Det er viktig å studere disse mekanisme i dyremodeller før man overfører behandlingsmetoder til mennesker.

MR-avbildning (MRI) er en teknikk som gjør det mulig å studere sentralnervesystemet over tid uten å gjøre operative inngrep, i motsetning til tradisjonelle metoder hvor man i dyreforsøk ofte må avlive dyrene før man tar vevsprøver som analyseres. Mangan (Mn^{2+}) er et paramagnetisk ion som hovedsaklig reduserer T_1-relaksasjonstiden i vev og dermed øker kontrasten i T_1-vektede MR bilder. I tillegg kan mangan komme inn i nerveceller gjennom nervecellenes kalsiumkanaler og bli transportert langs aksonene. Dette gjør mangan velegnet til å studere celler og nervebaner i sentralnervesystemet. Denne teknikken, hvor man bruker mangan som et MR kontrastmiddel, er ofte omtalt som manganforsterket MRI (MEMRI).

I dette PhD arbeidet er det utviklet metoder for å segmentere aksoner og hjernevev med mangan i MR bilder samt metoder for å kvantifisere signal- og kontrastendringer langs nervebanene. Synsnerven og hjernen til rotte er brukt som eksperimentmodell for sentralnervesystemet.

I første del av arbeidet ble en metode for segmentering og beregning av MR-bildekontrast langs den manganforsterkede synsnerven er utviklet. Metoden gjør det mulig å se hvordan mangan fordeles langs nerven og hvor transporten av mangan eventuelt stopper opp. Denne metoden ble brukt til å detektere regenerasjon av aksoner i synsnerven etter skade ved hjelp av MRI og etter stimulering av gjenvekst. Videre ble mekanismene for tilførsel og transport av mangan i aksonene undersøkt. Resultatene tyder på at tilførselen er uavhengig av konsentrasjon over et visst nivå samt at mangan transporteres med en rekke hastigheter i friske aksoner. Studier av hvordan denne hastighetsfordelingen endres ved sykdom kan gi verdifull informasjon om sykdomsutvikling og eventuell respons på behandling. Til slutt i arbeidet ble en billedanalytisk metode for sammenligning av MEMRI og korresponderende histologi av hjerneslag hos nyfødte rotter utviklet. Resultatene fra denne studien tyder på at mangan akkumuleres i deler av hjernen etter slag som en følge av aktiviserte glia celler.

Metodene som er utviklet i dette arbeidet har bidratt til å gi en dypere kunnskap om hvordan mangan kommer inn i og transporteres langs nervebanene. I tillegg har de forbedret teknikkene for å studere regenerasjon av nerver i sentralnervesystemet og tolke betydningen av akkumulasjon av mangan i hjernevev i forbindelse med hjerneslag hos nyfødte rotter. Dette har betydning for videre studier i dyremodeller hvor det endelige målet er å utvikle behandling for mennesker.

Øystein Olsen

Institutt for sirkulasjon og bildediagnostikk.
Veiledere: Olav Haraldseth, Christian Brekken og Pål Erik Goa.

Overnevnte avhandling er funnet verdig til å forsvares offentlig for graden Philosophiae Doctor i medisinsk teknologi.

Disputasen finner sted i MTA, Medisinsk-teknisk forskningssenter, fredag 19. mars 2010 kl 12:15.

Acknowledgments

This thesis is the result of my work in partial fulfillment of the degree of Philosophiae Doctor carried out at the Department of Circulation and Medical Imaging, Faculty of Medicine, Norwegian University of Science and Technology (NTNU). Financial support was provided by Sør-Trøndelag University College (HiST).

First of all, I would like to thank my supervisors; Professor Olav Haraldseth, Dr Christian Brekken and Dr Pål Erik Goa for inviting me to participate in an exciting project and for their ideas and advice. Their complementary roles have been of great importance for the success of this project. Furthermore, I would like to thank Dr Marte Thuen, MD Marius Widerøe and Tina Bugge Pedersen for outstanding work regarding the animal experiments and Dr Anders Kristoffersen for fruitful discussions and help on model simulations. A special thanks goes to Professor Maria Petrou and Dr Vassili Kovalev for their help at my stay at the University of Surrey. Their initial ideas and suggestions on image processing have been of great importance for this project. I would also like to thank all my co-authors of the papers in this thesis. I am very grateful for their contributions.

Thanks also to all my colleagues at the MR-centre, FUGE Molecular Imaging Center Trondheim and HiST for providing a positive working environment and to encourage me to continue during times when the data looked crap, writing was difficult and reviews merciless. Finally, thanks to my family at home for letting me do this and giving me the life I appreciate so much.

Øystein Olsen,

Trondheim, november 2009

Summary

Injury or disease in the central nervous system (CNS) such as stroke or Alzheimer's disease is often irreversible, thus patients suffering from such injuries or diseases have poor prognosis. Important factors in CNS injury and disease are absence of axonal regeneration and axonal transport disturbances. Axons in the mammalian CNS do not regenerate after injury but few experimental procedures have shown to promote CNS regeneration. In some neurodegenerative diseases failure in the axonal transport system is the underlying cause of the disease. Studies of these mechanisms in animal models are important before translating any treatments to humans. Magnetic resonance imaging (MRI) is a non-invasive imaging technique which allows *in vivo* longitudinal CNS studies in contrast to traditional methods which requires sacrificing the animals before tissue sampling and microscopic analysis of neurons. Manganese (Mn^{2+}) is a paramagnetic ion which reduces the T_1-relaxation time, thus increases tissue contrast in T_1-weighted MR images. In addition, Mn^{2+} enters neurons through voltage gated calcium channels and is transported along neural axons which make Mn^{2+} well suited as a contrast agent in MRI studies of the CNS and neural pathways.

In this PhD-thesis methods for segmentation of axons and brain tissue with Mn^{2+} accumulation together with methods for quantification of signal- and contrast changes along axons related to Mn^{2+} accumulation and transport have been established. The rat optic nerve (ON) and brain was chosen as experimental models for the mammalian CNS. A method for semi-automatic segmentation of the manganese enhanced rat ON and calculation of contrast variation along the ON was developed in Paper I. In Paper II, this method was used to *in vivo* detect ON axon regeneration after injury and axon re-growth stimulation. In Paper III, the transport kinetics of Mn^{2+} in the healthy rat ON was investigated. The results indicate that input of Mn^{2+} into axons is restricted and are transported along the ON axons in a wide range of velocities. In Paper IV, a method for comparison of manganese enhanced MRI and corresponding histology of stroke in the perinatal period was developed. The methods have enabled more reliable *in vivo* studies of axonal damage and repair in parts of the CNS and provided more profound knowledge about axonal manganese transport kinetics, as well as novel insight into the relationship between manganese enhancement and neural death related to ischemic insult in the neonatal brain.

Symbols and abbreviations

α	flip angle
b	diffusion weighting factor
Ca^{2+}	calcium ion
CNR	contrast-to-noise ratio
CNS	central nervous system
d	days
δ	temporal width of diffusion gradients
Δ	temporal spacing between diffusion gradients
dpl	days past lesion
DTI	diffusion tensor imaging
EPI	echo planar imaging
FLASH	fast low angle shot
FOV	field of view
Gd^{3+}	gadolinium ion
h	hour
HI	hypoxic-ischemic injury
MEMRI	manganese-enhanced magnetic resonance imaging
min	minutes
Mn^{2+}	manganese ion
$MnCl_2$	manganese chloride
MnDPDP	manganese dipyridoxyl diphosphate
MR	magnetic resonance
MRI	magnetic resonance imaging

MSME	multi-slice multi-echo
ON	optic nerve
ONC	optic nerve crush
PNG	peripheral nerve graft
ρ	proton density
RGC	retinal ganglion cells
ROI	region of interest
SD	standard deviation
SE	spin echo
SI	signal intensity
SNR	signal-to-noise ratio
T_1	time constant for spin-lattice relaxation
T_2	time constant for spin-spin relaxation
T_2*	time constant for effective spin-spin relaxation
TD	saturation recovery delay
TE	echo time
TR	repetition time

List of papers

Paper I
Axon tracing in the adult rat optic nerve and tract after intravitreal injection of MnDPDP using a semi-automatic segmentation technique

Øystein Olsen, Marte Thuen, Martin Berry, Vassili Kovalev, Maria Petrou, Pål Erik Goa, Axel Sandvig, Olav Haraldseth, and Christian Brekken.
Journal of Magnetic Resonance Imaging 27:34–42, 2008

Paper II
Combination of Mn^{2+}-enhanced and diffusion tensor MR imaging gives complementary information about injury and regeneration in the adult rat optic nerve

Marte Thuen, Øystein Olsen, Martin Berry, Tina Bugge Pedersen, Anders Kristoffersen, Olav Haraldseth, Axel Sandvig, and Christian Brekken.
Journal of Magnetic Resonance Imaging 29(1):39-51, 2009

Paper III
Manganese transport in the rat optic nerve evaluated with spatial- and time-resolved MRI

Øystein Olsen, Anders Kristoffersen, Marte Thuen, Axel Sandvig, Christian Brekken, Olav Haraldseth, Pål Erik Goa.
Submitted to Journal of Magnetic Resonance Imaging

Paper IV
Manganese-enhanced magnetic resonance imaging of hypoxic-ischemic brain injury in the neonatal rat

Marius Widerøe, Øystein Olsen, Tina Bugge Pedersen, Pål Erik Goa, Annemieke Kavelaars, Cobi Heijnen, Jon Skranes, Ann-Mari Brubakk, Christian Brekken.
Neuroimage 45(3):880-90 2009

Contents

Symbols and abbreviations ix

List of papers xi

1 Introduction 1
1.1 Clinical background . . . 1
1.2 Animal models . . . 2
1.2.1 Rat optic nerve . . . 2
1.2.2 Neonatal rat brain . . . 2
1.3 Axonal transport . . . 2
1.4 Manganese-enhanced MRI . . . 3
1.4.1 Properties of manganese . . . 3
1.4.2 Contrast agents . . . 4
1.4.3 Image sequences . . . 4
1.5 Image processing . . . 5
1.5.1 Mathematical morphology . . . 5
1.5.2 Image segmentation . . . 6
1.5.3 Image registration . . . 7
1.5.4 Model optimization . . . 7

2 Aims of study 9

3 Materials and Methods 11
3.1 Animal models . . . 11
3.1.1 Animal handling . . . 11
3.1.2 Contrast agent injections . . . 11
3.1.3 CNS injury . . . 11
3.2 MRI . . . 12
3.2.1 T_1-weighted MRI . . . 12
3.2.2 T_2-maps . . . 13
3.2.3 Diffusion tensor imaging . . . 13
3.3 Data analysis . . . 13
3.3.1 Optic nerve segmentation . . . 13
3.3.2 Axonal Mn^{2+} transport model optimization . . . 14

3.3.3 Segmentation of manganese enhanced areas in the ischemic brain . . . 14
3.3.4 Histology . . . 14
3.3.5 Segmentation of stained areas in the histology images . . . 15
3.3.6 Image registration . . . 15
3.3.7 Statistical analysis . . . 15

4 Summary of papers **17**

5 General discussion **21**
5.1 Main findings . . . 21
5.2 Methodological considerations . . . 22
5.3 Intracellular manganese . . . 25
5.4 Conclusion . . . 26

Bibliography **28**

Chapter 1

Introduction

1.1 Clinical background

Injury in the central nervous system (CNS) often results in paralysis and permanent loss of function. CNS damage occurs in traumatic injuries such as brain trauma, hypoxic-ischemic injury (HI) and neurodegenerative diseases such as Alzheimer's disease and Parkinson's disease. Few clinical treatments are currently available which means that for those suffering from CNS injury or disease, many will experience loss in quality of life and in many cases CNS injury or disease will be the causative event for death.

Axonal damage may cause axons to be isolated from its cell body. Within few days after injury, the distal part of the axon degenerates [8] in contrast to the proximal part where the axon survives to a greater degree [42]. However, in the CNS axons will not regenerate spontaneously [23, 74].

During HI in the perinatal period, necrotic cysts within the brain cellular tissue are produced which is then followed by a delayed phase of tissue injury which is characterized by apoptotic cell death [31]. In addition, an over-activation of the brain inflammatory response worsen the primary neuronal injury [31].

A hallmark for many neurodegenerative diseases is accumulations of organelles and other proteins in the cell body [25]. The pathogenic accumulation of organelles suggests that defective functioning of the axon, including damage to axonal transport, contributes to disease and is now known to be true for several neurodegenerative diseases [25, 56].

Histology and immunohistochemistry is the gold standard to study cellular and axonal damage in the CNS. However, this requires tissue sampling and is often done post mortem and thus unsuited for longitudinal real time *in vivo* studies. This is also true for axon transport studies which traditionally use viruses, radioactive, or non-fluorescent tracers [64, 47, 100, 114, 82].

A versatile MRI technique is manganese-enhanced MRI (MEMRI) which combines the strengths of MRI with the physical and biological properties of manganese (Mn^{2+}). This technique makes it possible to visualize the neuroarchitecture [51, 4], neural pathways [71, 98, 70, 83, 113] and to map functional brain activity [3, 116]. In addition, MEMRI has been used for detecting brain ischemia [1, 2] and abnormal brain function associated with neurodegenerative disease [91, 93, 57].

1.2 Animal models

1.2.1 Rat optic nerve

The rat optic nerve (ON) contains about 120 000 axons [14, 15] which arise from retinal ganglion cells (RGC) in the eye and project towards the optic chiasm where the ON from both eyes meet. From the optic chiasm, the ON project through the contralateral optic tract to the thalamic lateral geniculate nucleus (LGN), midbrain pretectum, and superior colliculus (SC) [42, 108]. Visual information is processed in the LGN before it is relayed to the primary visual cortex while the SC is involved in the coordination of head and eye movements [102, 108].

1.2.2 Neonatal rat brain

The neonatal brain differs from the adult brain in several ways and normal maturation of the mammalian brain is characterized by periods of limitations in glucose transport capacity and increased use of alternative cerebral metabolic fuels lactate and ketone bodies [106]. Rates of cerebral energy metabolism are low in the immature brain and relate primarily to the level of neuronal maturation and synaptic activity at the developmental stage [106]. In contrast to adult stroke, the development of energy failure and subsequent neuron death because of HI in the immature brain results in a prolonged evolution of injury days and weeks after the primary insult [106, 30, 59].

1.3 Axonal transport

Neurons are highly polarized cells which consist of a cell body from where a single axon and shorter multiple dendrites emerge. The axon transmits signals while the dendrites are specialized to receive signals. Inside neurons and other eukaryotic

cells, microtubules are part of the cytoskeleton and are formed by alpha- and beta-tubulin into 24nm wide hollow tubes with a plus and minus end. Inside axons, microtubules are uniformly oriented with plus end pointing towards the synapse and the minus end towards the cell body [19].

Kinesin and Dynein are the major molecular motors responsible axonal transport [78]. Kinesin walks along microtubules toward the plus ends, facilitating material transport from the cell interior toward the synapse while dynein transports material toward the microtubule minus ends and transport material the cell interior [32, 78]. Kinesin has been shown to walk in 8-nm steps along a single microtubule protofilament [96, 121] and Dynein seems wander with steps that vary from 8 to 32 nm [53, 75, 112] including runs in the reverse (plus-end) direction [79]. Even though Kinesin and Dynein have preferred directions of movement their cargos can be moved bi-directionally as a result of a tug of war between Dynein and Kinesin being attached to the same cargo [58].

The transport rates of various substances are independent of the electrical activity within the axons [7, 65] and are traditionally grouped in fast and slow components with speeds of approximately 4-16mm/h and 0.004-0.25 mm/h respectively in the healthy axon, [11, 29, 65]. The same "fast" molecular motors are involved in both fast and slow axonal transport, but during slow axonal transport there are prolonged pauses between phases of movements [81, 110]. Dynein tends to tether its cargo at microtubuli intersections, a tendency which increases with increasing density of dynein [78]. Kinesin, which is smaller in size than dynein, tends to transverse microtubule intersections without stopping or reversing its direction, thus, kinesin may have a higher speed along the microtubule than Dyenin [78].

1.4 Manganese-enhanced MRI

1.4.1 Properties of manganese

Manganese is an essential trace metal found at low levels in food, water, and the air, and is a co-factor in several biological processes [6]. Mn^{2+} is a calcium (Ca^{2+}) analogue and can enter cells through voltage gated Ca^{2+}-channels [60, 62] and also be transported along axons [44, 48]. By substituting Ca^{2+} with Mn^{2+} it is also possible to get intracellular accumulation of Mn^{2+} in neurons undergoing cell death [1, 2].

1.4.2 Contrast agents

Paramagnetic materials (e.g. Mn^{2+}, Gd^{3+}, Fe^{3+} and Cu^{2+}) have unpaired electrons resulting in a net magnetic moment. The magnetic moments are randomly distributed and will cancel each other out unless they are placed in an external magnetic field where they align with the external field and produce an increase in the local field. In tissue, paramagnetic substances will interact with tissue protons through dipole-dipole interactions and create fluctuations in the magnetic field. This can affect both the longitudinal relaxation time T_1 and transversal relaxation time T_2 of the protons, and result in increased tissue contrast in T_1-weighted images or reduced tissue contrast in T_2-weighted images in regions where the paramagnetic substances are present [36, 55]. In pure water, the relaxation rates are linearly dependent on the concentration of the paramagnetic substance [50].

Mn^{2+} was early recognized as an MRI contrast agent and in vivo, Mn^{2+}can bind to a variety of materials which influence the magnetic properties in the surrounding tissue leading to a reduction in T_1 relaxation time and increased tissue contrast in T_1-weighted imaging [45, 63]. A widely used Mn^{2+} contrast agent in animal research is manganese chloride ($MnCl_2$). In water, $MnCl_2$ dissolves into Mn^{2+} and Cl^{2-} and the solution can be injected intravenously, subcutaneously, intraperitoneally or directly into the area of interest where Mn^{2+} will enter cells through the Ca^{2+}-channels. However, overexposure of Mn^{2+} may cause toxic reactions [6, 21, 80] and Parkinson-like symptoms [6, 21]. In addition, high Mn^{2+} concentrations may inactivate the voltage gated Ca^{2+}-channels which leads to unrestrained Ca^{2+}entry [12, 62]. Mn^{2+} may also increase the production of reactive oxygen species which can lead to apoptosis of neurons [27, 123].

Manganese dipyridoxyl diphosphate (MnDPDP) (Teslascan, GE Healthcare AS, Oslo, Norway) is a chelated Mn^{2+}-compound which is clinically approved for MRI of the human liver and has also been used in imaging of the human myocardium [92]. The chelate consists of Mn and the organic ligand dipyridoxyl diphosphate (DPDP). In blood, MnDPDP is metabolised by dephosphorylation to manganese dipyridoxyl monophosphate (MnDPMP) and manganese dipyridoxyl ethylendiamine diacetate (MnPLED). The MnDPDP and MnPLED metabolites are simultaneously transmetalled with zinc (Zn) releasing Mn^{2+} [101].

1.4.3 Image sequences

T_1-weighed image sequences such as the fast low angle shot (FLASH) sequence are characterized by short TR and TE [36]. The FLASH is an incoherent steady state

sequence which uses small flip angle excitations and spoiling of the transverse magnetization before the next RF pulse [36]. In steady state the signal is given by:

$$S = \rho \sin\alpha \frac{1 - \mathrm{e}^{-\frac{\mathrm{TR}}{T_1}}}{1 - \mathrm{e}^{-\frac{\mathrm{TR}}{T_1}} \cos\alpha} \mathrm{e}^{-\frac{\mathrm{TE}}{T_2*}} \tag{1.1}$$

where ρ is the proton density, α is the flip angle, TR is the repetition time, TE is the echo time and T_1 and T_2* are the longitudinal and transversal relaxation times, respectively.

The centric reordered saturation recovery turbo-FLASH sequence consists of a 90 degree inversion pulse followed by a saturation recovery delay and a turbo-FLASH readout [67]. The approximated signal is given by :

$$S = S_0 \left(1 - \mathrm{e}^{-\frac{\mathrm{TD}}{T_1}}\right) \tag{1.2}$$

where S_0 is is the maximum available signal when the longitudinal magnetization is fully relaxed, TD is the saturation recovery delay and T_1 the longitudinal relaxation time. Since the centre of k-space is read out first (centric reordered) the image contrast is mainly determined by the saturation recovery delay.

1.5 Image processing

1.5.1 Mathematical morphology

Developed during the 1960s and 1970s mathematical morphology has become a powerful tool in signal and image processing applications [11]. Since its introduction, mathematical morphology has been used in a wide range of applications including biomedical image processing [86, 89], shape analysis [37], coding and compression [41, 122], automated industrial inspection [54], texture analysis [5, 40] and radar imagery [39].

Mathematical morphology has a rigorous mathematical foundation based on set theory where an image is regarded as set in the 2D integer space Z2 (binary images), Z3 (gray scale images) or in higher dimensions which can include colour images and time varying components [33]. An image is probed with a smaller set called a structuring element which explores the image and modify the image by one or a set of rules which constitute an operation. The basic operations are erosion and dilation which "contracts" and "expands" the boundary of a set

and is the basis for operations like opening, closing, boundary extraction and top-hat transformation [33]. Openings can be used to remove small objects (e.g. noise), protrusions and thin connections between objects while closing smoothes contours, eliminates small holes and fuses narrow breaks. The top-hat transformation is defined as the difference between the original image and its opening by an structuring element and extracts small elements from the image [33, 124].

1.5.2 Image segmentation

Image segmentation is the process of extracting regions or objects from images and numerous methods exists and where the choice of method often depend of the a priori knowledge of the objects to be detected [73, 87, 99, 117]. In medical imaging, segmentation using mathematical morphology has been used in various studies including 3D MRI of the human skull [28], microscope images and MRI of blood vessels [69, 77], MRI of the human ventricular system [85], MRI of multiple sclerosis lesions [68], CT images of neuroblastoma [26] and fMRI data [52].

Central elements in mathematical morphological segmentation are pixel connectivity and region growing. The connectivity defines which pixels in the image meeting specific criteria are connected and forms objects or connected components. A region growing procedure utilizes the connectivity and extract objects by grouping pixels which are connected as defined by the connectivity. The connectivity can be defined in various ways in order to extract objects with certain shapes. To explain connectivity, the standard 3D connectivities 6-connected, 18-connected and 26-connected can be used as examples. A 3D pixel (voxel) has 6 faces, 12 edges and 8 corners. If the connectivity is 6-connected, voxels are connected if one of their faces touches. If the connectivity is 18-connected (6 faces + 12 edges), voxels are connected if faces or edges touch while 26-connected (6 faces + 12 edges + 8 corners) connectivity connect voxels where either faces, edges or corners touch [33].

Segmentation of colour images uses the same paradigms as gray scale images [18] as for example in detection of exudates in colour images of the human retina [109]. Colour images are usually stored and displayed in the RGB vector space where the Euclidian distance between two colours not necessarily correspond to the human perception of the colour difference [18] and can cause problems in segmentations. This may be bypassed by transforming the image into the Luv colour space which approximates the human perception of colour differences [88]. However, the transformation is non-linear and may significantly increase noise in the transformed image [88]. A way to segment images in the RGB vector space is to use the Mahalanobis distance [24] as a threshold which include the covariance

matrix of a sample (ROI) representative to the colour we want to segment [33]. In contrast to the Euclidian distance where all colours within a certain distance from an "average" colour describes a solid 3D sphere, the locus of points using the Mahalanobis distance describes a solid 3D elliptical body. This means that the Mahalanobis distance, as opposed to the Euclidian distance, is sensitive to different spread in colours along the three colour axis and may therefore yield a better segmentation.

1.5.3 Image registration

Image registration is the process of aligning two or more images of the same scene and was actualized in the 1970s concerning problems of aligning satellite images [94]. Image registration algorithms can use landmarks [13, 43, 66, 119], contours [22, 115], surfaces [72, 97] or volumes [49, 118] to manually or automatically define correspondence between images. Traditionally intra-subject images have been registered using rigid body transformations while inter-subject images have required non-rigid body transformation. Recently, it has been shown that intra-subject data in fMRI studies improves by using non-rigid transformation [120].

A fundamental step in image registration is to determine the transfer function which maps the points in one image into the other. The transformation should be one-to-one, i.e., each point in one image is mapped to only one point in the other and vice versa [16]. A method which obey this rule in addition to be able to handle geometrical distortions between the images is the piecewise linear mapping [34] using manually placed landmarks. Based on a set of manually placed landmarks in the images an optimal triangulation of the convex hull is calculated. For each pair of corresponding triangles a linear transfer function is found which will overlay the triangles. Outside the convex hull, the transfer function is based on extrapolated boundary triangles which may result in poor alignment [34, 35]. The area of interest should therefore be situated within the convex hull of the landmarks.

1.5.4 Model optimization

Optimization is the action of finding the best solution to a problem. Optimizing a model to fit observed data can be done by constructing a function which describe the difference between the model and data and search for the model parameters which minimizes the difference.

A mathematical model with a set of variables $x_1, ..., x_n$ can be optimized to fit a

set of data by finding the set of variables which minimize the L-norm. Generally, the L_p norm can be written as:

$$L_p = \left(\sum |Model(x_1, ..., x_n) - Data(x_1, ..., x_n)|^p \right)^{\frac{1}{p}} \; p \geqslant 1 \tag{1.3}$$

where minimizing the L_2 norm ($p = 2$) equals the least square fit.

A simplex method for finding a local minimum of a function of n variables, e.g. the L-nom, has been developed by Nelder and Mead [61]. The method is a systematic search that compares function values at each vertex of a simplex, a generalized triangle in n dimensions, and rejects the worst vertex (largest function value), replaces it with a new and repeats the procedure. The process creates a sequence of simplexes for which the function values of the vertices gradually get smaller until a minimum has been found. Since the procedure terminates at any local minimum several searches with different initial conditions should be carried out to increase the probability to find the global minimum.

Chapter 2

Aims of study

The main objective of this thesis were to develop and apply methods for analysing MEMRI of the normal and injured rat central nervous system.

More specifically, the aims of this thesis were:

1. Develop and scientifically evaluate methods for segmentation of axons and brain tissue with manganese accumulation (Paper I & IV).
2. Develop and scientifically evaluate methods for quantification of signal/contrast changes related to manganese accumulation and transport (Paper I & III).
3. Adapt these methods to scientific studies of:
    a) Nerve damage and regeneration in CNS (Paper II).
    b) Uptake and transport kinetics in brain neurons and axons (Paper III).
    c) Tissue damage after ischemic insult in the neonatal brain (Paper IV).

Chapter 3

Materials and Methods

3.1 Animal models

3.1.1 Animal handling

Fisher (Paper I & II), Sprague Dowley (Paper III) and Wistar rats (Paper IV) were used in the studies. The animals were kept in a 12:12h light:dark cycle and allowed free access to food and water. All experimental procedures were performed under anaesthesia and analgesia was provided afterwards if required. Guidelines approved by the local ethics committee for animal research were followed and all experiments were approved by the responsible governmental authorities.

3.1.2 Contrast agent injections

Anesthetized animals were placed in a purpose-built head frame and a single dose of $MnCl_2$ (Paper I-III), MnDPDP (Paper I) and Gadodiamid (Paper I) was injected through the sclera posterior to the ora serrata of the left eye using a purpose-built injection device consisting of a plastic syringe connected via polyethylene tubing to a glass micropipette with a tip diameter of 50 μm. After the injection the pipette was slowly withdrawn to minimize reflux. In Paper IV, animals were given a single dose of $MnCl_2$ intraperitoneally.

3.1.3 CNS injury

Optic nerve crush (ONC) was performed according to the method described by Berry et al. [10]. In brief, the dural sheath of the ON was incised longitudinally after intraorbital exposure through a superior palpebral incision, and the ON was crushed for 10 seconds, 2 mm distal to the lamina cribrosa with microforceps,

leading to a complete transaction of all axons. Hypoxic-ischemic injury (HI) (Paper IV) was performed according to Vannucci-Rice model for HI brain damage [76, 105]. Through a mid-neck incision, the right common carotid artery was thermo-cauterized and severed. After surgery, the animals were exposed to pre-heated air (36 deg C) with 8% O_2 in 92% N_2 for 75 minutes.

3.2 MRI

3.2.1 T_1-weighted MRI

Paper I: 2.35 T Bruker Biospec Avance DBX-100 with water-cooled BGA-12 (200 mT/m) gradients (Bruker, Ettlingen, Germany). A 72-mm volume coil was used for RF transmission and an actively decoupled quadrature rat head surface coil for receive. Data acquisition: T_1-weighted FLASH with TR/TE = 15/4.2 ms, and a flip angle of 25 deg. Field of view (FOV) = 5x5x2 cm^3. With an acquisition matrix of 256x256x64, the voxel resolution was 195x195x312 μm^3.

Paper II: 7 T Bruker Biospec Avance 70/20 with water-cooled BGA-12 (400 mT/m) gradients. A 72-mm volume coil was used for RF transmission and an actively decoupled quadrature rat head surface coil for receive. Data acquisition: T_1-weighted FLASH with TR/TE = 12.5/3.7 ms, and a flip angle of 20 deg. FOV = 4x4x2.3 cm^3. With an acquisition matrix of 192x192x112, the voxel resolution was 208x208x205 μm^3.

Paper III: 7 T Bruker Biospec Avance 70/20 with water-cooled BGA-12 (400 mT/m) gradients. A 72-mm volume coil was used for RF transmission and an actively decoupled quadrature rat head surface coil for receive. Data acquisition: 3D centric recorded saturation recovery turbo-FLASH sequence, with saturation delay=500ms, flip angle = 15 deg. TR/TE = 9.25/2.7 ms, echo train length 445 ms and number of segments = 4. FOV = 3.5x3.5x2.64 cm^3. With an acquisition matrix of 192x192x66, the voxel resolution was 182x182x400 μm^3.

Paper IV: 7 T Bruker Biospec Avance 70/20 with water-cooled BGA-12 (400 mT/m) gradients. A 72-mm volume coil was used for RF transmission and an actively decoupled quadrature mouse head surface coil for receive. Data acquisition: T_1-weighted FLASH with TR/TE = 12/3.0 ms, flip-angle = 30 deg. FOV = 20x20x17.5 mm. The acquisition matrix was 128x96x84 giving an acquired resolution of 156x208x208 μm^3. With zero-filling of the matrix to 128x128x112, the interpolated resolution was 156 μm^3 isotropic.

3.2.2 T_2-maps

Paper IV: 2D T_2-maps were obtained with a spin-echo sequence (MSME) with TR/TE = 2500/7.6 ms, 40 echoes, slice thickness 1 mm. FOV = 18x18 mm and acquisition matrix 128x96 giving an in plane resolution of 140x187 μm^2. With zero-filling of the matrix to 128x128 the interpolated resolution was 140 μm^2 isotropic.

3.2.3 Diffusion tensor imaging

Paper II: A 2D multishot (four segments) DTI-EPI scan with five oblique axial slices containing the ON was obtained with TR/TE = 1500/ 32.6 ms, Δ = 15 ms, δ = 6 ms. Diffusion sensitizing gradients along 12 non-collinear directions and six b-values in the range of 0-3000 s/mm^2 (five A0 images, and 300, 600, 1000, 1600, 2300, and 3000 s/mm^2) were used. The slice thickness was 0.8 mm (no gap), FOV = 5x5 cm^2, and the acquisition matrix size = 160x160 (zero-filled to 256x256).

3.3 Data analysis

3.3.1 Optic nerve segmentation

In Paper I, a technique for semiautomatic segmentation of the manganese-enhanced ON was developed. In brief, the 3D image was binarised using a global threshold close to the mean signal of the non-enhanced ON. Then morphological segmentation of the manganese-enhanced ON was done by a 6-connected region growing resulting in an image containing the manganese-enhanced eye, ON, and part of the brain. The ON was separated from the eye and brain using a morphological top-hat transformation with a spherical structuring element with a diameter slightly largger than the ON diameter. Furthermore, a sliding box technique was developed to ensure correct definitions of the ON co-ordinates. The ON co-ordinates was re-sampled with 0.2 mm resolution and the signal in a 1 mm diameter ROI centred on the ON in 2D planes perpendicular to the ON was calculated every 0.2 mm.

Due to image distortions (Paper II) and low signal to noise ratio (SNR) (Paper III), the segmentation procedure failed to segment the ON in the DTI datasets (Paper II) and in the study of manganese kinetics (Paper III). In these cases the co-ordinates of the centre were manually identified along the ON. The set of

co-ordinates were re-sampled with 0.2mm resolution by either bi-linear (Paper II) or tri-linear (Paper III) interpolation which gave an intensity curve of the ON for each scan.

3.3.2 Axonal Mn^{2+} transport model optimization

In Paper III, approximated ON Mn^{2+} concentration curves at various time points were constructed by subtracting a mean pre Mn^{2+} intensity curve from the post Mn^{2+} injection curves. Three different transport functions were evaluated; 1) a single component anterograde convection together with random walk and clearance as described in [20] and [57], 2); a pure anterograde convection with a majority of fast velocity components, and 3); a pure anterograde convection with a majority of slow velocity components. The transport functions together with two different functions which described Mn^{2+} entrance into RGC axons were fitted to the concentration curves. The fit was done by optimizing the model parameters in order to minimize the L_1 and L_2 norm.

3.3.3 Segmentation of manganese enhanced areas in the ischemic brain

In paper IV, a binary mask of the manganese-enhancement in the injured hemisphere was defined by signal intensities above a threshold set by the mean signal intensity (SI) of a ROI placed in the thalamus of the contralateral non-injured hemisphere + 1 SD of the image noise.

3.3.4 Histology

Histological counting of the RGC in retina (Paper II) was obtained after injection of 1 μl FluroGold into the ON between the lamina cribrosa and ONC 20 days past lesion (dpl). After preparation, the retina was whole mounted on a slide, defining the temporal, nasal, superior and inferior retinal quadrants with radial incisions. A 349.0x440.4 μm^2 counting grid was projected onto the mid radial point of each retinal segment and the total number of FluroGold-filled RGC recorded per grid. Details on the preparations are given in the Material and Methods section in Paper II. The ON was dissected, straightened on a stiff card, and dried in room temperature for a couple of minutes. After preparation, the ON was frozen at -80 deg. C and 5 μm thick frozen longitudinal sections were cut and mounted onto dedicated microscope slides. After further preparation, sections

were stained with anti-GAP43. After preparation, 8 μm coronal sections of the HI brain corresponding to -3.25 mm from the bregma (Paxinos and Watson, 1998) were cut and stained with among others anti-MAP2, anti-GFAP and anti-CD68 (Paper IV).

3.3.5 Segmentation of stained areas in the histology images

Images of whole histological slices stained for MAP-2, CD68 and GFAP (Paper IV) were segmented in the RGB vector space using the Mahalanobis distance from an average colour calculated from a ROI manually placed in an area with uniform staining. The segmented colours were defined to be in a distance equal or less than 1 SD from the average colour, where the SD was selected from the RGB component with the largest variance within the ROI. From this a binary mask for the area of staining was created.

3.3.6 Image registration

The T_1-weighted MR images and the histology images (Paper IV) were co-registered using landmark based image registration. After manually selecting approximately 15 pairs of anatomical points of reference in the two images, the transformation was calculated using piecewise linear mapping. The transformation was applied to the segmented histology image which enabled comparison of manganese-enhanced areas and segmented histology staining on a pixel-to-pixel basis.

3.3.7 Statistical analysis

Statistical analyses were conducted using the statistical software package SPSS (SPSS Inc., Chicago, IL, USA), with a significance level of 5%. The statistical analyses are described in detail in the Material and Methods sections of each individual paper.

Chapter 4

Summary of papers

Paper I
Axon tracing in the adult rat optic nerve and tract after intravitreal injection of MnDPDP using a semi-automatic segmentation technique

Øystein Olsen, Marte Thuen, Martin Berry, Vassili Kovalev, Maria Petrou, Pål Erik Goa, Axel Sandvig, Olav Haraldseth, and Christian Brekken.
Journal of Magnetic Resonance Imaging 27:34–42, 2008

The aims of this study were to:

1. Develop and validate an objective technique for 3D segmentation of the manganese enhanced optic nerve in adult rats and to improve CNR calculations.
2. Use the technique to ascertain if manganese dipyridoxyl diphosphate (MnDPDP) gives sufficient Mn^{2+} enhancement compared to $MnCl_2$ when used for functional imaging of the visual pathway.

Intravitreal MnDPDP injection resulted in significant MRI contrast enhancement of the retina and ON after 12-24 hours. The enhanced optic nerve was successfully segmented and CNR calculated accurately within 2 minutes on a standard desktop PC in a representative 3D MR image volume using a semi-automated procedure.

Mn^{2+} was found to be released from MnDPDP after intravitreal injection in sufficient amounts to obtain functional tracing of the adult rat primary visual pathway. This study also indicated that a slow release contrast agent formulation might be useful to prevent the high initial Mn^{2+} concentration that follows from $MnCl_2$ injections for such tract-tracing studies.

Paper II
Combination of Mn^{2+}-enhanced and diffusion tensor MR imaging gives complementary information about injury and regeneration in the adult rat optic nerve

Marte Thuen, Øystein Olsen, Martin Berry, Tina Bugge Pedersen, Anders Kristoffersen, Olav Haraldseth, Axel Sandvig, and Christian Brekken.
Journal of Magnetic Resonance Imaging 29(1):39-51, 2009

The aims of this study were to:

1. Evaluate manganese MEMRI and diffusion tensor imaging (DTI) as tools for detection of axonal injury and regeneration after peripheral nerve graft (PNG) implantation in the rat optic nerve.
2. Investigate retinal ganglon cell survival after optic nerve crush (ONC) and PNG implantation.

This study showed that MEMRI and DTI enabled detection of functional and structural degradation after rat ON injury, and there was correlation between MEMRI and immunohistochemical measures of axon regeneration. The DTI-derived parameters fractional anisotropy, mean diffusivity, axial diffusivity, and radial diffusivity were unaffected by the presence of Mn^{2+} in the ON.

At 1 dpl, both CNR (MEMRI) and axial diffusivity were reduced at the injury site, while at 21 dpl they were increased. ONC reduced RGC density in retina at 21 dpl compared to noninjured ON without $MnCl_2$ injections. Both intravitreal PNG and intravitreal $MnCl_2$ injections improved RGC survival in retina after ONC.

Paper III
Manganese transport in the rat optic nerve evaluated with spatial- and time-resolved MRI

Øystein Olsen, Anders Kristoffersen, Marte Thuen, Axel Sandvig, Christian Brekken, Olav Haraldseth, Pål Erik Goa.

Submitted to Journal of Magnetic Resonance Imaging

The aim of this study were to:

1. Utilize spatial- and time-resolved MEMRI and different models of how Mn^{2+} enters RGC axons and axonal transport of Mn^{2+} to evaluate Mn^{2+} RGC axon entrance, multiple transport rates, dispersion and clearance in the healthy rat ON after intravitreal manganese injection.
2. Compare predictions from the new models with previously reported experimental data.

The study showed that the rate of Mn^{2+} entrance into the RGC axon is not proportional to the Mn^{2+} concentration in the vitreous body. Instead a model with constant rate of Mn^{2+} influx, termed rate limited axonal entrance, gave a good fit to the experimental data. In addition, the model simulations showed that rate limited axonal entrance explains the semi-logarithmic relationship between intravitreal Mn^{2+} dose and ON contrast enhancement seen in-vivo [98].

The study did not give any clear answers regarding the transport along the ON. Both a random-walk like model with bi-directional transport and a convection-like model with uni-directional transport gave similar fit to the data. However, what did seem clear, was that components of both fast and slow transport is necessary in order to fit the data, which might indicate that manganese does not depict synaptic vesicle transport rates directly. Clearance of Mn^{2+} along the ON is slow or non-existent. Two of the models gave an infinite time constant for exponential axonal clearance while one model gave a time constant of 100h.

Paper IV
Manganese-enhanced magnetic resonance imaging of hypoxic-ischemic brain injury in the neonatal rat

Marius Widerøe, Øystein Olsen, Tina Bugge Pedersen, Pål Erik Goa, Annemieke Kavelaars, Cobi Heijnen, Jon Skranes, Ann-Mari Brubakk, Christian Brekken.
Neuroimage 45(3):880-90 2009

The aims of this study were to:

1. Depict delayed neuronal death by MEMRI up to several days after the initial hypoxicischemic insult (HI) in the neonatal rat brain.
2. Evaluate the specificity of MEMRI in detection of cells related to injury by comparison with histology and immunohistochemistry.

Seven days after HI, increased Mn enhancement was seen on T_1-weighted images in parts of the injured cortex, hippocampus and thalamus among HI+Mn pups, but not among HI+Vehicle or Sham+Mn pups. Comparison with immunohistochemistry showed delayed neuronal death and inflammation in these areas with late Mn enhancement. Areas with increased Mn enhancement corresponded best with areas with high concentrations of activated microglia. Thus, late Mn enhancement seems to be related to accumulation of manganese in activated microglia in areas of neuronal death rather than depicting neuronal death per se.

Chapter 5

General discussion

5.1 Main findings

The main objective of this thesis was to develop methods for segmentation of manganese enhanced axons and brain tissue and apply the methods for studies of axonal damage and repair, axon transport of Mn^{2+}, and studies of ischemic insult in the neonatal brain. The main finding of Paper I was that the manganese enhanced ON could be segmented and CNR calculated along the ON using a combination of global thresholding, region growing and a sliding box technique. Furthermore we showed that a top hat transformation resulted in a consistent separation of the ON from the manganese enhanced retina at lamina cribrosa which defined a reliable zero point for measuring distance along the ON. In Paper II we applied MEMRI and the method developed in Paper I to detect blocking of Mn^{2+}transport in and beyond the site of a nerve crush 1 dpl and increased Mn^{2+} enhancement 21 dpl and implantation of a peripheral nerve graft. The increase of Mn^{2+} enhancement 21 dpl corresponded well with histological findings which showed axon re-generation at the lesion site and beyond.

In paper III, model fitting to time- and spatial resolved ON MEMRI data indicated that entrance of Mn^{2+} into RGC axons after intravitreal injection is rate limited and independent of the Mn^{2+} concentration above a certain threshold. Furthermore, the model optimization indicated that Mn^{2+} is loosely bound during axonal transport which means that the apparent Mn^{2+} transport velocities are different from the genuine synaptic vesicle transport velocities.

In Paper IV, T_1-weigthed images and T_2-maps of hypoxic ischemic rat pup brains were segmented using a global threshold and region growing while stained areas in the histology images were segmented in the RGB vector space. Comparison of segmented Mn^{2+} enhanced areas and areas with reduced T_2 showed a 53% match. Comparison of Mn^{2+} enhanced areas with segmented immunohistochemical staining showed best spatial agreement between Mn^{2+} and activated microglia/macrophages.

5.2 Methodological considerations

The initial process of segmentation of the Mn^{2+} enhanced volumes (Paper I and II) and areas (Paper IV) was based on a threshold which binarised the image and included voxels for further morphological image processing steps. The threshold was based on the SI in the non-enhanced ON (Paper I and II) and SI in the non-injured brain hemisphere (Paper IV). At least three factors influenced which voxels were included for further analysis: 1) the threshold level, 2) the image noise and 3), any gradient in the image which may change the overall signal level from where the threshold level was determined to where it was applied.

In Paper I and Paper II the threshold was determined by the mean SI in a ROI manually placed in the non-enhanced ON. Since the diameter of the rat ON is about 1mm and the voxel size was 0.2mm the mean SI in a small ROI manually placed on the ON is susceptible for both inherent partial volume effect and an artificial partial volume effect caused by slight misplacement of the ROI. This will cause an error in the estimate of the mean SI but as the validation of the method showed (Paper I) the centre of nerve co-ordinates were not sensitive for variation within 10% of the threshold level. In Paper IV, the threshold was determined by the mean of a ROI placed in the corresponding non-injured hemisphere. Enhanced areas (T_1-weighted images) and reduced T_2 areas (T_2-maps) were defined to be above and below 1 SD of the mean, respectively. The use of a large ROI made the determination of the threshold level less sensitive of the exact positioning of the ROI.

During data acquisition, thermal noise enters the signal and ad to the intrinsic object noise formed by the statistical behaviour of the spin populations [111]. The noise is generally known to be characterized by a zero mean Gaussian probability function which is transformed into a Rice probability function after reconstruction of the complex MR signal into a magnitude image [90]. Because of noise, some voxels may wrongly be included in the binarised image after applying a threshold. In Paper I and Paper II, 6-connected region growing was applied to the binarised 3D image to segment theMn^{2+} enhanced ON. This included only voxels where neighbouring voxel faces touched as expected in the ON which is a heavily elongated object. Wrongly included voxels because of noise showed a more random spatial distribution appearing either alone or in groups connected by edges and corners in addition to faces. 6-connected region growing omitted the corner- and edge-connected voxels and resulted in a smooth segmented nerve (Figure 5, Paper I). In Paper II the method was applied to detect axon regeneration after ON nerve crush and intravitreal implantation of a peripheral nerve graft (PNG). The use of PNG in this model results in few percent regeneration of axons [9] and a small but significant increase of CNR was detected beyond

the crush 21 dpl (Paper II, Figure 7). Because of few regenerating axons the MEMRI signal in the regenerating area was small and close to the noise. Low signal MEMRI voxels wrongly omitted by 6-connected region growing may have been included in the segmented nerve if 18- or 26-connected region growing had been applied. However, the contrast was calculated based on re-sampled slices perpendicular to the nerve which was independent of the choice of connectivity. Higher degree of connectivity may have leaded to longer part of the ON being segmented but also increased the risk for including noise voxels in the definition of the segmented ON.

In Paper III, the dynamic changes in MEMRI signal along the ON was investigated which included the low MEMRI signal from the first time points after intravitreal Mn^{2+} injections. The weak MEMRI signal at these time points gave unreliable segmentation results and the ON was therefore manually identified in the image volume. This was also the case for the EPI-DTI data in Paper II where the segmentation method also failed to give reliable results because of the image artefacts. EPI is prone to several artefacts such as chemical shift and eddy current in addition to distortions due to field inhomogeneity and magnetic susceptibility variations. SE-DTI may have produced maps with sufficient quality for the segmentation procedure to work but because of the long scan time [95] this technique was difficult to combine with the other MRI protocol in the study.

A surface coil was used for signal detection. The advantage of a small surface coil is the high sensitivity close to the coil and the small volume form where noise is received, both of which contribute to a good SNR. However, the sensitivity is highly inhomogeneous and results in a gradually decreased tissue signal as a function of distance form the coil [17]. This leads to gradients in the image which may impact both segmentation and calculation of CNR. In Paper I, no corrections of the image gradients before segmentation were made but this did not affect the segmentation of the ON because of the high MEMRI signal in the enhanced nerve. In Paper II and Paper IV, low resolution correction scans were used to correct for the image gradients. This was important in order to segment the low MEMRI signal from the regenerating axons (Paper II) and areas with low Mn^{2+} accumulation (Paper IV) which else may have been below the threshold and not included for further analysis. The rat ON projects ventrally from the retina towards the optic chiasm away from the dorsally located surface coil which result in a gradually reduced signal along the ON. In Paper I, this was corrected for by using a linear regression model based on non-enhanced ON data when calculating CNR profiles. However, the signal do probably not vary linearly along the ON, both because the surface coil field does not vary linearly [107] and because the ON curves from the retina towards the optic chiasm (Paper 1, Figure 5a). As a result of the linear approximation, the CNR curves presented in Paper I may

include variations caused by the surface coil. In Paper III, the signal variation along the ON was corrected by subtracting the mean signal from the ON (n=5) before intravitreal $MnCl_2$ injection. Since these data were obtained almost in the same positions as the Mn^{2+} enhanced data relative to the surface coil the result was not susceptible spatial change in the coil field as we could expect if we used data from the contralateral non-enhanced ON. The use of low resolution correction scans in Paper II and Paper IV removed the gradients in the images caused by the coil.

In pure water, the relaxation rate $\frac{1}{T_1}$ is a linear function of the concentration of a contrast agent [50]. T_1-mapping which gives the true T_1 value in tissue [17, 38] therefore yield a method for studying absolute Mn^{2+} tissue concentration. However, a reliable 3D T_1-maping sequence was not available for use in this project. Instead, 3D T_1-weighted imaging was used in the MEMRI studies where CNR can be used to estimate Mn^{2+} temporospatial variations since it reflects the difference between enhanced and non-enhanced tissue . In Paper I and Paper II, ON CNR curves were made based the segmented Mn^{2+} enhanced ON and the mean SI in a ROI manually placed in the non-enhanced ON. As discussed above, manually placing a small ROI in the non-enhanced ON may induce errors in the estimate of the non-enhanced ON signal. Correct calculation of CNR was crucial in detecting nerve damage (Paper II) where a too high or too low CNR in and beyond the ON crush could lead to opposite conclusions. However, the result from the segmentation and CNR calculation was supported by both histology and visual inspection, but the CNR sensitivity to errors in the estimation of the enhanced and non-enhanced signal should be considered in these types of studies.

In Paper III, signal intensity (SI) was used to estimate Mn^{2+} temporospatial variations. There are two main issues to take into considerations when comparing changes in SI between different animals at different time points and approximating SI to Mn^{2+} concentration: 1), SI is a dimensionless quantity resulting from the number of spins which have been manipulated and their coupling to the coil, and scaling during image reconstruction; and 2), in a T_1-weighted sequence change in SI is not linearly related to changes in Mn^{2+} concentration. Regarding the first point, different sequence settings such as TR, TE and geometry, as well as changes in subject shape, size, mass and positioning within the magnet will alter the SI. SI is also sensitive to changes in tuning and matching of the coil, receiver gain, inhomogeneities the excitation field (B1) and reception coil sensitivity, and is independently rescaled during reconstruction for each scan. In this study all sequence settings were identical in each scan, and equally sized animals were put in the same position within the magnet. Differences in receiver gain and reconstruction scaling were corrected and tuning and matching performed equally, but spatial variations in the local reception coil sensitivity were not cor-

rected and the B1 field was not mapped to check for B1 homogeneity. Those parameters could affect our results but, since we compare SI at the same positions relative to the magnet iso-centre, these effects mainly represent a systematic error and do not play an important role in the dynamic changes. Regarding the second point, we assumed that changes in SI were proportional to changes in the Mn^{2+} concentration. This approximation is only true for small variations but, for larger variations, SI tends to underestimate Mn^{2+} variations. The approximation probably holds for the changes we observe in the ON, but early time points of the vitreous body data were probably in the non-linear regime and may have influenced the estimation of the time constant for vitreal clearance used in the input functions. However, our conclusions are based on the overall shape of the input function rather than small changes the time constant for the exponential decay.

In Paper IV, stained areas in histology images where segmented and compared with Mn^{2+} enhanced areas in T_1-weigted images after co-registration of the images. The segmented colours were based on the colours within a sample ROI representative to the coloured areas of interest. Since the ROI was placed manually the selected colour sample was sensitive to user errors and may have influenced the results. The segmented area was aligned with the T_1-weigted image using a piecewise linear transform. Event though the transform can handle local geometrical distortions [34], alignment of large distortions is sensitive to the number and positioning of the landmarks. An example of large local distortion can be seen in Paper IV Figure 7 where part of the cortex which in HI animals *in vivo* was supported by cystic tissue, *ex vivo* have moved substantially. This effect might have contributed to misalignment of part of the images. However, a visual inspection was carried out in every case to validate the result.

5.3 Intracellular manganese

Mn^{2+} enters the cells through voltage gated Ca^{2+}-channels [60] and the use of the Ca^{2+}-channel blocker diltiazem has shown to reduce uptake of Mn^{2+} [70]. In Paper I, the T_1 contrast agents $MnCl_2$, manganese dipyridoxcyl monophosphate (MnDPDP) and gadodiamide (Gd^{3+}) were injected intravitreally. Both $MnCl_2$ and MnDPDP which probably released Mn^{2+} through transmetallization with intraocular zinc (Zn) [46, 101] gave enhancement in the retina, ciliary body and ON, while no enhancement in these areas was seen with Gd^{3+}. This supported the hypothesis on specific uptake rather than unspecific uptake like pinocytosis. Ca^{2+}-channels have an ion turnover rate of approximately $3 \cdot 10^6$ Ca^{2+} ions/s [103] which means that there is a plateau of ion transport into the cell. In Pa-

per III, model optimization of time and spatial resolved MEMRI data detected a plateau of Mn^{2+} input into the ON after intravitreal injection. However, the plateau could also be due to restricted input of Mn^{2+} into the axons, e.g. restricted Mn^{2+} vesicle packing, or a combination of both. To our knowledge this is the first time such a plateau is detected.

The existence of a plateau was supported by simulations of dose-concentration relationship in the ON which showed a semi-logarithmic relationship between the doses of intravitreal injected Mn^{2+} and ON Mn^{2+} concentration when restricted Mn^{2+} input was assumed, while the relationship was linear if we assumed a Mn^{2+} concentration dependent input (Paper III, Figure 8). A semi-logarithmic relationship between intravitreal Mn^{2+} dose and ON CNR has earlier been reported from in-vivo MEMRI of the rat visual system by Thuen et al. [98]. The existence of a plateau of maximum Mn^{2+} input into the ON suggest that increased ON signal enhancement observed with increased dose [98] is a consequence of a greater duration of Mn^{2+} availability when large doses are used. As a consequence, the Mn^{2+} exposure can be greatly reduced by using a slow release low dose contrast agent with a release rate tuned to the uptake threshold, and ON signal enhancement may even be improved if the contrast agent release time is increased.

After entering the cell, Mn^{2+} complex with other molecules or enter subcellular compartments for axonal transport [7] like mitochondria and vesicles. Mitochondria travel slowly (0.18-1.08 mm/h) [84] while neural vesicles may travel as fast as 18 mm/h [104]. Mn^{2+} may enter several of these compartments, and thus travel at various velocities in the same axon [7]. The transport model optimization in Paper III forced the centre of all tested velocity distributions towards zero which indicated a high density of slow transporters. This may indicate a high degree of transport in mitochondria. However, the two transport models which fitted the data best both supported infinitesimal velocity components which means that even slower velocities than reported for mitochondria seemed to be involved. This could include slow transport, but an alternative hypothesis is that Mn^{2+} is loosely bound during transport fall off and re-enter transporters which create apparent velocities different from the genuine transporter velocities, e.g. vesicle and mitochondria transport velocities.

5.4 Conclusion

Methods for segmentation of axons and brain tissue with manganese accumulation together with methods for quantification of signal- and contrast changes

along axons related to manganese accumulation and transport have been established. The methods have enabled more reliable *in vivo* studies of axonal damage and repair in parts of the CNS and provided more profound knowledge about axonal manganese transport kinetics, as well as novel insight into the relationship between manganese enhancement and neural death related to ischemic insult in the neonatal brain.

Bibliography

[1] I. Aoki, T. Ebisu, C. Tanaka, K. Katsuta, A. Fujikawa, M. Umeda, M. Fukunaga, T. Takegami, E. M. Shapiro, and S. Naruse. Detection of the anoxic depolarization of focal ischemia using manganese-enhanced mri. *Magn Reson Med*, 50(1):7–12–, 2003.

[2] I. Aoki, S. Naruse, and C. Tanaka. Manganese-enhanced magnetic resonance imaging (memri) of brain activity and applications to early detection of brain ischemia. *NMR Biomed*, 17(8):569–80–, 2004.

[3] I. Aoki, C. Tanaka, T. Takegami, T. Ebisu, M. Umeda, M. Fukunaga, K. Fukuda, A. C. Silva, A. P. Koretsky, and S. Naruse. Dynamic activity-induced manganese-dependent contrast magnetic resonance imaging (daim mri). *Magn Reson Med*, 48(6):927–33–, 2002.

[4] I. Aoki, Y. J. Wu, A. C. Silva, R. M. Lynch, and A. P. Koretsky. In vivo detection of neuroarchitecture in the rodent brain using manganese-enhanced mri. *Neuroimage*, 22(3):1046–59–, 2004.

[5] A. Asano. Texture analysis using morphological pattern spectrum and optimization of structuring elements. In *Image Analysis and Processing, 1999. Proceedings. International Conference on*, pages 209–214–, 1999.

[6] M. Aschner, K.M. Erikson, and D.C. Dorman. Manganese dosimetry: Species differences and implications for neurotoxicity. *Crit. Rev. Toxicol.*, 35:1–32–, 2005.

[7] E. L. Bearer, T. L. Falzone, X. Zhang, O. Biris, A. Rasin, and R. E. Jacobs. Role of neuronal activity and kinesin on tract tracing by manganese-enhanced mri (memri). *Neuroimage*, 37 Suppl 1:S37–46–, 2007.

[8] J. L. Becerra, W. R. Puckett, E. D. Hiester, R. M. Quencer, A. E. Marcillo, M. J. Post, and R. P. Bunge. Mr-pathologic comparisons of wallerian degeneration in spinal cord injury. *AJNR Am J Neuroradiol*, 16(1):125–33–, 1995.

[9] M. Berry, J. Carlile, and A. Hunter. Peripheral nerve explants grafted into the vitreous body of the eye promote the regeneration of retinal ganglion cell axons severed in the optic nerve. *J Neurocytol*, 25(2):147–70–, 1996.

[10] M. Berry, J. Carlile, A. Hunter, W. Tsang, P. Rosustrel, and J. Sievers. Optic nerve regeneration after intravitreal peripheral nerve implants: Trajectories of axons regrowing through the optic chiasm into the optic tracts. *J. Neurocytol.*, 28:721–741–, 1999.

[11] N. Bouaynaya, M. Charif-Chefchaouni, and D. Schonfeld. Theoretical foundations of spatially-variant mathematical morphology part i: Binary images. *Pattern Analysis and Machine Intelligence, IEEE Transactions on*, 30(5):823–836–, 2008.

[12] L. Castelli, F. Tanzi, V. Taglietti, and J. Magistretti. Cu^2+, co^2+, and mn^2+ modify the gating kinetics of high-voltage-activated ca^2+ channels in rat palaeocortical neurons. *J. Membr. Biol.*, 195:121–136–, 2003.

[13] R. Castillo, E. Castillo, R. Guerra, V. E. Johnson, T. McPhail, A. K. Garg, and T. Guerrero. A framework for evaluation of deformable image registration spatial accuracy using large landmark point sets. *Phys Med Biol*, 54(7):1849–70–, 2009.

[14] C. Cavallotti, D. Cavallotti, N. Pescosolido, and E. Pacella. Age-related changes in rat optic nerve: morphological studies. *Anat Histol Embryol*, 32(1):12–6–, 2003.

[15] W. O. Cepurna, R. J. Kayton, E. C. Johnson, and J. C. Morrison. Age related optic nerve axonal loss in adult brown norway rats. *Exp Eye Res*, 80(6):877–84–, 2005.

[16] G. E. Christensen and H. J. Johnson. Consistent image registration. *Medical Imaging, IEEE Transactions on*, 20(7):568–582–, 2001.

[17] K. H. Chuang and A. Koretsky. Improved neuronal tract tracing using manganese enhanced magnetic resonance imaging with fast t(1) mapping. *Magn Reson Med*, 55(3):604–11–, 2006.

[18] D. Comaniciu and P. Meer. Robust analysis of feature spaces: color image segmentation. In *Computer Vision and Pattern Recognition, 1997. Proceedings., 1997 IEEE Computer Society Conference on*, pages 750–755–, 1997.

[19] Cecilia Conde and Alfredo Caceres. Microtubule assembly, organization and dynamics in axons and dendrites. *Nat Rev Neurosci*, 10(5):319–332–, 2009.

[20] D. J. Cross, J. A. Flexman, Y. Anzai, K. R. Maravilla, and S. Minoshima. Age-related decrease in axonal transport measured by mr imaging in vivo. *Neuroimage*, 39(3):915–26–, 2008.

[21] J. Crossgrove and W. Zheng. Manganese toxicity upon overexposure. *NMR biomed.*, 17:544–553–, 2004.

[22] C. Davatzikos, J. L. Prince, and R. N. Bryan. Image registration based on boundary mapping. *IEEE Trans Med Imaging*, 15(1):112–5–, 1996.

[23] S.J.A. Davies, M.T. Fitch, S.P. Memberg, A.K. Hall, G. Raisman, and J. Silver. Regeneration of adult axons in white matter tracts of the central nervous system. *Nature*, 390:680–683–, 1997.

[24] R. De Maesschalck, D. Jouan-Rimbaud, and D. L. Massart. The mahalanobis distance. *Chemometrics and Intelligent Laboratory Systems*, 50(1):1–18–, 2000.

[25] K. J. De Vos, A. J. Grierson, S. Ackerley, and C. C. Miller. Role of axonal transport in neurodegenerative diseases. *Annu Rev Neurosci*, 31:151–73–, 2008.

[26] Hanford Deglint, Rangaraj Rangayyan, Fabio Ayres, Graham Boag, and Marcelo Zuffo. Three-dimensional segmentation of the tumor in computed tomographic images of neuroblastoma. *Journal of Digital Imaging*, 20(1):72–87–, 2007.

[27] M.S. Desole, L. Sciola, M.R. Deloga, S. Sicanca, and R. Migheli. Manganese and 1-methyl-4-(2-ethylphenyl)-1,2,3,6-tetrahydropyridine induce apoptosis in pc12 cells. *Neurosci. Lett.*, 209:193–196–, 1996.

[28] Belma Dogdas, David W. Shattuck, and Richard M. Leahy. Segmentation of skull and scalp in 3-d human mri using mathematical morphology. *Human Brain Mapping*, 26(4):273–285–, 2005.

[29] R. G. Elluru, G. S. Bloom, and S. T. Brady. Fast axonal transport of kinesin in the rat visual system: functionality of kinesin heavy chain isoforms. *Mol Biol Cell*, 6(1):21–40–, 1995.

[30] R. Geddes, R. C. Vannucci, and S. J. Vannucci. Delayed cerebral atrophy following moderate hypoxia-ischemia in the immature rat. *Dev Neurosci*, 23(3):180–5–, 2001.

[31] M. B. Gill and J. R. Perez-Polo. Hypoxia ischemia-mediated cell death in neonatal rat brain. *Neurochem Res*, 33(12):2379–89–, 2008.

[32] L. S. Goldstein and Z. Yang. Microtubule-based transport systems in neurons: the roles of kinesins and dyneins. *Annu Rev Neurosci*, 23:39–71–, 2000.

[33] Rafael C Gonzales and Richard E Woods. Prentice-Hall Inc., New Jersey, 2002.

[34] Ardeshir Goshtasby. Piecewise linear mapping functions for image registration. *Pattern Recognition*, 19(6):459–466–, 1986.

[35] Ardeshir Goshtasby. John Wiley & Sons, Inc., Hoboken, New Jersey, 2005.

[36] E.M. Haacke, Brown R.W., Thompson M.R., and Venkatesan R. John Wiley & Sons, Inc., New York, 1999.

[37] Robert M. Haralick, Stanley R. Sternberg, and Xinhua Zhuang. Image analysis using mathematical morphology. *Pattern Analysis and Machine Intelligence, IEEE Transactions on*, PAMI-9(4):532–550–, 1987.

[38] E. Henderson, G. McKinnon, T. Y. Lee, and B. K. Rutt. A fast 3d look-locker method for volumetric t1 mapping. *Magn Reson Imaging*, 17(8):1163–71–, 1999.

[39] Liu Hongxing, Wang Lei, and K. C. Jezek. Automated delineation of dry and melt snow zones in antarctica using active and passive microwave observations from space. *Geoscience and Remote Sensing, IEEE Transactions on*, 44(8):2152–2163–, 2006.

[40] A. Houri, A. Bijaoui, and L. Fongang. A texture analysis by mathematical morphology. application to cells discrimination. In *Engineering in Medicine and Biology Society, 1990., Proceedings of the Twelfth Annual International Conference of the IEEE*, pages 163–164–, 1990.

[41] R. B. Inampudi, T. N. Purimetla, and P. V. Suresh. Image compression by morphological operators. In *Geoscience and Remote Sensing Symposium, 2002. IGARSS '02. 2002 IEEE International*, volume 6, pages 3314–3316 vol.6–, 2002.

[42] S. Isenmann, A. Kretz, and A. Cellerino. Molecular determinants of retinal ganglion cell development, survival, and regeneration. *Prog. Retinal Eye Res.*, 22:483–543–, 2003.

[43] H. J. Johnson and G. E. Christensen. Consistent landmark and intensity-based image registration. *IEEE Trans Med Imaging*, 21(5):450–61–, 2002.

[44] D. S. Kang, S. C. Harvey, and R. D. Wells. Diepoxybutane forms a monoadduct with b-form (dg-dc)n.(dg-dc)n and a crosslinked diadduct with the left-handed z-form. *Nucleic Acids Res*, 13(15):5645–56–, 1985.

[45] Y. S. Kang, J. C. Gore, and I. M. Armitage. Studies of factors affecting

the design of nmr contrast agents: manganese in blood as a model system. *Magn Reson Med*, 1(3):396–409–, 1984.

[46] Z. A. Karcioglu. Zinc in the eye. *Surv Ophthalmol*, 27(2):114–22–, 1982.

[47] C. Kobbert, R. Apps, I. Bechmann, J. L. Lanciego, J. Mey, and S. Thanos. Current concepts in neuroanatomical tracing. *Prog Neurobiol*, 62(4):327–51–, 2000.

[48] A.P. Koretsky and A.C. Silva. Manganese-enhanced magnetic resonance imaging (memri). *NMR biomed.*, 17:527–531–, 2004.

[49] P. J. Kostelec, J. B. Weaver, and Jr. Healy, D. M. Multiresolution elastic image registration. *Med Phys*, 25(9):1593–604–, 1998.

[50] R.B. Lauffer. Paramagnetic metal complexed as water proton relaxation agents for nmr imaging: Theory and design. *Chem. Rev.*, 87:901–927–, 1987.

[51] J. H. Lee, A. C. Silva, H. Merkle, and A. P. Koretsky. Manganese-enhanced magnetic resonance imaging of mouse brain after systemic administration of mncl2: dose-dependent and temporal evolution of t1 contrast. *Magn Reson Med*, 53(3):640–8–, 2005.

[52] Y. Lu, T. Jiang, and Y. Zang. Region growing method for the analysis of functional mri data. *Neuroimage*, 20(1):455–65–, 2003.

[53] R. Mallik, B. C. Carter, S. A. Lex, S. J. King, and S. P. Gross. Cytoplasmic dynein functions as a gear in response to load. *Nature*, 427(6975):649–52–, 2004.

[54] G. K. Matsopoulos, K. K. Delibasis, N. A. Mouravliansky, and K. S. Nikita. Automatic medical image registration schemes using global optimization techniques. *Stud Health Technol Inform*, 79:463–91–, 2000.

[55] M.H. Mendonca-Dias, E. Gaggelli, and P.C. Lauterbur. Paramagnetic contrast agents in nuclear magnetic reconance medical imaging. *Semin. Nucl. Med.*, 13:364–376–, 1983.

[56] C. C. Miller, S. Ackerley, J. Brownlees, A. J. Grierson, N. J. Jacobsen, and P. Thornhill. Axonal transport of neurofilaments in normal and disease states. *Cell Mol Life Sci*, 59(2):323–30–, 2002.

[57] S. Minoshima and D. Cross. In vivo imaging of axonal transport using mri: aging and alzheimer's disease. *Eur J Nucl Med Mol Imaging*, 35 Suppl 1:S89–92–, 2008.

[58] M. J. Muller, S. Klumpp, and R. Lipowsky. Tug-of-war as a cooperative mechanism for bidirectional cargo transport by molecular motors. *Proc Natl Acad Sci U S A*, 105(12):4609–14–, 2008.

[59] Wako Nakajima, Akira Ishida, Mary S. Lange, Kathleen L. Gabrielson, Mary Ann Wilson, Lee J. Martin, Mary E. Blue, and Michael V. Johnston. Apoptosis has a prolonged role in the neurodegeneration after hypoxic ischemia in the newborn rat. *J. Neurosci.*, 20(21):7994–8004–, 2000.

[60] K. Narita, F. Kawasaki, and H. Kita. Mn and mg influxes through ca channels of motor nerve terminals are prevented by verapamil in frogs. *Brain Res*, 510(2):289–95–, 1990.

[61] J.A. Nelder and R. Mead. A simplex method for function minimization. *The Computer Journal*, 7(4):308–313–, 1965.

[62] M.T. Nelson. Interactions of divalent cations with single calcium channels from rat brain synaptosomes. *J. Gen. Physiol.*, 87:201–222–, 1986.

[63] W. Nordhoy, H. W. Anthonsen, M. Bruvold, H. Brurok, S. Skarra, J. Krane, and P. Jynge. Intracellular manganese ions provide strong t1 relaxation in rat myocardium. *Magn Reson Med*, 52(3):506–14–, 2004.

[64] R.B. Norgren and M.N. Lehman. Herpes simplex virus as a transneural tracer. *Neurosci. Biobehav. Rev.*, 22:695–708–, 1998.

[65] Emin Oztas. Neuronal tracing. *Neuroanatomy*, 2:2–5–, 2003.

[66] D. Paquin, D. Levy, and L. Xing. Hybrid multiscale landmark and deformable image registration. *Math Biosci Eng*, 4(4):711–37–, 2007.

[67] G. J. Parker, I. Baustert, S. F. Tanner, and M. O. Leach. Improving image quality and t(1) measurements using saturation recovery turboflash with an approximate k-space normalisation filter. *Magn Reson Imaging*, 18(2):157–167, Feb 2000.

[68] R. C. Parodi, F. Sardanelli, P. Renzetti, E. Rosso, C. Losacco, A. Ferrari, F. Levrero, A. Pilot, M. Inglese, and G. L. Mancardi. Growing region segmentation software (gres) for quantitative magnetic resonance imaging of multiple sclerosis: intra- and inter-observer agreement variability: a comparison with manual contouring method. *Eur Radiol*, 12(4):866–71–, 2002.

[69] N. Passat, C. Ronse, J. Baruthio, J. P. Armspach, C. Maillot, and C. Jahn. Region-growing segmentation of brain vessels: an atlas-based automatic approach. *J Magn Reson Imaging*, 21(6):715–25–, 2005.

[70] R. G. Pautler and A. P. Koretsky. Tracing odor-induced activation in the olfactory bulbs of mice using manganese-enhanced magnetic resonance imaging. *Neuroimage*, 16(2):441–8–, 2002.

[71] R.G. Pautler, R. Mongeau, and R.E. Jacobs. In vivo trans-synaptic tract tracing from the murine striatum and amygdala utilizing manganese enhanced mri (memri). *Magn. Reson. Med.*, 50:33–39–, 2003.

[72] C. A. Pelizzari, G. T. Chen, D. R. Spelbring, R. R. Weichselbaum, and C. T. Chen. Accurate three-dimensional registration of ct, pet, and/or mr images of the brain. *J Comput Assist Tomogr*, 13(1):20–6–, 1989.

[73] D. L. Pham, C. Xu, and J. L. Prince. Current methods in medical image segmentation. *Annu Rev Biomed Eng*, 2:315–37–, 2000.

[74] S. Ramon y Cajal. Oxford University Press, London, 1928.

[75] S. L. Reck-Peterson, A. Yildiz, A. P. Carter, A. Gennerich, N. Zhang, and R. D. Vale. Single-molecule analysis of dynein processivity and stepping behavior. *Cell*, 126(2):335–48–, 2006.

[76] 3rd Rice, J. E., R. C. Vannucci, and J. B. Brierley. The influence of immaturity on hypoxic-ischemic brain damage in the rat. *Ann Neurol*, 9(2):131–41–, 1981.

[77] R. Rodriguez, T. E. Alarcon, and O. Pacheco. A new strategy to obtain robust markers for blood vessels segmentation by using the watersheds method. *Comput Biol Med*, 35(8):665–86–, 2005.

[78] J. L. Ross, H. Shuman, E. L. Holzbaur, and Y. E. Goldman. Kinesin and dynein-dynactin at intersecting microtubules: motor density affects dynein function. *Biophys J*, 94(8):3115–25–, 2008.

[79] J. L. Ross, K. Wallace, H. Shuman, Y. E. Goldman, and E. L. Holzbaur. Processive bidirectional motion of dynein-dynactin complexes in vitro. *Nat Cell Biol*, 8(6):562–70–, 2006.

[80] F. Rovetta, S. Catalani, N. Steimberg, J. Boniotti, M.E. Gilberti, M.A. Mariggiò, and G. Mazzoleni. Organ-specific manganese toxicity: A comparative in vitro study on five models exposed to $mncl_2$. *Toxicol. In Vitro*, 21:284–292–, 2006.

[81] S. Roy, P. Coffee, G. Smith, R. K. Liem, S. T. Brady, and M. M. Black. Neurofilaments are transported rapidly but intermittently in axons: implications for slow axonal transport. *J Neurosci*, 20(18):6849–61–, 2000.

[82] T. J. Ruigrok, T. M. Teune, J. van der Burg, and H. Sabel-Goedknegt. A retrograde double-labeling technique for light microscopy. a combination of axonal transport of cholera toxin b-subunit and a gold-lectin conjugate. *J Neurosci Methods*, 61(1-2):127–38–, 1995.

[83] K. S. Saleem, J. M. Pauls, M. Augath, T. Trinath, B. A. Prause, T. Hashikawa, and N. K. Logothetis. Magnetic resonance imaging of neuronal connections in the macaque monkey. *Neuron*, 34(5):685–700–, 2002.

[84] P. Satpute-Krishnan, J. A. DeGiorgis, and E. L. Bearer. Fast anterograde transport of herpes simplex virus: role for the amyloid precursor protein of alzheimer's disease. *Aging Cell*, 2(6):305–18–, 2003.

[85] H. G. Schnack, H. E. Hulshoff Pol, W. F. C. BaarÃ©, M. A. Viergever, and R. S. Kahn. Automatic segmentation of the ventricular system from mr images of the human brain. *Neuroimage*, 14(1):95–104–, 2001.

[86] D. Schonfeld. Morphological processing of medical images: an introduction. In *Circuits and Systems, 1991., IEEE International Sympoisum on*, pages 746–749 vol.1–, 1991.

[87] S. Schupp, A. Elmoataz, R. Clouard, P. Herlin, and D. Bloyet. Mathematical morphology and active contours for object extraction and localization in medical images. In *Image Processing and Its Applications, 1997., Sixth International Conference on*, volume 1, pages 317–321 vol.1–, 1997.

[88] L. Shafarenko, H. Petrou, and J. Kittler. Histogram-based segmentation in a perceptually uniform color space. *Image Processing, IEEE Transactions on*, 7(9):1354–1358–, 1998.

[89] Tang Sheng and Chen Si-ping. Data cleansing based on mathematic morphology. In *Bioinformatics and Biomedical Engineering, 2008. ICBBE 2008. The 2nd International Conference on*, pages 755–758–, 2008.

[90] J. Sijbers, A. J. den Dekker, A. Van der Linden, M. Verhoye, and D. Van Dyck. Adaptive anisotropic noise filtering for magnitude mr data. *Magnetic Resonance Imaging*, 17(10):1533–1539–, 1999.

[91] A. C. Silva and N. A. Bock. Manganese-enhanced mri: an exceptional tool in translational neuroimaging. *Schizophr Bull*, 34(4):595–604–, 2008.

[92] A. Skjold, T. R. Vangberg, A. Kristoffersen, O. Haraldseth, P. Jynge, and H. B. Larsson. Relaxation enhancing properties of mndpdp in human myocardium. *J Magn Reson Imaging*, 20(6):948–52–, 2004.

[93] K. D. Smith, V. Kallhoff, H. Zheng, and R. G. Pautler. In vivo axonal trans-

port rates decrease in a mouse model of alzheimer's disease. *Neuroimage*, 35(4):1401–8–, 2007.

[94] Kirby M. E. Steiner, D. Geometrical referencing of landsat images by affine transformation and overlaying of map data. *Photogrammetria*, 33:41–75–, 1977.

[95] S. W. Sun, H. F. Liang, A. H. Cross, and S. K. Song. Evolving wallerian degeneration after transient retinal ischemia in mice characterized by diffusion tensor imaging. *Neuroimage*, 40(1):1–10–, 2008.

[96] K. Svoboda, C. F. Schmidt, B. J. Schnapp, and S. M. Block. Direct observation of kinesin stepping by optical trapping interferometry. *Nature*, 365(6448):721–7–, 1993.

[97] P. Thompson and A. W. Toga. A surface-based technique for warping three-dimensional images of the brain. *IEEE Trans Med Imaging*, 15(4):402–17–, 1996.

[98] M. Thuen, T. E. Singstad, T. B. Pedersen, O. Haraldseth, M. Berry, A. Sandvig, and C. Brekken. Manganese-enhanced mri of the optic visual pathway and optic nerve injury in adult rats. *J Magn Reson Imaging*, 22(4):492–500–, 2005.

[99] Song Ting, E. D. Angelini, B. D. Mensh, and A. Laine. Comparison study of clinical 3d mri brain segmentation evaluation. In *Engineering in Medicine and Biology Society, 2004. IEMBS '04. 26th Annual International Conference of the IEEE*, volume 1, pages 1671–1674–, 2004.

[100] H. Tjä, lve, C. Mejá, re, and K. Borg-Neczak. Uptake and transport of manganese in primary and secondary olfactory neurons in pike. *Pharmacol. Toxicol.*, 77:23–31–, 1995.

[101] K. G. Toft, S. O. Hustvedt, D. Grant, I. Martinsen, P. B. Gordon, G. A. Friisk, A. J. Korsmo, and T. Skotland. Metabolism and pharmacokinetics of mndpdp in man. *Acta Radiol*, 38(4 Pt 2):677–89–, 1997.

[102] A.W. Toga and R.C. Collins. Metabolic response of optic centers to visual stimuli in the albino rat: Anatomical and physiological considerations. *J. Comp. Neurol.*, 199:443–464–, 1981.

[103] G. Ugarte, F. Perez, and R. Latorre. How do calcium channels transport calcium ions? *Biol Res*, 31(1):17–32–, 1998.

[104] R. D. Vale, B. J. Schnapp, T. S. Reese, and M. P. Sheetz. Organelle, bead, and microtubule translocations promoted by soluble factors from the squid giant axon. *Cell*, 40(3):559–69–, 1985.

[105] R. C. Vannucci and S. J. Vannucci. Perinatal hypoxic-ischemic brain damage: evolution of an animal model. *Dev Neurosci*, 27(2-4):81–6–, 2005.

[106] Susan J. Vannucci and Henrik Hagberg. Hypoxia-ischemia in the immature brain. *J Exp Biol*, 207(18):3149–3154–, 2004.

[107] den Boer J.A. Vlaardingerbroek, M.T. volume Second edition. Springer, Berlin Heidelberg, 1999.

[108] J. Voogd. In *The central nervous system of vertebrates*, pages 1791–1820–. Springer, New York, 1998.

[109] T. Walter, J. C. Klein, P. Massin, and A. Erginay. A contribution of image processing to the diagnosis of diabetic retinopathy-detection of exudates in color fundus images of the human retina. *Medical Imaging, IEEE Transactions on*, 21(10):1236–1243–, 2002.

[110] L. Wang, C. L. Ho, D. Sun, R. K. Liem, and A. Brown. Rapid movement of axonal neurofilaments interrupted by prolonged pauses. *Nat Cell Biol*, 2(3):137–41–, 2000.

[111] Yue J. Wang, Tianhu Lei, Wilfred Sewchand, and Seong K. Mun. Mr imaging statistics and its application in image modeling. In *Medical Imaging 1996: Physics of Medical Imaging*, volume 2708, pages 706–717–, Newport Beach, CA, USA, 1996. SPIE.

[112] Z. Wang and M. P. Sheetz. The c-terminus of tubulin increases cytoplasmic dynein and kinesin processivity. *Biophys J*, 78(4):1955–64–, 2000.

[113] T. Watanabe, T. Michaelis, and J. Frahm. Mapping of retinal projections in the living rat using high-resolution 3d gradient-echo mri with mn2+-induced contrast. *Magn Reson Med*, 46(3):424–9–, 2001.

[114] C. Weidner, D. Miceli, and J. Reperant. Orthograde axonal and transcellular transport of different fluorescent tracers in the primary visual system of the rat. *Brain Res*, 272(1):129–36–, 1983.

[115] E. Weiss, K. Wijesooriya, V. Ramakrishnan, and P. J. Keall. Comparison of intensity-modulated radiotherapy planning based on manual and automatically generated contours using deformable image registration in four-dimensional computed tomography of lung cancer patients. *Int J Radiat Oncol Biol Phys*, 70(2):572–581–, 2008.

[116] J. C. Weng, J. H. Chen, P. F. Yang, and W. Y. Tseng. Functional mapping of rat barrel activation following whisker stimulation using activity-induced manganese-dependent contrast. *Neuroimage*, 36(4):1179–88–, 2007.

[117] D. J. Withey and Z. J. Koles. Medical image segmentation: Methods and software. In *Noninvasive Functional Source Imaging of the Brain and Heart and the International Conference on Functional Biomedical Imaging, 2007. NFSI-ICFBI 2007. Joint Meeting of the 6th International Symposium on*, pages 140–143–, 2007.

[118] R. P. Woods, J. C. Mazziotta, and S. R. Cherry. Mri-pet registration with automated algorithm. *J Comput Assist Tomogr*, 17(4):536–46–, 1993.

[119] S. Worz and K. Rohr. Physics-based elastic image registration using splines and including landmark localization uncertainties. *Med Image Comput Comput Assist Interv Int Conf Med Image Comput Comput Assist Interv*, 9(Pt 2):678–85–, 2006.

[120] D. H. Wu, Y. Guo, C. C. Lu, and J. Suri. Improvement to functional magnetic resonance imaging (fmri) methods using non-rigid body image registration methods for correction in the presence of susceptibility artifact effects. *Conf Proc IEEE Eng Med Biol Soc*, 1:1018–20–, 2006.

[121] A. Yildiz, M. Tomishige, R. D. Vale, and P. R. Selvin. Kinesin walks hand-over-hand. *Science*, 303(5658):676–8–, 2004.

[122] Y. Zeng. Region coding and detail compensation. In *Signal Processing, 1996., 3rd International Conference on*, volume 2, pages 1227–1230 vol.2–, 1996.

[123] S. Zhang, Z. Zhou, and J. Fu. Effect of manganese chloride exposure on liver and brain mitochondria function in rats. *Environ. Res.*, 93:149–157–, 2003.

[124] Yu Zijuan, Zhao Yuqian, and Wang XiaoFang. Research advances and prospects of mathematical morphology in image processing. In *Cybernetics and Intelligent Systems, 2008 IEEE Conference on*, pages 1242–1247–, 2008.

Paper I-II
are not included due to copyright

Manganese transport in the rat optic nerve evaluated with spatial- and time-resolved MRI

Øystein Olsen, MSc[1], Anders Kristoffersen PhD[2], Marte Thuen, PhD[3], Axel Sandvig, MD, PhD[4], Christian Brekken, PhD[3], Olav Haraldseth, MD, PhD[2,3], Pål Erik Goa, PhD[2]

[1]*Department of Radiography, Sør-Trøndelag University College, Trondheim, Norway*

[2]*Department of Radiology, St Olavs Hospital, Trondheim, Norway*

[3]*Department of Circulation and Medical Imaging, Norwegian University of Science and Technology, Trondheim, Norway*

[4] *Department of Laboratory Medicine Children's and Women's Health Norwegian University of Science and Technology, Trondheim, Norway*

Submitted to Journal of Magnetic Resonance Imaging

Abstract

Purpose: 1) To evaluate a novel theoretical model for *in vivo* axonal Mn^{2+} transport with MRI data from the rat optic nerve (ON), and 2); to compare predictions from the new model with previously reported experimental data.

Materials and Methods: Time resolved *in vivo* T_1 weighted MRI of adult female Sprague Dowley rat (n=9) ON was obtained at different time points after intravitreal $MnCl_2$-injection. A concentration dependent and a rate dependent function for the Mn^{2+} retinal ganglion cell (RGC) axon entrance were convolved with three different transport functions and each model system was optimized to fit the ON data.

Results: The rate-limited input function gave a better fit to the data than the concentration-limited input. Simulations showed that the rate-limited input leads to a semi-logarithmic relationship between injected dose and Mn^{2+} concentration in the ON, which is in agreement with previously reported *in vivo* experiments. A random walk transport model and an anterograde predominant slow model gave similar fit to the data, both better than an anterograde predominant fast model.

Conclusion: The results indicate that Mn^{2+} input into RGC axons is limited by a maximum entrance rate into the axons. Also, a wide range of apparent Mn^{2+} transport rates seems to be involved, different from synaptic vesicles transport rates, meaning that manganese does not depict synaptic vesicle transport rates directly.

Introduction

In neurons many proteins are synthesised in the cell body and transported along axons by molecular motors. Kinesin and dynein motor proteins generate force and move along microtubules carrying protein cargos; Kinesin travels from the cell body towards the synapse (anterograde direction) while dynein travels towards the cell body (retrograde direction) (1). In many major human neurodegenerative diseases such as Alzheimer's and Parkinson's disease disruption of the transport processes is an early significant event in the aetiology (2).

Various substances move at different rates independently of the electrical activity within the axons (3,4) and are grouped in fast and slow components with speeds of approximately 4-16mm/h and 4-250μm/h respectively in the healthy axon, (3,5). The same "fast" molecular motors are involved in both fast and slow axonal transport, but during slow axonal transport there are prolonged pauses between periods of movements (6,7). Axon transport of radioactive, fluorescent and non-fluorescent tracers is the basis of axon tracing and may be specific for either antero- or retrograde transport. However, most techniques require tissue sampling (8) and are therefore unsuited for longitudinal real time *in vivo* studies.

Rat optic nerve (ON) axons arise from retinal ganglion cells (RGC) in the eye and project towards the optic chiasm and project through the contralateral optic tract to the superior colliculus (SC) in the mid brain. Hence, ON anterograde transport is from the eye and towards the SC while ON retrograde transport is directed towards the eye. The vitreous body makes a well defined and easily accessible chamber for tracer injection from where a tracer can access the RGC and be transported in their axons in the ON. The uniform orientation of the trajectory of RGC axons in the ON and optic tract makes the visual pathway well suited for axonal transport studies.

Pautler et al. introduced manganese enhanced MRI (MEMRI) as an *in vivo* anterograde central nervous system (CNS) tract tracing technique by injecting an unchelated manganese chloride ($MnCl_2$) solution into the vitreous body of the mouse eye (9). Since then, MEMRI has become an established technique for *in vivo* anatomical CNS tract tracing in various animal models (9-13) and has recently been extended to dynamic tracing (14-16). MEMRI utilizes the paramagnetic property of the manganese ion (Mn^{2+}) and takes advantage of Mn^{2+} being a calcium (Ca^{2+}) analogue in biological systems. Mn^{2+} gives positive contrast on T_1-weigthed images and enters cells through voltage gated Ca^{2+} channels on the cell membrane

(17). A working hypothesis for Mn^{2+} transport is that Mn^{2+} is packaged into vesicles and transported anterogradely along axonal microtubules (18) and released into the synaptic cleft for thereafter to enter post synaptic neurons through voltage gated Ca^{2+} channels (11,19).

One way to describe the Mn^{2+} transport processes is to use the analogy of vesicles being carried on transport belts running in anterograde and retrograde directions. If Mn^{2+} is bound to vesicles until it reaches the synapse, the transport will be described as *convection-like* with either 1) a single velocity if all transport belts run at the same speed or 2), a mean velocity with dispersion if the transport belts run in the same direction at different speeds. However, if Mn^{2+} are loosely bound to the vesicles, detach during transport and re-bind to cargo on the anterograde and/or retrograde running transport belts, the transport resembles that of random walk, also called Brownian motion or diffusion. However, note that the diffusion coefficient now is not that of the Brownian motion of free ions, but rather an apparent or effective transport coefficient.

Even though Mn^{2+} CNS axonal transport rates have been reported in various studies (9-13,16) a more thorough investigation of Mn^{2+} transport which addresses issues like entering of Mn^{2+} into axons, multiple transport rates and axonal clearance are needed before MEMRI has application in *in vivo* studies of neurodegenerative diseases. The previous studies have used two time points and positions to estimate transport rates while several positions and time points are needed to reveal multiple transport rates.

The response of ON contrast to various intravitreal Mn^{2+} doses has been investigated by Thuen et al (20) and a semi-logarithmic relationship between intravitreal Mn^{2+} dose and ON contrast to noise ratio (CNR) has been found. However, the transport mechanisms governing this semi-logarithmic relationship are unknown.

The aims of the present study were to: 1) To evaluate a novel theoretical model for *in vivo* axonal Mn^{2+} transport with MRI data from the rat optic nerve, and 2); to compare predictions from the new model with previously reported experimental data.

Materials and Methods

Animals

Adult female Sprague Dowley rats (n=9) (~200g) were kept in a pathological-free environment on a 12:12 light:dark hours (h) cycle and allowed free access to food and water. All experimental procedures were performed using isoflurane gas anaesthesia (3.5% induction and 1.5% maintenance). Animal experiments were conducted in accordance to the National Ethics Committee for Animal Research approved by the responsible governmental authority.

Intravitreal Mn^{2+} injections

Anesthetized animals were placed in a purpose-built head frame and 3µl of a non-toxic dose of 150nmol $MnCl_2$ was injected through the sclera posterior to the ora serrata of the left eye using a purpose-built injection device consisting of a plastic syringe connected via polyethylene tubing to a glass micropipette with a tip diameter of ~50µm. After the injection the pipette was slowly withdrawn to minimize reflux (21).

Experimental design

Time resolved (15min resolution) *in vivo* MRI was obtained before $MnCl_2$-injection and in the periods 0-6h, 12-30h, 42-44h and 46-48h after $MnCl_2$-injection. Each animal was in the scanner for 2h and eyes were lubricated with Simplex (Ophtha AS, Copenhagen, Denmark) to counteract corneal dehydration. In order to cover the time spans, each animal was scanned 2-4 times throughout the 48h period. For the time period 0-6h 2-4 animals were used to increase the signal to noise ratio (SNR) at each time point while for all other time points one animal was used. More details of the experimental design are given in Figure 1.

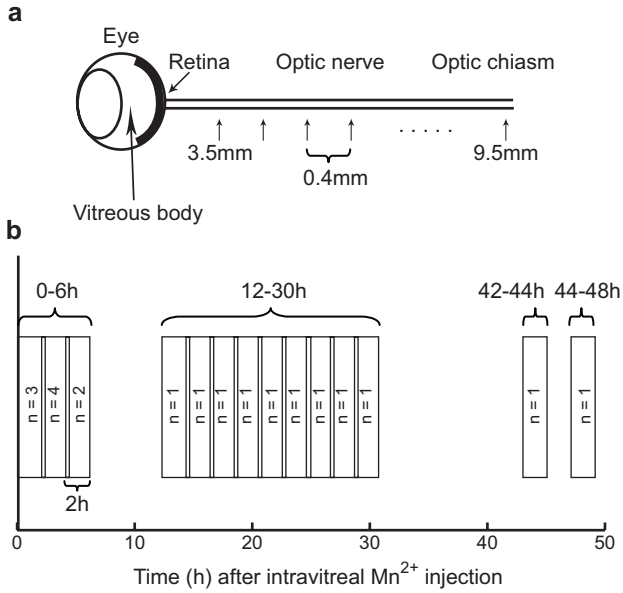

Figure 1*: **a:** The ON was sampled with 0.4 mm resolution from the retina to the optic chiasm every 15min. Data from 3.5mm to 9.5 mm were used in the analysis. **b:** To cover the first 6h of Mn^{2+} transport 2-4 animals were used (0-2h: n=3, 2-4h: n=4 and 4-6h: n=2), while for the 12-30h period one animal was used for each time point with overlapping time slots.*

MEMRI

MEMRI was performed at 7T using a Bruker Biospec Avance 70/20 (Bruker Biospin, Ettlingen, Germany) with Water-cooled BGA-12 (400mT/m) gradients. A 72mm volume coil was used for transmission and an actively decoupled quadrature rat head surface coil was used for receive-only. During scanning, the anesthetized rats lay prone in a dedicated animal bed heated with circulating water at 37°C. To plan a 3D data set, a gradient-echo pilot scan consisting of three orthogonal slice packages (five slices per package) was obtained using field of view (FOV) =5x5cm^2, matrix =128x128, repetition time (TR) =200ms, and echo time (TE)=5ms.

The 3D dataset was obtained using a centric reordered saturation recovery turbo-FLASH sequence, with saturation delay=500ms, flip angle=15°, TE/TR=2.7/9.25ms, echo train length 445ms and number of segments=4. An oblique acquisition matrix of 192x192x66 voxels was placed 45° to the rostral-caudal direction. With a field of view of 3.5x3.5x2.64cm^3, the resolution was 182x182x400µm^2. The sequence was repeated every 15min over the 2h period the animal was in the scanner.

Image processing

The co-ordinates of the centre of the left ON were manually identified in each slice perpendicular to the nerve from the retina to the optic chiasm. The set of co-ordinates were re-sampled with 0.2mm resolution by tri-linear interpolation which gave an intensity curve of the ON for each scan. The intensities were normalized to the signal from a ROI placed in tissue in the same anatomical position in each animal and integrated in 1mm steps. Data from the 12-48h period were averaged along the time dimension (45min window size) to increase signal to noise ratio. To construct approximated Mn^{2+} concentration curves, $SI_c(x)$, a mean intensity curve of ON data before Mn^{2+} injection was calculated and subtracted from the post Mn^{2+} injection curves. The approximated Mn^{2+} concentration curves were placed in a position-time matrix, $SI_c(x,t)$, for model fitting. In addition, the vitreous body intensity was extracted and normalized, and the time constant for vitreal clearance was calculated based on a mono-exponential fit to the vitreous body data. The data were post processed using Matlab® (R14 SP3, MathWorks Inc., Natick MA, USA).

Description of the Mn^{2+} transport model system

The model system we used consisted of three elements as shown in Figure 2: 1), the vitreous body and retina, where Mn^{2+} is initially injected and subsequently cleared through blood vessels and transport into the RGC axons; 2) The input function $u(t)$ describing how Mn^{2+} enters the RGC axon as a function of time, and 3), the ON in which the Mn^{2+} is transported along RGC axons. The ON is mathematically represented by a transport function $p(x,t)$ describing how an input of Mn^{2+} at time zero is transported and distributed along the ON at all later time points. This transport function is analogous to what is often referred to as the impulse response or Green's function of a system. The total Mn^{2+} concentration $c_{mod}(x,t)$ along the ON at any time point is then given by the mathematical convolution between the input function and the transport function, as shown in Eq.1:

$$c_{\mathrm{mod}}(x,t) = a\int_0^t u(\tau)\,p(x,t-\tau)\,d\tau \qquad (1)$$

where a is a scaling factor which includes the dose of injected Mn^{2+} and the cross-sectional area of the ON. The scaling factor was included in the input function in the parameter optimization. For Eq.1 to be valid, one must assume that the biological system is both linear and time-invariant.

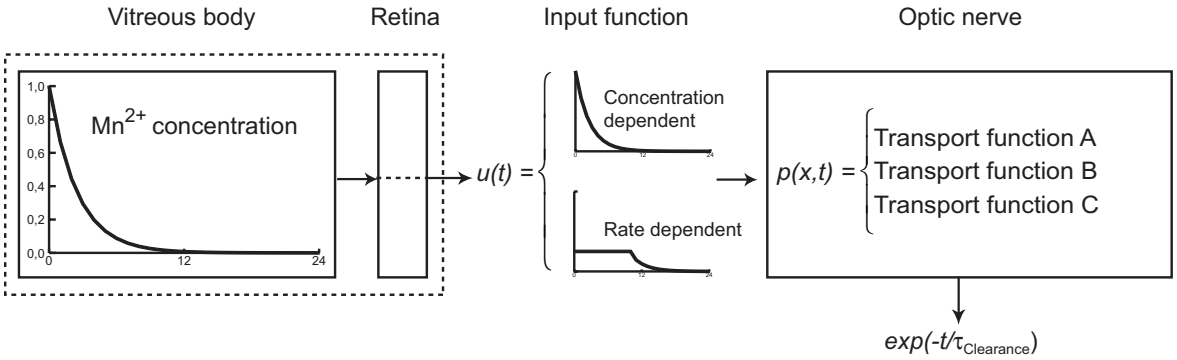

Figure 2: *After injection of $MnCl_2$ into the vitreous body, intravitreal Mn^{2+} concentration gradually decreases as Mn^{2+} enters the retina (retinal compartment) by diffusion and then passes through Ca^{2+} channels to enter RGC. Entering of Mn^{2+} into RGC axons is described by the input function u(t) where the input could either be Mn^{2+} concentration dependent, or uptake rate dependent. Inside RGC axons, the transport is described by the transport function p(x,t). ON clearance is described by an exponential decay function with time constant $\tau_{Clearance}$. The ON Mn^{2+} concentration is given by the mathematical convolution of the input function and the transport function.*

Vitreal clearance

A mono-exponential fit was made to the vitreous body time-intensity curve to obtain the vitreous body clearance rate. Data points in the interval 0 – 30min were excluded to allow Mn^{2+} to distribute in the vitreous body.

Input functions

Two input functions were evaluated. 1): The *concentration-dependent* input function which equalled the Mn^{2+} concentration time-curve in the vitreous body as found from the above mono-exponential fit. This describes the case where the entrance of Mn^{2+} is determined by the available amount of Mn^{2+}, i.e. the Mn^{2+} concentration. 2): The *rate-dependent* input function which is constant for a given time followed by a mono-exponential decay. This describes the case when the uptake of Mn^{2+} into the RGC axons is limited by a maximum rate. The same time-constant as for vitreal clearance of Mn^{2+} was used to describe the mono-exponential decay part of this input function.

Transport functions

Three different transport functions were tested: A), Single component anterograde convection together with random walk and clearance as described in (15) and (16); B) Pure anterograde convection with a majority of fast velocity components, and C) Pure anterograde convection with a majority of slow velocity components. Transport function A was recently used in

studies of age-related axonal transport rates (16) and Alzheimer's disease (15) and describes loosely bound Mn^2 in a uniform translation with a single velocity in one direction and random walk transport in both directions. For functions B and C a distribution of velocities was assumed instead of single components. As transport function B the Rice distribution was used (Figure 3a), which has very few components close to zero even for the minimum average velocity. For higher average velocity it resembles a Gaussian distribution. As transport function C an exponential velocity distribution was used, which has the majority of velocity components towards zero (Figure 3a). See Appendix A for more details.

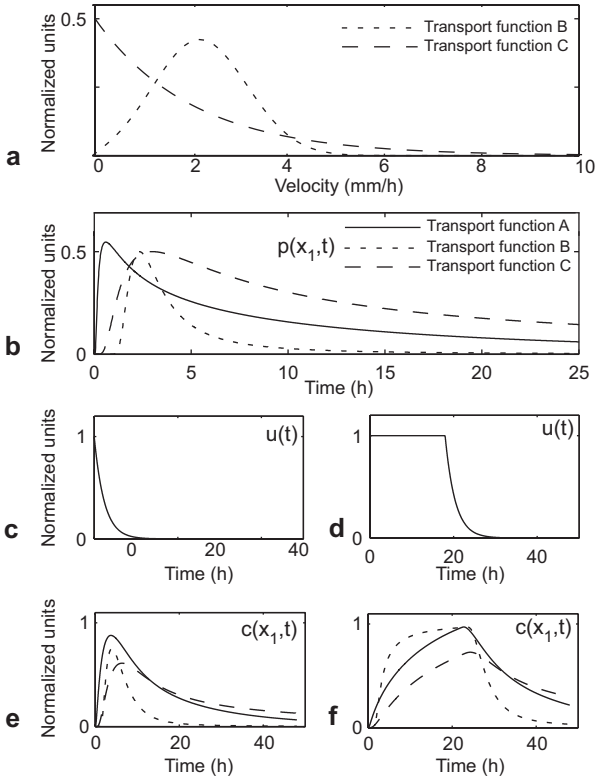

Figure 3: ***a:*** *Velocity distributions of transport functions B and C with mean velocity 2mm/h. Transport model B has very few components close to zero while transport function C has the majority of velocity components towards zero. Transport function A consisted of a single velocity with bi-directional random walk and as such, did not have a specific distribution of velocities* ***b:*** *Plot of transport functions A, B and C with comparable model parameters. The curves describe the concentration as a function of time at a given position x_1 in the ON after an instantaneous injection of Mn^{2+}.* ***c:*** *The concentration dependent input function.* ***d:*** *The rate dependent input function.* ***e:*** *Simulated concentration curves from the convolution of transport functions (b) and the concentration limited input function (c).* ***f:*** *Simulated concentration curves from the convolution of transport models (b) and the rate limited input function (d).*

Model prediction of two-point velocity and dose-concentration relationship

The injected dose of Mn^{2+}, the input function and the transport function determine how the Mn^{2+} concentration in the ON develops (Eq.1). Figure 3 b-f show a simulation of how the convolution of the transport functions A, B and C with the concentration dependent and the rate dependent input functions generates different concentration curves after an arbitrary dose of Mn^{2+}. We simulated ON Mn^{2+} concentration for eight different intravitreal Mn^{2+} doses to investigate the model predictions of dose-concentration relationship in the ON 3mm from the retina 24h after intravitreal Mn^{2+} injection.

The two-point method used in previous studies to estimate apparent transport velocity was based on measurements of the time taken for the MEMRI signal to reach a specific level (e.g. detection level) at a given position from the Mn^{2+} injection site, or at two different positions. We applied the two-point method to the modelled ON concentration curves at three different positions and levels of Mn^{2+} concentrations to compare our models with previous data and to investigate if choice of detection level and spacing of measurements would impact the results.

Model fitting

Data from the first part of the ON (0-3.5mm) and beyond 9.5mm were excluded from the fit because of motion artefacts close to the eye and to avoid the optic chiasm (~10mm) where the ON from both eyes meet and the axon density within each voxel probably change.

The models (Appendix A: Eq.6 - Eq.8) were fitted to the ON data $SI_c(x,t)$ by optimizing the model parameters in order to minimize the L_1 and L_2 norm. Generally, the L_p norm is given by:

$$L_p = \left(\sum_{i,j} abs[c_{\mathrm{mod}}(x_i,t_j) - SI_c(x_i,t_j)]^p \right)^{\frac{1}{p}} \quad p \geq 1 \tag{2}$$

The norm described the difference between the observed data and a model, and the optimized model which gave the smallest norm (difference) fitted the data best. The L_2 norm (p=2) equals the least square fit but is more sensitive to outliers than the L_1 norm. Both norms were used to evaluate the impact of choice of norm on the optimized model parameters. The optimizing was done using a build-in Matlab routine which utilizes the Nelder-Mead simplex method (22). The search was repeated 50 times for each model with randomly selected initial conditions to increase the probability of finding the global minimum. The mean and standard deviation (SD) of the seven best sets of model parameters (smallest L_1/L_2 norms) were

calculated. The SD reflects the variation of estimated model parameters as a function of initial conditions and SD = 0 indicates that the global minimum has been found while a large SD indicates one or several local minima among the seven best fits. The fits were also inspected visually since even though a small norm indicates a good overall fit, parts of the fit may not describe the data well.

Results

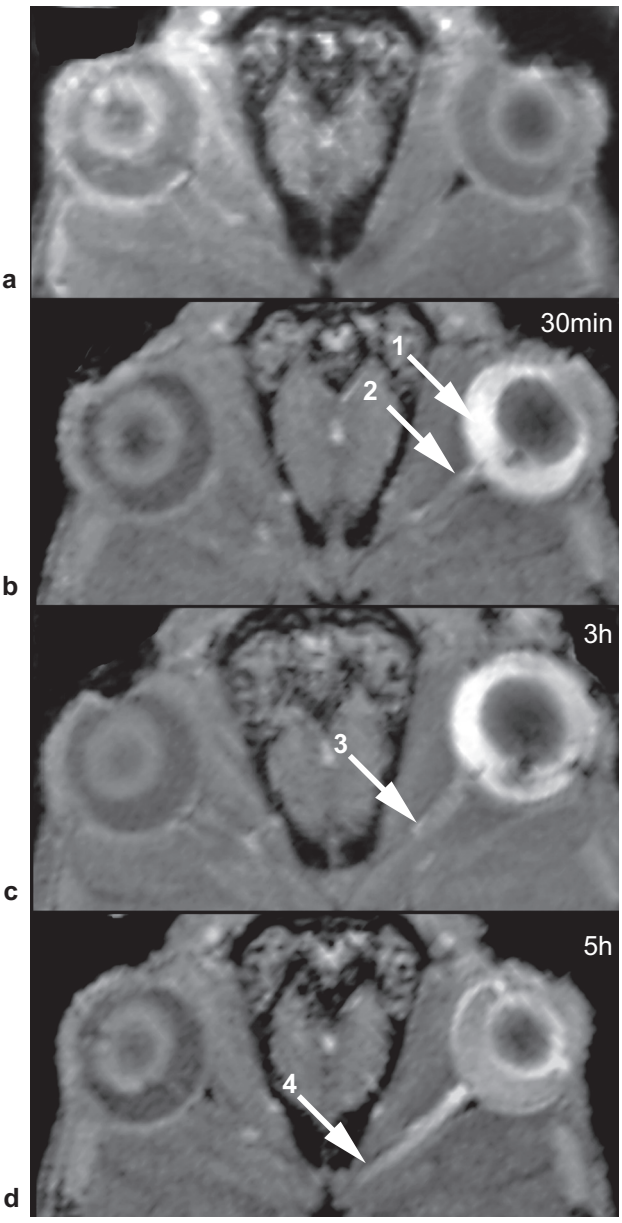

Figure 4: *MRI of left eye and ON before (a) and 30min (b), 3h (c) and 5h (d) after intravitreal injection of 3µl 50nM $MnCl_2$. The enhancement in the vitreous body (1) gradually decreased as Mn^{2+} enhancement increased along the ON (2-4).*

Figure 4 shows example MR images of the eye and ON before, and at different time points after intravitreal injection of $MnCl_2$ into the vitreous body. While the intravitreal Mn^{2+} concentration gradually decreased, Mn^{2+} entered the RGC axons and were transported along the ON.

Vitreal clearance

The vitreous body data are plotted as function of time in Figure 5. The mono-exponential fit to the vitreous body data gave a time constant for vitreous body Mn^{2+} clearance of 2.46h.

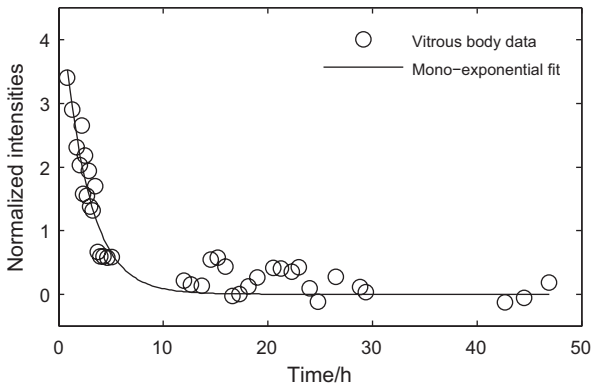

Figure 5: *Mono-exponential fit to the vitreous body data time intensity curve.*

Input functions

Figure 6 shows the best fit of model to data for transport function A convolved with the concentration-dependent and the rate-dependent input functions. For the concentration dependent input function, the model (solid line) overestimated the Mn^{2+} concentration close to the retina (Figure 6b) while underestimating the Mn^{2+} concentration further away from the retina (Figure 6d) over the first 10h after $MnCl_2$ injection. For the rate dependent input function, the model gave a better fit along the whole ON (3.5mm-9.5mm) (Figure 6f-h) at early time points. The results were similar when using transport functions B and C.

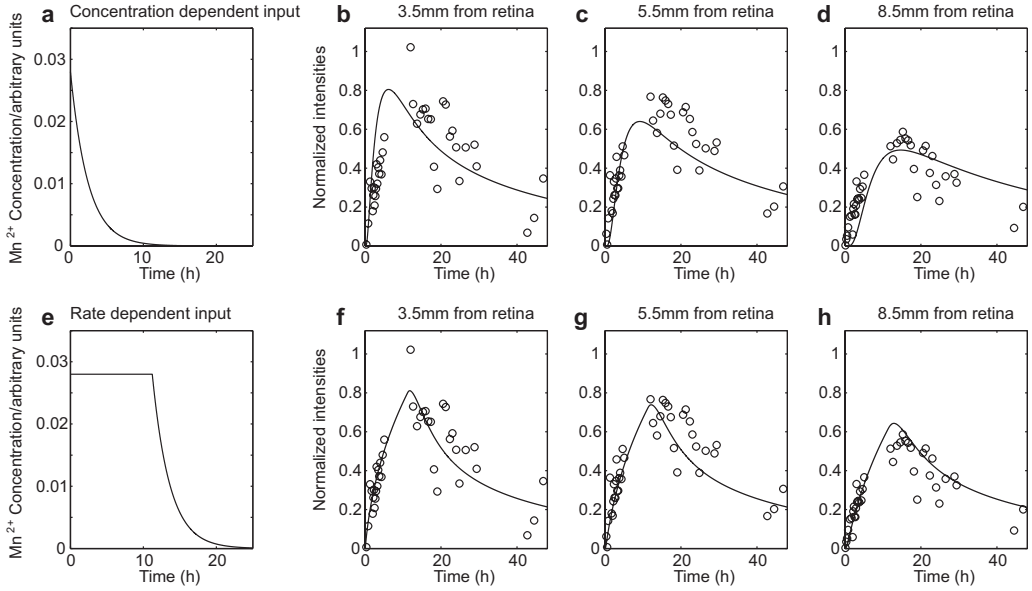

Figure 6: ***b-d:*** *Best fit for transport function A with the concentration dependent input function (a). Note how the model (solid line) rises too fast compared to the data (open dots) 3.5mm from the retina (b) while it rises too slow at 8.5mm from the retina (d) over the first 10h after $MnCl_2$ injection. At 5.5mm from the retina, the model fits the data well (c).* ***f-h:*** *Best fit of transport function A together with the rate dependent input function (e).*

Transport functions

The convolution of three different transport functions with to different input functions generated six *transport models*. Transport function A, B and C convolved with the rate dependent input function constituted transport model A, B and C, respectively, while convolved with the concentration dependent input function, transport model A, B and C constituted transport model D, E and F. Table 1 gives the L_1 and L_2 optimized model parameters for the different models and Figure 7 shows the best fit of model A, B and C at

3.5, 5.5, 7.5 and 9.5mm from the retina. Table 2 gives apparent transport velocities for the L_2 optimized models A, B and C based on the two-point method used in previous studies.

Table 1 Summary of the results from model fitting with the rate dependent and concentration dependent input function. The numbers indicate the mean of the seven best sets of model parameters with standard deviations in brackets.

Input function	Transport function	Transport model	Norm [a] (% SD)		v [b] (% SD) (mm/h)		D [c] (% SD) (mm^2/h)		σ [d] (%SD) (mm/h)		$\tau_{clearance}$ [e] (%SD) (h)		$t_{admission}$ [f] (%SD) (h)	
			L_1	L_2	L_1	L_2	L_1	L_2	L_1	L_2	L_1	L_2	L_1	L_2
Rate dependent	A	A	21.7 (0.3)	1.67 (0.4)	0.01 (264)	0.00 (185)	57.8 (33)	30.5 (21.5)	-	-	86.1 (19.5)	110 (36.4)	13.2 (9.6)	11.2 (5.8)
	B	B	27.2 (0.9)	2.02 (1.1)	0.15 (246)	0.28 (154)	-	-	2.78 (2.1)	2.85 (6.0)	infinite	infinite	23.4 (3.0)	26.1 (2.7)
	C	C	21.5 (0.0)	1.75 (0.0)	10.6 (1.8)	12.5 (0.0)	-	-	-	-	infinite	infinite	19.4 (0.6)	20.1 (0.0)
Concentration dependent	A	D	33.8 (1.4)	2.44 (1.0)	0.26 (32)	0.29 (11.4)	2.98 (16.2)	2.52 (8.3)	-	-	infinite	infinite	-	-
	B	E	73.8 (5.2)	5.15 (2.0)	0.21 (86,7)	0.19 (154)	-	-	1.12 (27.2)	1.00 (0.5)	infinite	infinite	-	-
	C	F	32.5 (1.0)	2.40 (1.9)	0.99 (6.6)	0.87 (6.5)	-	-	-	-	infinite	infinite	-	-

[a] *L_1 and L_2 norm.*

[b] *Mean velocity except for the convection random walk model which includes only a single velocity*

[c] *Apparent diffusion coefficient*

[d] *Velocity dispersion parameter*

[e] *Time constant for exponential clearance of Mn^{2+} from the ON*

[f] *Time of constant entry of Mn^{2+} into RGC axons*

The model fitting resulted in the smallest L_1 norm for model C (L_1=21.5) which was only slightly better than model A (L_1=21.7). The L_2 norm optimization gave the smallest norm for model A (L_2=1.67) while model B had larger norms than both model A and C (L_1=27.2/ L_2=2.02). The L_1 and L_2 norms for model D, E and F were larger than any of the corresponding norms of model A, B or C. The mean transport velocity was ~11mm/h for model C while both model A and B gave a velocity parameter close to zero. Note that this does not indicate zero transport but the centre of the velocity distributions. L_1 and L_2 optimization resulted in similar model parameters except for the apparent diffusion coefficient

D (random walk transport coefficient) where L_1 and L_2 -optimization differed almost by a factor of two (D=57.8mm^2/h and D=30.5mm^2/h, respectively).

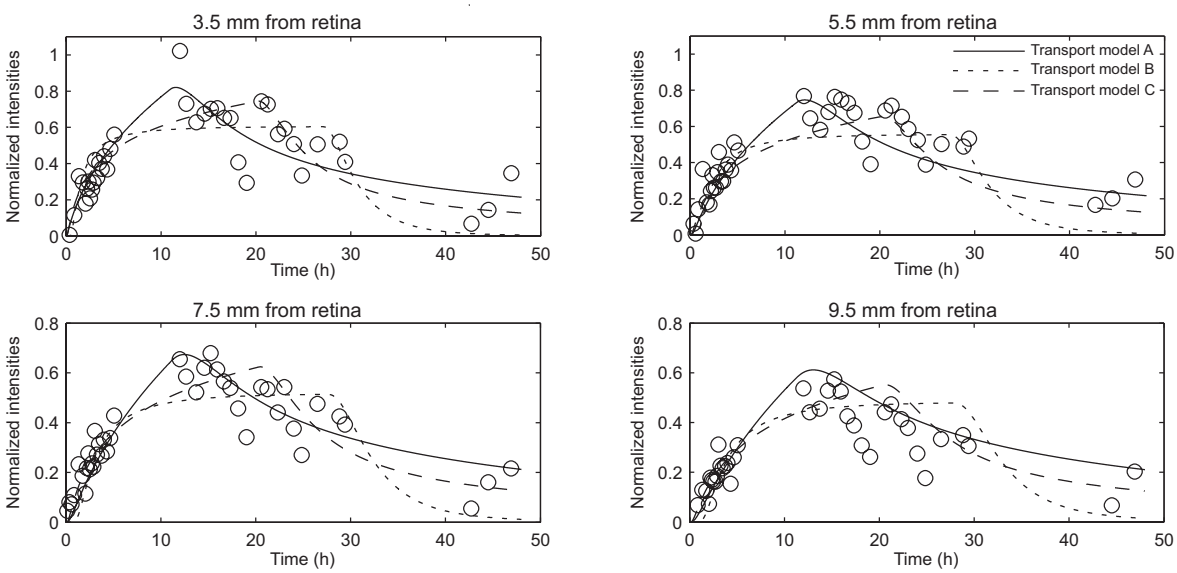

Figure 7*: Best fit for transport models A, B and C at 3.5, 5.5, 7.5 and 9.5mm from the retina based on L_2 optimization.*

Table 2 Apparent transport velocities based on the time to reach various optic nerve Mn^{2+} concentrations at 3.5mm, 5.5mm and 7.5mm from the retina (L_2 optimized data).

Transport model	Optic nerve Mn^{2+} concentration (arbitrary units)	Time (t) to reach Mn^{2+} concentration at a given position[a] (h)			Apparent velocity (mm/h)			Apparent Velocity (mm/h)	
		a=3.5 mm	b=5.5mm	c=7.5mm	a/t	b/t	c/t	(b-a)/Δt	(c-b)/ Δt
A	0,2	1,33	1,93	2,59	2,6	2,8	2,9	3,3	3,0
	0,4	3,53	4,61	5,77	1,0	1,2	1,3	1,9	1,7
	0,5	5,02	6,35	7,77	0,7	0,9	1,0	1,5	1,4
B	0,2	1,11	1,74	2,38	3,2	3,2	3,2	3,2	3,2
	0,4	2,05	3,22	4,41	1,7	1,7	1,7	1,7	1,7
	0,5	3,10	4,88	6,66	1,1	1,1	1,1	1,1	1,1
C	0,2	1,05	1,66	2,26	3,3	3,3	3,3	3,3	3,3
	0,4	3,40	5,33	7,27	1,0	1,0	1,0	1,0	1,0
	0,5	5,78	9,08	12,38	0,6	0,6	0,6	0,6	0,6

[a] *Positions along the optic nerve measured from the retina*

Model prediction of dose-concentration relationship

Figure 8 show the simulated Mn^{2+} concentrations in the ON 3mm from the retina 24h after intravitreal Mn^{2+} injection for a given set of comparable model parameters. The simulations showed a linear relationship between intravitreal Mn^{2+} dose and ON Mn^{2+} concentration 24h after intravitreal injection when the concentration dependent input function was used. The rate dependent input function resulted in near semi-logarithmic relationship between intravitreal dose and ON Mn^{2+} concentration.

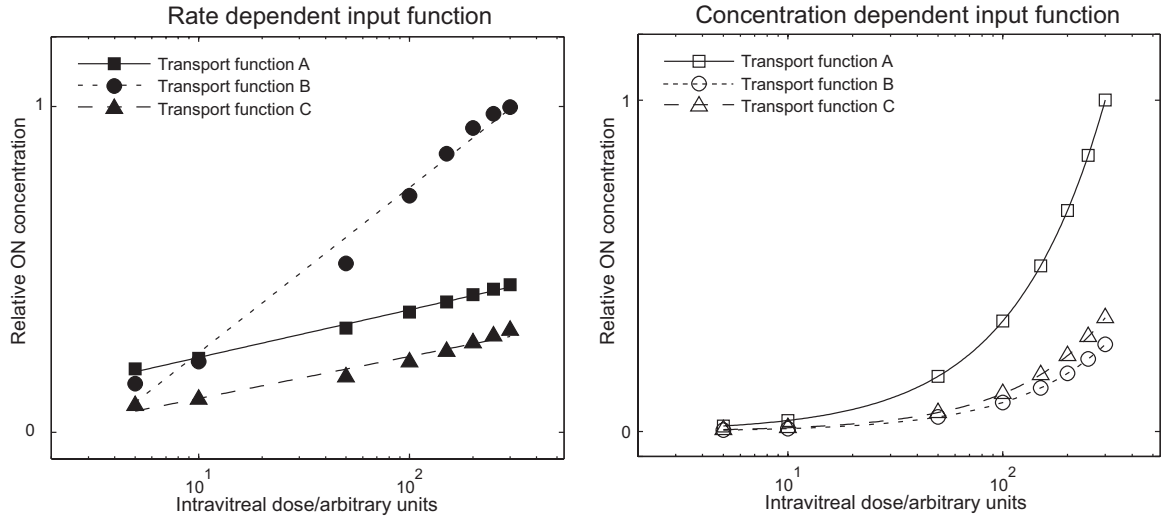

Figure 8: *Simulated Mn^{2+} concentrations in the ON 3mm from the retina 24h after intravitreal Mn^{2+} injection using doses 1, 2, 10, 20, 30, 40, 50 and 60 times an arbitrary reference dose and comparable model parameters. Simulations with the rate dependent input function and transport function A, B and C gave a semi-logarithmic relationship (R^2=0.99, R^2=0.98 and R^2=0.97 for transport function A, B and C, respectively), while simulations with the concentration dependent input function showed a linear relationship between intravitreal Mn^{2+} dose and ON Mn^{2+} concentration (R^2=1.00 for all transport functions). Similar results were obtained within a range of model parameters, including the optimized parameters from the model fitting.*

Discussion

The main result from this study is that the input of Mn^{2+} into RGC axons seems to be limited by a maximum entrance rate rather than the vitreal concentration of Mn^{2+}. This conclusion is supported both by the model fitting to the experimental data in this study and the simulations of the dose-concentration relationship. A semi-logarithmic relationship between intravitreal Mn^{2+} dose and ON contrast to noise ratio (CNR) has earlier been reported from *in vivo* MEMRI of the rat visual system by Thuen et al. (20) and correspond well with our simulations with a rate dependent input function (Figure 8). The L_1 and L_2 norm from the model optimization clearly indicated that the rate limited input function gave best fit (Table 1).

The input of Mn^{2+} into RGC is through voltage gated Ca^{2+} channels, but little is known about transit time of Mn^{2+} in RGC somata before axon transportation. Neither is it known if Mn^{2+} accumulates in RGC somata before/while it is transported in axons nor if it is a linear relationship between Mn^{2+} entering RGC and the transport of Mn^{2+} away from the cell body by anterograde axonal transport. The limited input of Mn^{2+} into the ON could be caused either by restricted Mn^{2+} vesicle packing in RGC somata, or by restricted Mn^{2+} transport through the voltage gated Ca^{2+} channels, or a combination of the two. Ca^{2+} channels have an ion turnover rate of approximately $3 \cdot 10^6$ Ca^{2+} ions/s (23) which means that there is a plateau of ion transport into the cell which could account for the observed restricted input. The time of which the retina is enhanced after vitreal clearance may indicate intracellular retinal storage of Mn^{2+} which could mean that the rate limited input we observe is caused by restricted Mn^{2+} vesicle packing. Future work should include a more comprehensive and detailed analysis of these mechanisms.

An interesting and important observation from the above finding is that is not the injected dose as such that determines the degree of manganese enhancement in the ON, but the duration of which Mn^{2+} is available from the vitreous body. The toxicity of Manganese is well known and limits the dose used in MEMRI (21). If indeed the manganese enhancement is uptake rate limited, one should be able to achieve increased manganese enhancement by using a slow release contrast agent with a release rate tuned to the uptake threshold, and at the same time maintain the local concentration safely below toxic levels. Moreover, this result suggests that changes in dose-contrast relationship can be used to reveal information on how neurodegenerative diseases affect the entering mechanisms of Mn^{2+} into RGC axons.

For the three different transport functions the results are less conclusive For model A, which consisted of a single velocity convective component together with random walk and a clearance factor, the best fit was found when the convection velocity was set to zero and the clearance time constant was set to around 100 h. In practice this means that model A was reduced to a pure random-walk model with an effective diffusion constant in the range 30-60 mm^2/h. Model A had the smallest L_2-norm but the large SD for the optimized parameters which indicated several local minima among the seven best fits. For model B, which consisted of pure anterograde convection with a rician distribution of velocities, the best fit was found for a mean and dispersion velocity of 0.15-0.28 mm/h and 2.78-2.85 mm/h respectively. Also here, large SD of the optimized mean velocity indicates that there was not a stable global minimum for this model. For model C, which consisted of pure anterograde convection with an exponential distribution of velocities, the best fit was found for a mean velocity of 10-12 mm/h. Model C had the smallest L_1-norm (Table 1) and explained the data with only one transport parameter (mean velocity) which is one parameter less than Model A and B. From a modelling viewpoint this is an attractive feature. Overall, model A and model C both described the data reasonably well, although they are based on different transport functions. We interpret this as being a result of limited temporal and spatial extent in the experimental data.

The optimized versions of both model A and model C involves a combination of slow and fast transport, although the detailed velocities and mechanisms involved cannot be extracted from this study. Furthermore, model B which involved a mean velocity with a gaussian spread was forced into a regime where it had a broad distribution of velocities. Hence none of the optimized models supports an interpretation where the transport velocity is well defined, as it would be if Mn^{2+} is tightly bound to its cargo. On the other hand, the observed wide range of effective velocities is in agreement with a transport process where Mn^{2+} are loosely bound during transport, fall off, and then re-bind to either anterograde only moving cargos (model C) or both anterograde and retrograde moving cargos (model A).

The apparent transport velocities for model A, B and C estimated with the two-point method (Table 2) showed that the reference level was an important factor as the apparent transport velocity increased as the reference level decreased. This could account for some of the spread

of reported apparent Mn^{+2} transport velocities in CNS axons estimated as 2.8mm/h in rat ON (13), 2mm/h in the mouse ON (9), 2.1-2.6mm/h and 4.6-6.1mm/h in the rat (sub)cortical structures and corticofugal pathways (10), 4mm/h in the rat olfactory bulb (16), 0.64-1.42mm/h in the Macaque monkey striatum (11) and 2-6mm/h in a songbird brain (12). Furthermore, the apparent transport velocity did not seem to reflect the mean of the velocity distributions. For model B and C the apparent transport velocity was 3.2mm/h and 3.3mm/h at a given reference level whereas the mean of their velocity distributions was ~0.2mm/h and ~10mm/h, respectively. Another interesting observation from the apparent transport velocity estimation is the behaviour of random walk transport. Generally, with random walk like transport, the apparent velocity will depend upon the selected spatial spacing of measurements, with the apparent velocity becoming lower as the spacing of the two measurement points is increased. However, in the case with a rate limited input function, a random walk model may show the opposite behaviour (Table 2, model A). A thorough investigation of apparent velocities was outside the scope of this study but this behaviour seems to be connected to the rate limited input function.

In conclusion, RGC axonal entrance of Mn^{2+} is rate dependent and not directly proportional to the vitreal concentration, suggesting that increased Manganese enhancement could be achieved using a slow-release contrast agent without reaching toxic levels of local concentrations. Also, a wide range of apparent Mn^{2+} transport rates seems to be involved, different from synaptic vesicles transport rates, meaning that manganese does not depict synaptic vesicle transport rates directly. Furthermore, our study illustrates that with spatial- and time resolved in vivo MEMRI it is possible to assess different aspects of axonal transport kinetics, and this suggests that changes in axonal Mn^{2+} entrance and transport rate distributions can be used to reveal new information about how white matter disease affects axonal transport.

Acknowledgements

We thank Dr. Martin Berry for fruitful discussions on axonal transport and comments on the manuscript. This work was carried out using the intellectual and technical resources of the FUGE (Functional genomics in Norway) platform.

Appendix A

Generally, a transport function, *p,* with only one velocity can be written:

$$p(x,t;v) = \delta(x - vt) \tag{3}$$

where δ is delta function, *x* position, *v* velocity and *t* time. If the transport function contains several velocities described by a velocity distribution function $\rho(v;s)$ where *s* is a set of parameters, the averaged transport function can be written:

$$p(x,t;s) = \int p(x,t;v)\,\rho(v;s)\,dv \tag{4}$$

Function (4) describes the transport of a tracer based on a spectrum of transport velocities. To further model the transport, we included exponential clearance of the tracer:

$$p(x,t) = \exp(-t/\tau_{clearance}) \int p(x,t;v)\,\rho(v)\,dv \tag{5}$$

where $\tau_{clearance}$ is the time-constant for exponential clearance of the tracer from the ON.

The following velocity distributions were used to test convection-like transport:

1. The exponential distribution

$$\rho(v) = \frac{1}{v_0}\exp\left(-\frac{v}{v_0}\right) \quad v \geq 0 \tag{6}$$

where v_0 is the mean velocity.

2. The Rice distribution

$$\rho(v) = \frac{v}{\sigma^2} \exp\left(\frac{-(v^2 + \mu^2)}{2\sigma^2} \right) I_0\left(\frac{v\mu}{\sigma^2} \right) \quad v > 0 \tag{7}$$

where σ and μ are distribution parameters, and I_0 is the modified Bessel function of the first kind with order zero.

In addition to these velocity distributions, a one dimensional convection-diffusion transport function recently used in studies of age-related axonal transport rates (16) and Alzheimer's disease (15) was tested. The transport function can be written:

$$p(x,t) = \begin{cases} \frac{1}{\sqrt{4\pi D t}} \exp\left(-\frac{(x - v_0 t)^2}{4Dt} \right) \cdot \exp\left(-\frac{t}{\tau_{clearance}} \right) & x \geq 0 \\ 0 & x < 0 \end{cases} \tag{8}$$

where v_0 is the transport velocity, D is the diffusion coefficient and $\tau_{clearance}$ is the time-constant for exponential clearance of tracer from the ON. The model describes an overall transport with a single velocity in one direction with diffusion like transport in both directions.

References

1. Goldstein LS, Yang Z. Microtubule-based transport systems in neurons: the roles of kinesins and dyneins. Annu Rev Neurosci 2000;23:39-71.
2. De Vos KJ, Grierson AJ, Ackerley S, Miller CC. Role of axonal transport in neurodegenerative diseases. Annu Rev Neurosci 2008;31:151-173.
3. Oztas E. Neuronal tracing. Neuroanatomy 2003;2:2-5.
4. Bearer EL, Falzone TL, Zhang X, Biris O, Rasin A, Jacobs RE. Role of neuronal activity and kinesin on tract tracing by manganese-enhanced MRI (MEMRI). Neuroimage 2007;37 Suppl 1:S37-46.
5. Elluru RG, Bloom GS, Brady ST. Fast axonal transport of kinesin in the rat visual system: functionality of kinesin heavy chain isoforms. Mol Biol Cell 1995;6(1):21-40.
6. Wang L, Ho CL, Sun D, Liem RK, Brown A. Rapid movement of axonal neurofilaments interrupted by prolonged pauses. Nat Cell Biol 2000;2(3):137-141.
7. Roy S, Coffee P, Smith G, Liem RK, Brady ST, Black MM. Neurofilaments are transported rapidly but intermittently in axons: implications for slow axonal transport. J Neurosci 2000;20(18):6849-6861.
8. Kobbert C, Apps R, Bechmann I, Lanciego JL, Mey J, Thanos S. Current concepts in neuroanatomical tracing. Prog Neurobiol 2000;62(4):327-351.
9. Pautler RG, Silva AC, Koretsky AP. In vivo neuronal tract tracing using manganese-enhanced magnetic resonance imaging. Magn Reson Med 1998;40(5):740-748.
10. Leergaard TB, Bjaalie JG, Devor A, Wald LL, Dale AM. In vivo tracing of major rat brain pathways using manganese-enhanced magnetic resonance imaging and three-dimensional digital atlasing. Neuroimage 2003;20(3):1591-1600.
11. Saleem KS, Pauls JM, Augath M, et al. Magnetic resonance imaging of neuronal connections in the macaque monkey. Neuron 2002;34(5):685-700.
12. Van der Linden A, Verhoye M, Van Meir V, et al. In vivo manganese-enhanced magnetic resonance imaging reveals connections and functional properties of the songbird vocal control system. Neuroscience 2002;112(2):467-474.
13. Watanabe T, Frahm J, Michaelis T. Functional mapping of neural pathways in rodent brain in vivo using manganese-enhanced three-dimensional magnetic resonance imaging. NMR Biomed 2004;17(8):554-568.
14. Smith KD, Kallhoff V, Zheng H, Pautler RG. In vivo axonal transport rates decrease in a mouse model of Alzheimer's disease. Neuroimage 2007;35(4):1401-1408.
15. Minoshima S, Cross D. In vivo imaging of axonal transport using MRI: aging and Alzheimer's disease. Eur J Nucl Med Mol Imaging 2008;35 Suppl 1:S89-92.

16. Cross DJ, Flexman JA, Anzai Y, Maravilla KR, Minoshima S. Age-related decrease in axonal transport measured by MR imaging in vivo. Neuroimage 2008;39(3):915-926.
17. Narita K, Kawasaki F, Kita H. Mn and Mg influxes through Ca channels of motor nerve terminals are prevented by verapamil in frogs. Brain Res 1990;510(2):289-295.
18. Pautler RG, Koretsky AP. Tracing odor-induced activation in the olfactory bulbs of mice using manganese-enhanced magnetic resonance imaging. Neuroimage 2002;16(2):441-448.
19. Takeda A, Kodama Y, Ishiwatari S, Okada S. Manganese transport in the neural circuit of rat CNS. Brain Res Bull 1998;45(2):149-152.
20. Thuen M, Singstad TE, Pedersen TB, et al. Manganese-enhanced MRI of the optic visual pathway and optic nerve injury in adult rats. J Magn Reson Imaging 2005;22(4):492-500.
21. Thuen M, Berry M, Pedersen TB, et al. Manganese-enhanced MRI of the rat visual pathway: acute neural toxicity, contrast enhancement, axon resolution, axonal transport, and clearance of Mn(2+). J Magn Reson Imaging 2008;28(4):855-865.
22. Nelder JA, Mead R. A Simplex Method for Function Minimization The Computer Journal 1965;7(4):308-313.
23. Ugarte G, Perez F, Latorre R. How do calcium channels transport calcium ions? Biol Res 1998;31(1):17-32.

NeuroImage 45 (2009) 880–890

Contents lists available at ScienceDirect

NeuroImage

journal homepage: www.elsevier.com/locate/ynimg

Manganese-enhanced magnetic resonance imaging of hypoxic–ischemic brain injury in the neonatal rat

Marius Widerøe [a,*], Øystein Olsen [b], Tina Bugge Pedersen [c], Pål Erik Goa [c,d], Annemieke Kavelaars [e], Cobi Heijnen [e], Jon Skranes [a,f], Ann-Mari Brubakk [a,f], Christian Brekken [c]

[a] Department of Laboratory Medicine, Children's and Women's Health, Norwegian University of Science and Technology, Trondheim, Norway
[b] Department of Radiography, Sør-Trøndelag University College, Trondheim, Norway
[c] Department of Circulation and Medical Imaging, Norwegian University of Science and Technology, Trondheim, Norway
[d] Department of Radiology, St Olavs Hospital, Trondheim, Norway
[e] Department of Psychoneuroimmunology, University Medical Center Utrecht, Utrecht, The Netherlands
[f] Department of Pediatrics, St Olavs Hospital, Trondheim, Norway

ARTICLE INFO

Article history:
Received 24 June 2008
Revised 2 December 2008
Accepted 3 December 2008
Available online 24 December 2008

ABSTRACT

Hypoxic–ischemic injury (HI) to the neonatal brain results in delayed neuronal death with accompanying inflammation for days after the initial insult. The aim of this study was to depict delayed neuronal death after HI using Manganese-enhanced MRI (MEMRI) and to evaluate the specificity of MEMRI in detection of cells related to injury by comparison with histology and immunohistochemistry. 7-day-old Wistar rat pups were subjected to HI (occlusion of right carotid artery and 8% O_2 for 75 min). 16 HI (HI+Mn) and 6 sham operated (Sham+Mn) pups were injected with $MnCl_2$ (100 mM, 40 mg/kg) and 10 HI-pups (HI+Vehicle) received NaCl i.p. 6 h after HI. 3D T_1-weighted images (FLASH) and 2D T_2-maps (MSME) were acquired at 7 T 1, 3 and 7 days after HI. Pups were sacrificed after MR-scanning and brain slices were cut and stained for CD68, GFAP, MAP-2, Caspase-3 and Fluorojade B. No increased manganese-enhancement (ME) was detectable in the injured hemisphere on day 1 or 3 when immunohistochemistry showed massive ongoing neuronal death. 7 days after HI, increased ME was seen on T_1-w images in parts of the injured cortex, hippocampus and thalamus among HI+Mn pups, but not among HI+Vehicle or Sham+Mn pups. Comparison with immunohistochemistry showed delayed neuronal death and inflammation in these areas with late ME. Areas with increased ME corresponded best with areas with high concentrations of activated microglia. Thus, late manganese-enhancement seems to be related to accumulation of manganese in activated microglia in areas of neuronal death rather than depicting neuronal death per se.

Introduction

Hypoxic–ischemic brain injury in the perinatal period results in high mortality and morbidity among infants and children (Ferriero, 2004; Vannucci and Perlman, 1997; Vannucci and Hagberg, 2004). In contrast to adult stroke, hypoxia–ischemia in the neonatal brain results in a prolonged evolution of injury with neurons dying days and weeks after the primary insult. This has presented a possible window of opportunity for therapeutic intervention (Nakajima et al., 2000; Geddes et al., 2001; Vannucci and Hagberg, 2004; Northington et al., 2005), but in order to develop effective treatment strategies the complexity of the underlying injury mechanisms and evolution of injury has to be further investigated. One of the injury mechanisms that we are just beginning to elucidate the consequences and significance of is the inflammatory response after hypoxia–ischemia in the neonatal brain. Inflammatory cytokines have been shown to potentiate excitotoxic injury, and microglia, the resident macrophage of CNS, has been shown to be activated both acutely and delayed in the brain after hypoxia–ischemia. Although microglia by many means are considered a renovation cell through its phagocytosis of dead cells and debris, it is increasingly viewed as a possible cause of cell death through its release of glutamate, free radicals and nitric oxide (McRae et al., 1995; McLean and Ferriero, 2004; Ferriero, 2004).

The advances during the past decade in revealing the pathogenesis of neonatal hypoxic–ischemic brain injury are in part due to new neuroimaging techniques and a focus on mapping the cellular and molecular mechanisms of injury through animal models (Ferriero, 2004; Vannucci and Vannucci, 2005). Combining the strengths of MRI with neonatal animal models give the opportunity of longitudinal studies of brain injury *in vivo* where mechanisms of the evolution of injury can be investigated on a structural and cellular level. One novel versatile MRI technique is manganese-enhanced MRI (MEMRI). Manganese (Mn^{2+}) gives positive contrast on T_1-weighted images due to its paramagnetic properties that primarily shortens T_1 in solid

* Corresponding author. Medical Faculty, LBK, NTNU, MTFS, 7489 Trondheim, Norway. Fax: +47 73 55 13 50.
E-mail address: marius.wideroe@ntnu.no (M. Widerøe).

1053-8119/$ – see front matter © 2008 Elsevier Inc. All rights reserved.
doi:10.1016/j.neuroimage.2008.12.007

tissue (Koretsky and Silva, 2004; Silva et al., 2004). The divalent manganese ion (Mn^{2+}) functions as an analogue for Ca^{2+} in biological systems and is known to enter neurons and glial cells through voltage-gated Ca^{2+}-channels. During normal homeostasis systemic administration of Mn^{2+} gives signal enhancement on T_1-weighted images of brain areas with high neuronal activity (Watanabe et al., 2002; Wadghiri et al., 2004; Kuo et al., 2005). Under pathological conditions the properties of Mn^{2+} give MEMRI other potentials for use. Calcium plays an important role in neuronal death during brain ischemia either through rapid Ca^{2+}-influx as a result of depolarisation caused by energy failure or excitatory glutamate release or as a result of slow continued accumulation of intracellular Ca^{2+} associated with neuronal apoptosis (Ankarcrona et al., 1995; Kristián and Siesjö, 1998; Won et al., 2002; Aoki et al., 2003; Koretsky and Silva, 2004). Substituting Ca^{2+} with Mn^{2+} may lead to intracellular accumulation of Mn^{2+} in neurons undergoing cell death. Aoki et al. has demonstrated this during *early* neuronal death in the adult rat stroke model (Aoki et al., 2003, 2004). However, using the same principles we hypothesised that MEMRI may be utilised for imaging *delayed* neuronal death which would be particularly valuable for better understanding neonatal hypoxic–ischemic brain injury.

The main aim of the present study was to depict delayed neuronal death by MEMRI up to several days after the initial hypoxic–ischemic insult in the neonatal rat brain. In addition, we aimed to evaluate the specificity of MEMRI in detection of cells related to injury by comparison with histology and immunohistochemistry.

Materials and methods

Animals

Wistar rats (Scanbur, Norway AS) were bred in the animal facilities at the St. Olav University Hospital in Trondheim. Time-mated rats ($n=5$) and their offspring ($n=35$) were kept on a 12:12 h light:dark cycle. They had water and food ad libitum. Animal experiments where conducted in accordance with Guidelines set by the Norwegian Ethics Committee for Animal Research and the experiments were approved by the responsible governmental authority.

Hypoxia-ischemia (HI)

The Vannucci–Rice model for hypoxic–ischemic brain damage was used (Rice et al., 1981; Vannucci and Vannucci, 2005): P7 rats (mean weight: 15.1 ± 1.6 g) were anaesthetized with isoflurane (Baxter Medication Delivery, Oslo, Norway) (4% induction, 2% maintenance) in O_2. Through a mid-neck incision, the right common carotid artery was identified, thermo-cauterized and severed. Wounds were closed and sprayed with Xylocaine (2%). Duration of operating procedure was 5–10 min. The pups were then placed back with their dam for recovery and feeding for minimum 2 and maximum 4 h. Thereafter, pups were put in a fibreglass box inside an incubator. The temperature inside the box was kept at 36 ± 0.5 °C throughout the procedure. The box was flushed with pre-heated humified air with 8% O_2 (in 92% N_2) (15 l/min) for approximately 3 min until the oxygen concentration in the box was 8%. Thereafter air flow was kept at 5 l/min and O_2 was measured to 8% throughout the procedure using an OxyQuant S® (EnviteC GmbH, Wismar, Germany). After 75 min of hypoxia, the box was flushed with room air and the pups were allowed to recover for 5 min before being placed back with their dam. This procedure resulted in a unilateral hypoxic–ischemic insult (HI) to the right cerebral hemisphere. In every litter pups were sham-operated; carotid artery was identified under anaesthesia, but not damaged. Sham-operated animals were not subjected to hypoxia.

Study groups and manganese administration

Six hours after the hypoxia one group of HI pups (HI + Mn) ($n=16$) and the sham operated pups (Sham + Mn) ($n=6$) were given a single dose of $MnCl_2$ (# 7773-01-5, Sigma-Aldrich Inc., St. Louis, USA) intraperitoneally. A dose of 40 mg $MnCl_2$ per kg bodyweight (~318 μmol Mn^{2+}/kg) at a concentration of 100 mM was mixed with 0.9% NaCl to make an isotonic injection volume of 0.1 ml. Another group of pups (HI + Vehicle) ($n=10$) did not receive $MnCl_2$, but were instead injected with 0.1 ml of 0.9% NaCl to serve as controls (Fig. 1).

To evaluate whether there was active cellular uptake of manganese 7 days after hypoxia–ischemia (HI), one group of pups HI + Mn6 ($n=3$) followed the described protocol for hypoxia–ischemia on day 0, but received no injections until day 6 after HI. They were then injected with 40 mg $MnCl_2$ per kg at 100 mM mixed with 0.9% NaCl (total volume 0.1 ml).

Magnetic resonance imaging

MRI was performed on days 1, 3 and 7 after HI (day 0) using a 7 T magnet (Biospec 70/20 AS, Bruker Biospin MRI, Ettlingen, Germany) with water-cooled (BGA-12, 400 mT/m) gradients. A 72 mm volume resonator was used for RF transmission and an actively decoupled mouse head surface coil was used for RF reception. Pups injected with $MnCl_2$ on day 6 (HI + Mn6) were also imaged on days 8, 10 and 14 after HI. All animals were imaged longitudinally at all time-points until they were sacrificed for histology. During scanning the anaesthetized (2% isoflurane in 30% O_2, 70% N_2) pups lay prone in a dedicated water heated mouse bed (Bruker Biospin MRI) and the head of every animal was fixed in the same position with inbuilt earplugs, tooth bar and nose-mask. This assured the same placement of the head of the animals within the magnet from scan to scan.

After a gradient echo FLASH pilot scan (acquisition time 1 min), a 3D data set was obtained using a T_1-weighted gradient echo FLASH sequence with flip-angle = 30°, TR = 12 ms, TE = 3.0 ms. FOV = 20 × 20 × 17.5 mm and acquisition matrix was 128 × 96 × 84

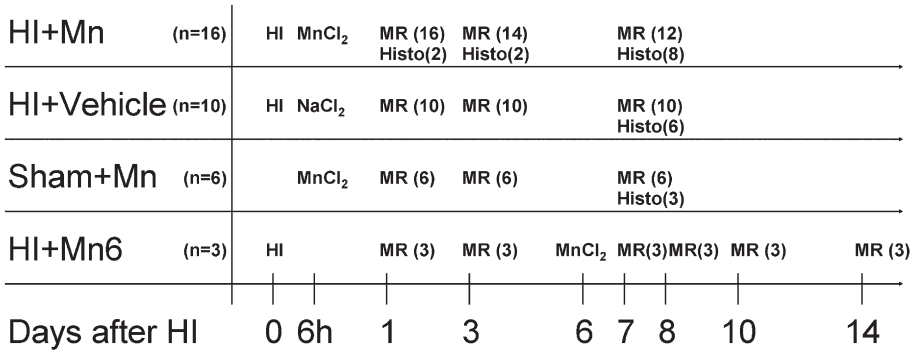

Fig. 1. Overview of the study design with study groups (HI + Mn, HI + Vehicle, Sham + Mn and HI + Mn6). Timing of hypoxia–ischemia (HI) and injection with $MnCl_2$ or Vehicle ($NaCl_2$), and timing of MR imaging (MR) and sacrificing for histological examinations (Histo).

giving an acquired resolution of 156 μm×208 μm×208 μm. With zero-filling of the matrix to 128×128×112, the interpolated resolution was 156 μm isotropic. Acquisition time was 25 min with 16 averages. 2D T_2-maps were obtained with a spin-echo sequence (MSME) with TR=2500 ms, TE=7.6 ms, 40 echoes, slice thickness 1 mm. FOV=18×18 mm and acquisition matrix 128×96 giving an in plane resolution of 140 μm×187 μm. With zero-filling of the matrix to 128×128 the interpolated resolution was 140 μm isotropic. Acquisition time was 16 min with 4 averages. The receiver gain was held constant for all scans and the signal scaling during reconstruction of the images was corrected for before quantitative analysis of the data.

The B1-field of the volume-coil was considered homogeneous within the field of view, while the spatially inhomogeneous sensitivity of the surface-coil used in the 3D T_1-weighted FLASH acquisition was corrected for using two additional scans in coupled and single coil operation: 3D T_1-weighted FLASH sequences: Flip-angle=30°, TR=12 ms, TE=3.0 ms, matrix size 32×32×32, acquisition-time was 2 min for each scan. FOVs were the same as those used to obtain 3D data set. The correction-procedure was performed in Matlab (MATLAB ver 2007a, MathWorks Inc.). The MRI signal intensity in a voxel at location *(x,y,z)* was normalized using the following relation:

$$I_{SC}(x,y,z) = I_{CC}(x,y,z)\frac{C_{SC}(x,y,z)}{C_{CC}(x,y,z)} \quad (1)$$

where C_{CC} and C_{SC} is the coupled-coil and single-coil intensities in the correction scan datasets respectively, I_{CC} is the recorded couple-coil signal intensity in the main 3D data set, and I_{SC} is the resulting normalized signal intensity.

Histology and immunohistochemistry

Animals were sacrificed after MRI acquisition on day 1 (HI+Mn, n=2), day 3 (HI+Mn, n=2) and day 7 (HI+Mn, n=8; HI+Vehicle, n=6; HI+Sham, n=3) following HI. They received an overdose pentobarbital (300 mg/kg) and were perfused intracardially with 4% paraformaldehyde (PAH) in phosphate-buffered saline (PBS). Brains were removed and embedded in paraffin. Coronal sections (8 μm) corresponding to −3.25 mm from the bregma (Paxinos and Watson, 1998) were cut and stained with either hematoxylin–eosin (Klinipath, Duiven, the Netherlands), anti-MAP2 (Sigma-Aldrich, Steinheim, Germany), anti-cleaved-caspase3 (Cell Signaling) or anti-ED1-fitc (Serotec, Raleigh, NC) and slices from HI+Mn pups on days 1 and 3 and 4 HI+Mn pups on day 7 were stained with anti-GFAP (Cymbus Biotechnology, Southampton, UK). Sections were then incubated with rat-anti-FITC-biotin (Roche, Basel, Switzerland), goat-anti-rabbit-biotin (Vector Laboratories, Burlingame, CA) or horse-anti-mouse-biotin (Vector Laboratories, Burlingame, CA). Visualization was performed using a Vectastain ABC kit (Vector Laboratories). Full section images were captured with a Nikon D1 digital camera (Nikon, Tokyo, Japan). Sections were also stained with Flourojade B (Chemicon International, Temecula, CA, USA) after incubation in 0.06% potassium-permanganate, embedded in DEPEX and visualized using a fluorescence-microscope in the FITC channel.

MR image analysis

In-house developed software was used for MR image analysis (MATLAB ver. R2007a, MathWorks Inc., Natick MA, USA). From the 3D T_1-weighted data set a coronal 2D image-slice (slice thickness 0.156 mm) approximately corresponding to the histological slice was extracted by tri-linear interpolation and used for image analysis. Using a rat brain atlas (Paxinos and Watson, 1998) for reference, regions of interest (ROI) were manually placed in the cortex, hippocampus, External capsule and thalamus in both hemispheres and mean signal intensity (SI) was calculated for each ROI.

To evaluate Manganese enhancement (ME), SI on T_1-weighted images in ROIs in the injured hemisphere (ipsilateral) was compared to the contralateral (unaffected) hemisphere. To allow comparison between animals and groups of animals, a measure of the relative contrast (RC) was calculated for each structure (cortex, hippocampus, external capsule and thalamus) in every animal using the 2D-image slices acquired on days 1, 3 and 7. RC was calculated using the following equation:

$$RC = \frac{SI_{\mathrm{ROI}_{\mathrm{Ipsilateral}}} - SI_{\mathrm{ROI}_{\mathrm{Contralateral}}}}{SI_{\mathrm{ROI}_{\mathrm{Ipsilateral}}} + SI_{\mathrm{ROI}_{\mathrm{Contralateral}}}}. \quad (2)$$

Comparison of histology and manganese enhancement

The histological slices with different staining were evaluated using standard and fluorescent microscopy. The extent and intensity of CD68 and GFAP staining and the number of stained cells in different areas of the injured hemisphere were compared to the extent and intensity of ME. The extent of MAP-2 loss was compared to the extent of ME. For this comparison 2D T_1-weighted images was viewed with a RGB lookup table where the threshold for the colour yellow was adjusted to right above the highest level of signal intensity recorded in the contralateral hemisphere for every animal. High signal areas in the injured hemisphere, indicating increased ME, would hence appear yellow.

The following computer-based method for evaluating agreement between increased ME on T_1-weighted images and histological staining was developed: manganese-enhancement in the injured hemisphere was defined by signal intensities above a threshold set by mean SI of a ROI placed in the thalamus of the contralateral hemisphere +1 SD of the image noise. A binary mask was created for the area of ME in the injured hemisphere. Images of whole histological slices stained for MAP-2, CD68 and GFAP were segmented in the RGB vector space using the Mahalanobis distance from an average colour calculated from a ROI manually placed in an area with uniform staining (Gonzalez et al., 2004). The segmented colours were defined to be in a distance equal or less than 1 SD from the average colour, where the SD was selected from the RGB component with the largest variance within the ROI. From this a binary mask for the area of staining was created. The T_1 weighted MR images and the histology images were then co-registered using landmark based image registration. After manually selecting approximately 15 pairs of anatomical points of reference in the two images, the transformation was calculated using a piecewise linear model. The transformation was applied to the segmented histology image which made us able to compare the manganese-enhanced areas and segmented histology staining on a pixel-to-pixel basis. The fit of the transformation was evaluated visually. The overlap between the area of histological staining ($Area_{Histology}$) and the segmented manganese-enhanced area ($Area_{ME}$) was evaluated using three different parameters, where the intersection of the areas of ME and histological staining was divided by either the union of the two areas, area of histological staining or the area of segmented ME:

$$Match = \frac{Area_{\mathrm{ME}} \cap Area_{\mathrm{Histology}}}{Area_{\mathrm{ME}} \cup Area_{\mathrm{Histology}}} \quad (3)$$

$$Sensitivity = \frac{Area_{\mathrm{ME}} \cap Area_{\mathrm{Histology}}}{Area_{\mathrm{Histology}}} \quad (4)$$

$$Prediction = \frac{Area_{\mathrm{ME}} \cap Area_{\mathrm{Histology}}}{Area_{\mathrm{ME}}}. \quad (5)$$

Statistics

SPSS version 14.0 (SPSS Inc., Chicago, IL, USA) was used for all statistical analysis and the level of significance was set to 0.05. Signal intensity data and relative contrast data are presented in figures as mean with error-bars representing±2 SEM. Mann–Whitney *U*-test was used to compare the mean signal intensities in ROIs and the mean relative contrast (RC) in different structures between groups. T_2-values are presented as mean±1 SD. Paired *t*-tests were used to analyze differences in T_2-values of the ROIs between the two hemispheres. Results from the pixel-wise comparison of T_1-weighted images with histology and T_2-maps are presented as mean±SEM.

Results

MR signal enhancement with manganese

T_1-weighted MR images of HI pups injected with $MnCl_2$ (HI+Mn) showed high signal intensities in large parts of the dorsolateral thalamus and in several animals also in parts of the hippocampus and remaining cortex on day 7 (Fig. 2). In a few HI+Mn pups some small spots were also seen in the thalamus on day 3, but no high signal intensities was seen in the injured hemisphere among HI+Mn pups prior to day 3. High signal changes were not seen in HI+Vehicle pups in the injured hemisphere on day 3 or day 7 (Fig. 2).

ROI analysis of the injured hemisphere showed higher signal intensities in cortex, hippocampus and external capsule among HI+Mn than HI+Vehicle pups on day 1. On days 3 and 7 signal intensities of ROIs in cortex, hippocampus and thalamus were higher among HI+Mn than HI+Vehicle pups (Fig. 3). Also, on day 7 signal intensity of ROIs in the injured hemisphere's cortex and thalamus of HI+Mn pups was significantly higher than among Sham+Mn pups (Fig. 3).

Signal intensities in ROI in the contralateral hemisphere of HI+Mn pups were similar to Sham+Mn at all times in all areas (data not shown).

Contrast enhancement on T_1-weighted MR images caused by manganese on day 7

In order to identify areas of high or low signal intensities in the injured hemisphere relative to the contralateral hemisphere and compare these between animals, a normalized relative contrast (RC) was calculated (see Materials and methods). In the dorsolateral thalamus of the HI+Mn pups there was a mean negative RC on day 1 that increased to a highly positive RC (SI injured hemisphere>SI contralateral hemisphere) on day 7. In cortex and hippocampus the same trend was seen with RC increasing from negative (injured<contralateral) on day 3 to around zero (injured=contralateral) on day 7. However, among HI+Vehicle pups the opposite trend was observed going from positive RC in all areas on day 1 to negative on day 3 and becoming more negative from day 3 till 7 (Fig. 4). This lead to a large difference between HI+Mn and HI+Vehicle pups with far more positive RC in cortex, hippocampus and thalamus among HI+Mn than HI+Vehicle pups on day 7 (Fig. 4).

Increased manganese-enhancement after injection on day 6

T_1-weighted MR images of animals injected with $MnCl_2$ on day 6 (HI+Mn6) were also obtained on days 7, 8, 10 and 14 after HI. On day 7, increased signal intensities were seen primarily in the borders surrounding the area of the dorsolateral thalamus of the injured hemisphere (Fig. 5). The area corresponded to that seen on day 7 in pups injected with $MnCl_2$ 6 h after HI. A ROI placed in this area showed significantly higher mean signal intensities on day 7 among HI+Mn6 pups than among HI+Vehicle pups. From day 7 till day 14 the contrast in this area increased with more uniformly high signal intensity in the centre of the area evolving during the week (Fig. 5). However, signal intensity of this ROI among HI+Mn6 pups never became as high as the equivalent ROI among HI+Mn pups on day 7 (i.e. one week after their $MnCl_2$ injection). Among HI+Mn6 pups RC was negative in thalamus and hippocampus on day 7, but steadily increased in both areas and became positive on day 14.

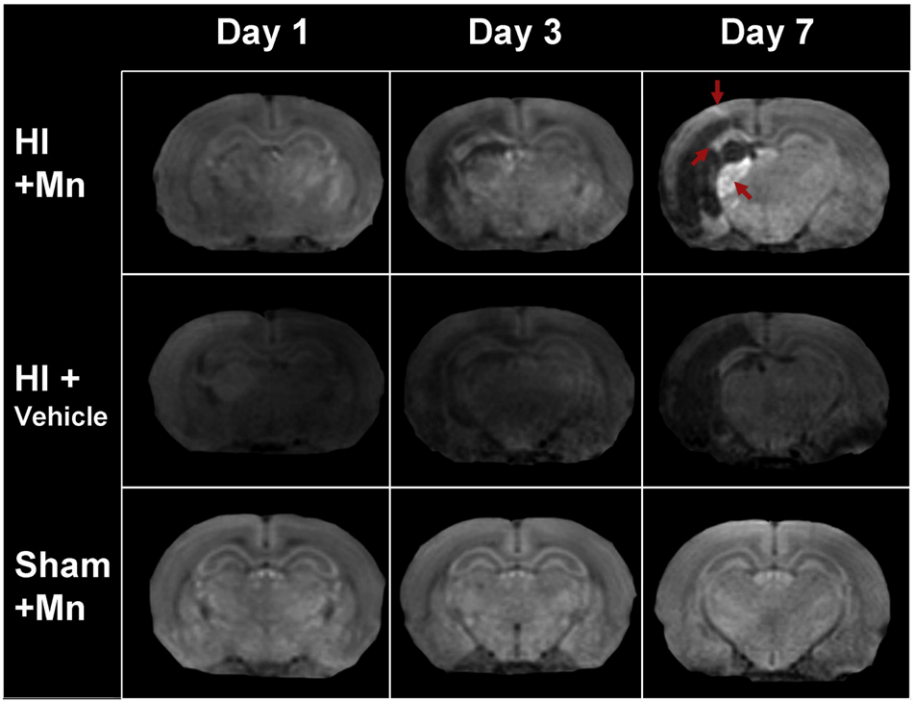

Fig. 2. T_1-weighted images of evolution of brain injury from day 1 till day 7 after hypoxia–ischemia in different groups. On day 7 high signal intensity is observed in the dorsolateral thalamus, and parts of the remaining cortex and hippocampus of the injured hemisphere of HI pups with injected $MnCl_2$ (arrows). These changes were not observed in HI+Vehicle or Sham+Mn pups.

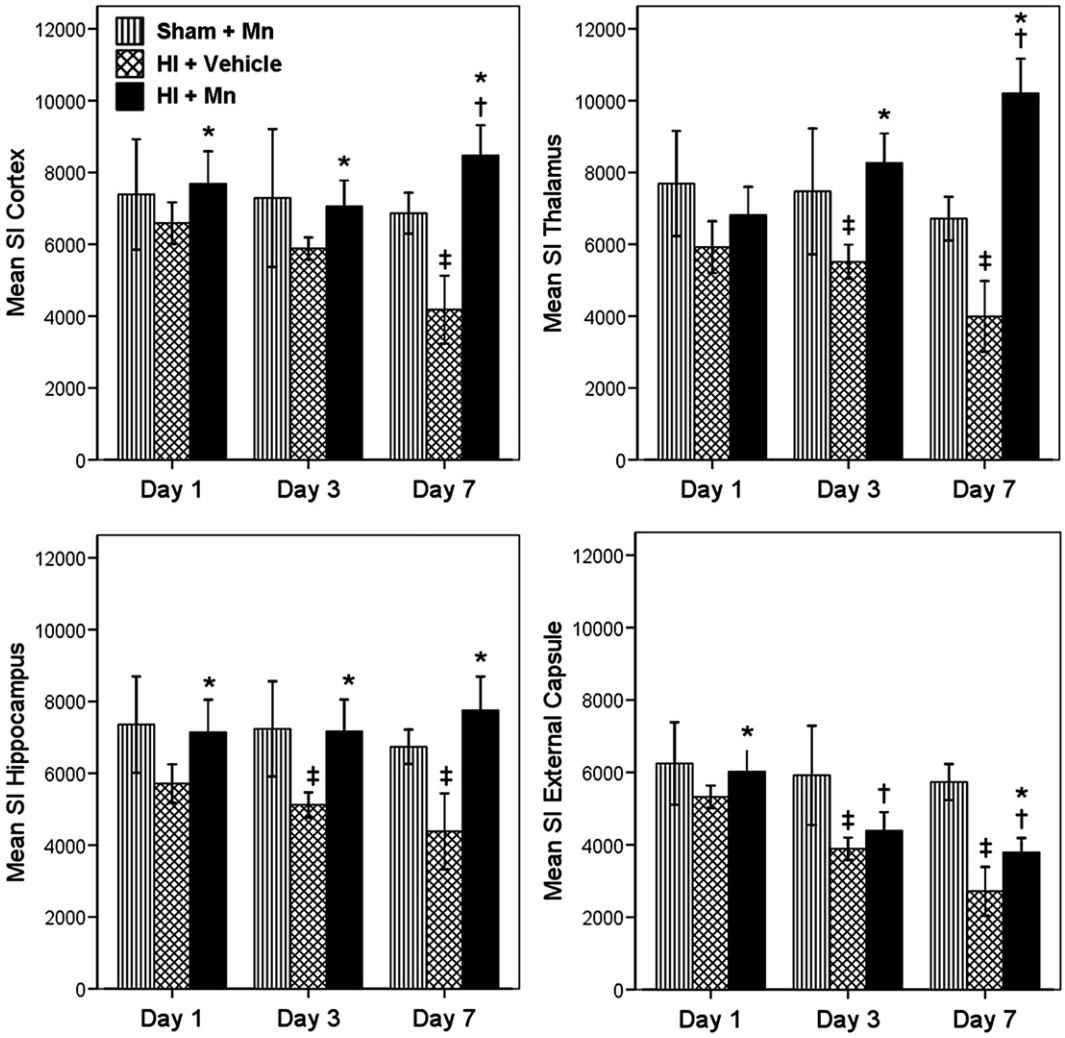

Fig. 3. Mean signal intensity (SI) in ROIs in cortex, thalamus, hippocampus and external capsule of the injured/ipsilateral hemisphere of Sham+Mn, HI+Vehicle and HI+Mn pups at different scan times. The graph shows how the mean SI of ROIs in cortex, hippocampus and thalamus increased over time among HI+Mn pups, with the most noticeable increase in thalamus, whereas among HI+Vehicle the SI steadily decreased in all areas. On day 1 SI among HI+Mn was on the same level as in Sham+Mn, but it was higher than among HI+Vehicles (thalamus $p=0.93$), indicating presence of manganese in these areas. SI in cortex and thalamus were significantly higher than both Sham+Mn and HI+Vehicle pups on day 7, indicating a pathological presence of manganese. SI in the external capsule ROI showed the same trend among HI+Mn and HI+Vehicle with decreasing values from day 1 till day 7. However, SI in this area was still higher among HI+Mn pups than HI+Vehicle on day 1 and 7. *$p<0.05$ HI+Mn vs. HI+Vehicle, †$p<0.05$ HI+Mn vs. Sham, ‡$p<0.05$ HI+Vehicle vs. Sham. (Error bars±2 SEM).

T_2-mapping

HI+Mn vs HI+Vehicles

At all scans times; the mean T_2 values measured in cortex, hippocampus and thalamus were significantly lower in HI+Mn than in HI+Vehicle pups. Among HI+Mn and HI+Vehicle pups mean T_2 values were elevated in cortex, hippocampus and thalamus in the injured hemisphere compared to the contralateral hemisphere on day 1. In HI+Vehicle, T_2 values in cortex and hippocampus of the injured hemisphere remained elevated, however slightly reduced from day 1 till day 3. T_2 in the same areas among HI+Mn pups were gradually reduced from day 1 till day 7 and was on the same level as in the contralateral hemisphere. In the dorsolateral thalamus, mean T_2 values were gradually reduced from day 1 till day 7 in both groups with the largest reduction among the HI+Mn pups. The mean T_2 value in dorsolateral thalamus of the injured hemisphere on day 7 was 24.5 ms±8.3 among HI+Mn pups vs. 54.3 ms±4.5 among HI+Vehicles ($p=0.001$) (Fig. 6). In the contralateral thalamus there were also a tendency to lower mean T_2 values among HI+Mn than HI+Vehicle pups (mean 48.6 ms±14.8 vs. mean 61.3 ms±6.9; $p=0.064$). The differences in T_2 values in thalamus between the injured and the contralateral hemisphere on day 7 were significant for both groups.

HI+Mn vs Sham+Mn

On day 1 there were increased mean T_2 values in cortex, hippocampus and thalamus of the injured hemisphere among HI+Mn pups compared to Sham+Mn. On days 3 and 7, mean T_2 values in these areas were reduced, resulting in significantly lower mean T_2 values in dorsolateral thalamus among HI+Mn pups than among Sham+Mn on day 7.

T2-mapping and manganese-enhancement

The area with reduced T_2 in dorsolateral thalamus of the injured hemisphere on day 7 in HI+Mn pups co-localized well with the manganese-enhanced areas on T_1-w images on visual analysis (Fig. 6). Software-based pixel-wise comparison of the overlap between the two segmented areas gave a mean match of 0.53±0.06, with a mean probability of 0.69±0.08 for a manganese-enhanced pixel to have a corresponding pixel with T_2-reduction.

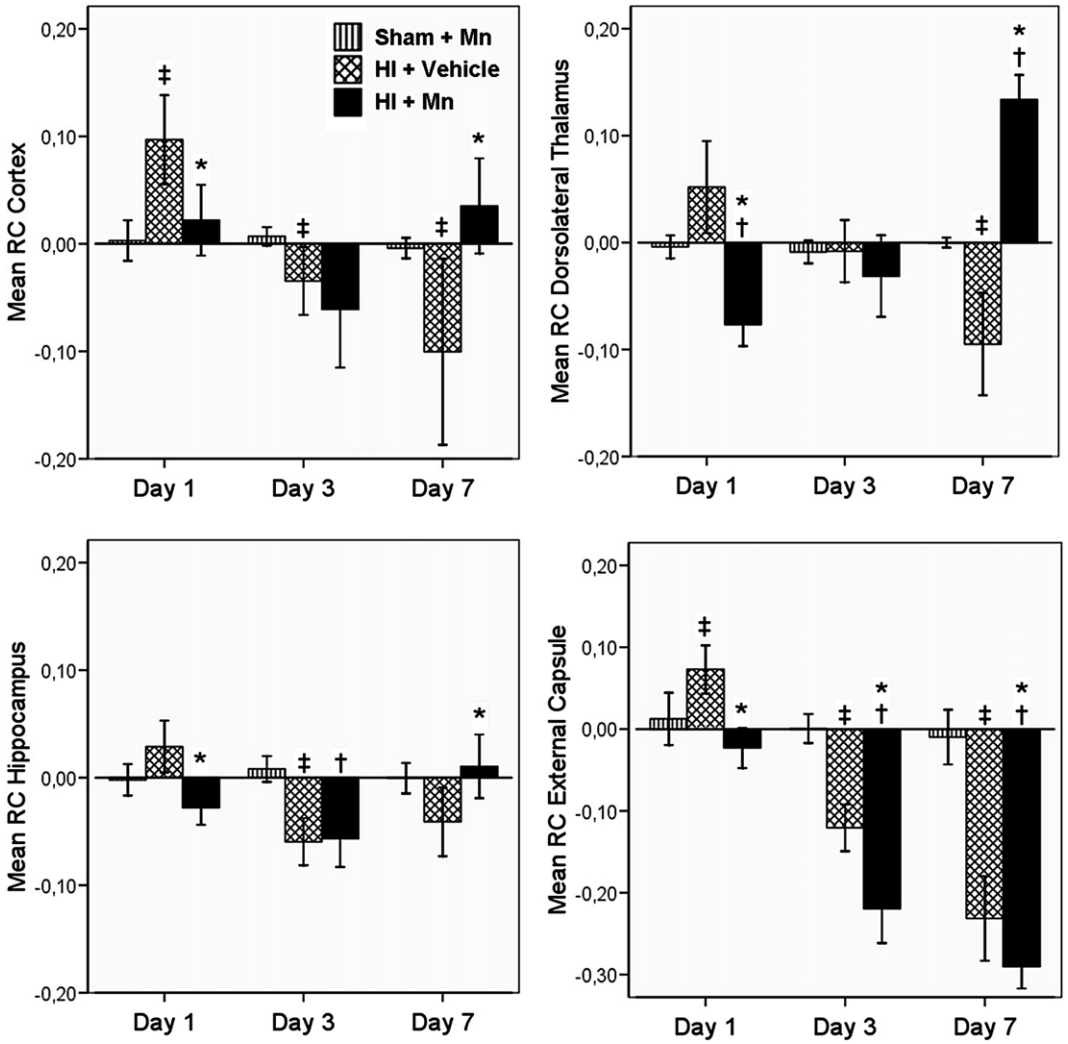

Fig. 4. Mean Relative Contrast (RC) in ROIs in cortex, thalamus, hippocampus and external capsule of Sham+Mn, HI+Vehicle and HI+Mn at different scan times. There was a highly positive relative contrast in thalamus among HI+Mn pups on day 7, meaning higher signal intensity in the injured- than the contralateral hemisphere. Notice the difference in development of RC between HI+Mn pups and HI+Vehicle in cortex, hippocampus and thalamus over time, with decreasing levels of RC among HI+Vehicle, whereas HI+Mn pups showed increasing RC from day 3 till 7. RC was significantly more positive in these areas on day 7 among HI+Mn than HI+Vehicle. External capsule showed the same development among both HI groups. *$p<0.05$ HI+Mn vs. HI+Vehicle, $^{\dagger}p<0.05$ HI+Mn vs. Sham, $^{\ddagger}p<0.05$ HI+Vehicle vs. Sham. (Error bars±2SEM).

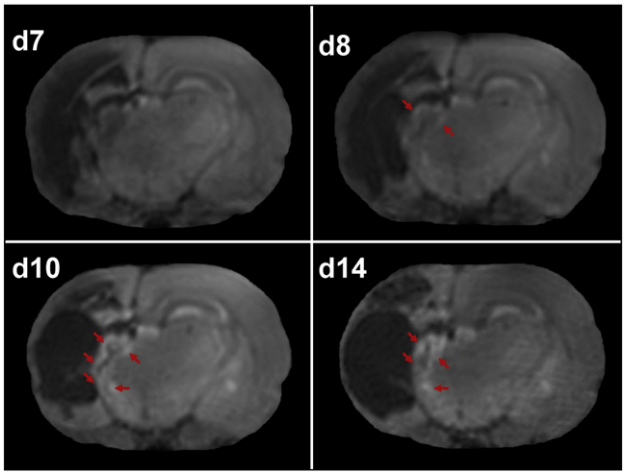

Fig. 5. T_1-weighted images 7, 8, 10 and 14 days after HI in rat pup injected with $MnCl_2$ day 6 after HI. Increasing signal intensity from day 7 till day 14 can be seen in an area of thalamus in the ipsilateral hemisphere (arrows).

Histology and immunohistochemistry

Day 1

On day 1 there was neuronal loss (areas not stained for MAP-2) in large parts of cortex, hippocampus and thalamus in the injured hemisphere with accompanying high number of cleaved caspase 3 positive cells in cortex and hippocampus and some in thalamus. Reactive astrocytes (staining positively for GFAP) and a few activated microglial cells (CD68 positive cells) were seen in widespread areas of the injured hemisphere.

Day 3

Histology on day 3 showed the same pattern of neuronal loss and cleaved caspase 3 positive cells as on day 1. Reactive astrocytes with intense GFAP staining were seen in all injured areas. Activated microglia/macrophages were evenly spread out in cortex, hippocampus and thalamus.

Day 7

Histological examination of brain sections showed no difference in lesion size, morphology, or immunohistochemical staining between HI+Mn and HI+Vehicle pups. The contralateral

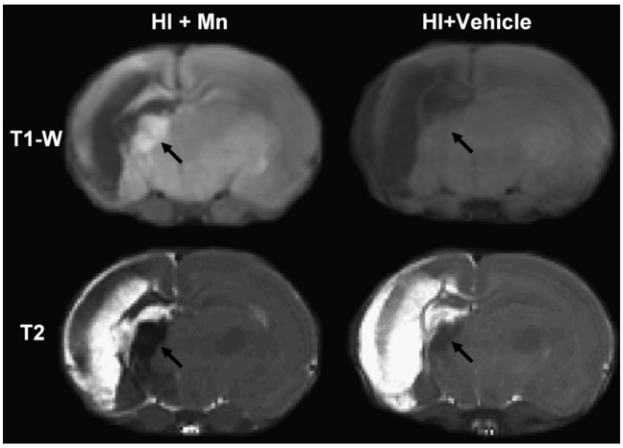

Fig. 6. T_1-weighted images and T_2-maps 7 days after HI of pups with and without injected $MnCl_2$. An area with highly reduced T_2 is seen in the dorsolateral thalamus of HI+Mn pups, corresponding to the manganese-enhancement on T_1-weighted image (arrows). In HI+Vehicle a smaller reduction in T_2 is observed in the same area, but with no corresponding increased signal intensity on T_1-weighted images (arrows).

hemisphere in these groups and among Sham+Mn pups showed no injury or abnormal pattern of staining. Immunohistochemical examination of the injured hemisphere in HI pups on day 7 showed widespread loss of tissue and cyst formation in the cortex and external capsule of the injured hemisphere. In the remaining tissue, neuronal loss was prominent and there were high numbers of Flourojade B positive dying neurons in cortex, hippocampus and dorsolateral thalamus in all HI animals (Fig. 7). Active caspase 3 positive cells were also present in all these areas, but in low numbers. Activated microglia/macrophages with intense CD68 staining were numerous in all these areas with the highest concentration in the dorsolateral thalamus. Numerous reactive astrocytes with intense GFAP staining were seen in large parts of the injured hemisphere with the highest concentration in hippocampus, cortex and dorsolateral thalamus.

Histology and manganese-enhancement on day 7

Areas with activated microglia (CD68 positive cells) had the best agreement with the areas of increased ME on T_1-weighted imaging. In 7 out of 8 HI+Mn pups increased ME was seen in the same areas that had high numbers of CD68 positive cells and vice versa. Also, the areas with activated microglia/macrophages and the areas of increased ME showed a similar morphological appearance, especially in the dorsolateral thalamus (Fig. 7). Furthermore, in two animals (HI+Mn) with very low density of activated microglia in the thalamus, there was almost no detectable ME on MRI. However, one animal had high density of CD68 positive cells, but little ME.

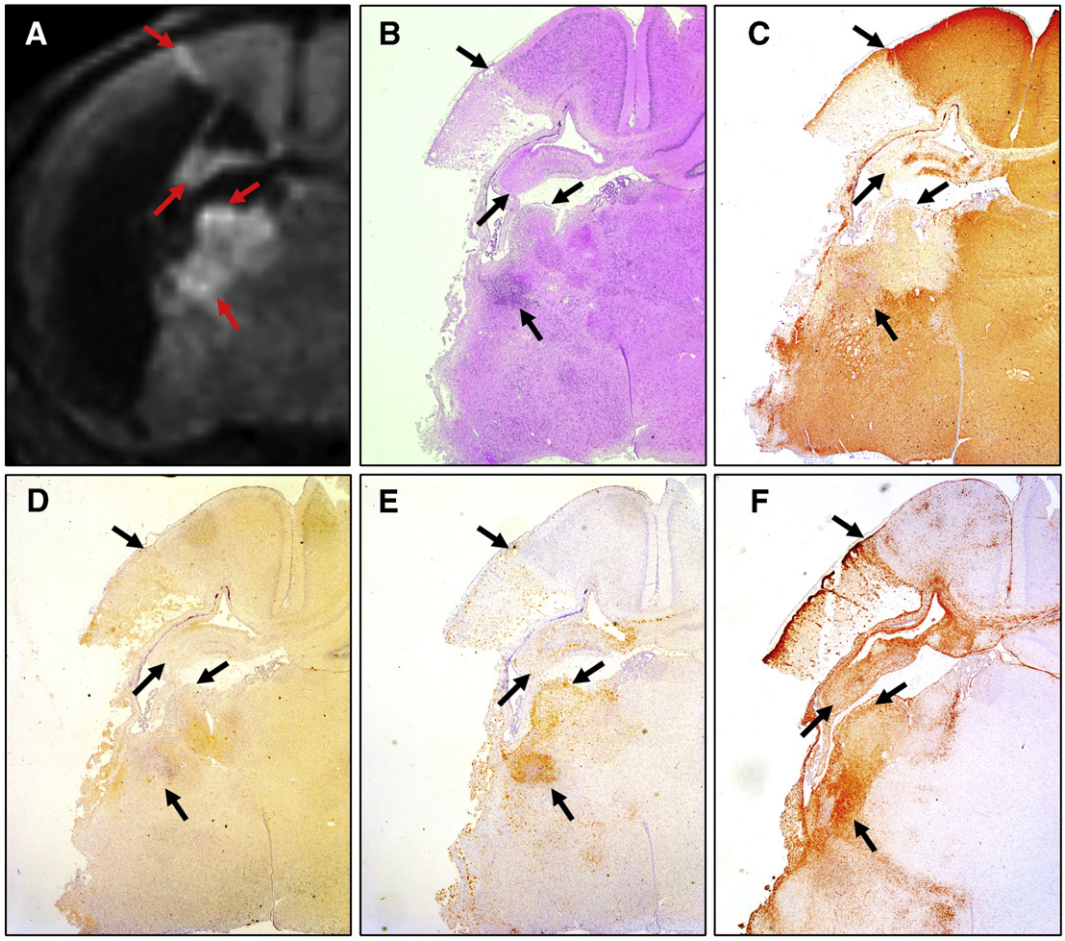

Fig. 7. T_1-weighted image (A) acquired day 7 after HI in pup injected with $MnCl_2$. Corresponding histological slices stained with HE (B) MAP-2 (C), Caspase-3 (D), CD68 (E) and GFAP (F) are shown. Arrows points to areas with increased manganese-enhancement in the T_1-weighted image and corresponding areas on histology. Comparison shows areas with dead neurons (not stained for MAP-2), activated microglia (CD68) and reactive astrocytes (GFAP) in areas with increased manganese-enhancement, but with best morphologic correlation between manganese-enhancement and staining for activated microglia.

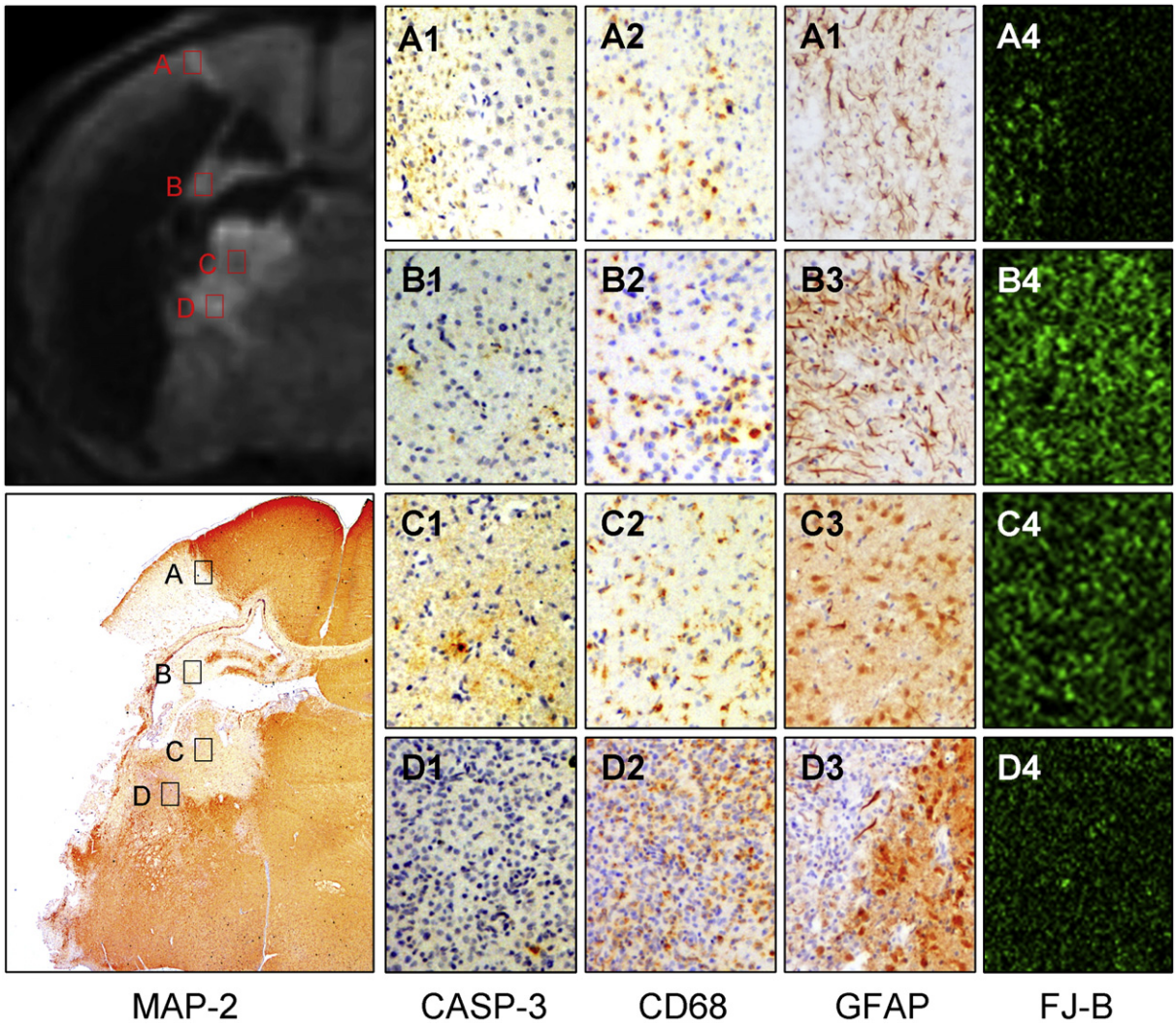

Fig. 8. Immunohistochemical staining with MAP-2, Caspase-3, CD68, GFAP and Flourojade B in different areas of varying intensity on T_1-weighted MR Image acquired day 7 after HI in pup injected with $MnCl_2$. Intensity of increased manganese-enhancement correlates well with staining for reactive astrocytes (GFAP) and activated microglia (CD68) and less with dying neurons (Flourojade B) and marker for apoptosis (Caspase-3).

Neuronal death (MAP-2 loss) and dying neurons (Fluorojade B positive cells) as well as reactive astrocytes (GFAP positive cells) were also found in the areas with increased ME on T_1-weighted images (Fig. 8). The morphological appearance of neuronal loss and the distribution of dying neurons (Fluorojade B positive cells) corresponded well with that of increased ME, but the degree of neuronal loss and density of dying neurons did not always agree well with the signal intensity of ME. The distribution of reactive astrocytes in the injured hemisphere was far more extensive than the detectable increased ME (Fig. 7). Also, the density of GFAP-staining in different areas did not always correspond with the degree of ME.

Areas with GFAP-staining, CD68 staining and MAP-2 loss were segmented and compared to areas of increased ME on a pixel-wise basis. The uncertainty in co-registration of images, made the comparison of ME and immunohistochemical staining in the small areas of cortex and hippocampus unreliable. Results of the comparison in the thalamus on day 7 are presented in Table 1 and suggest that the best match was found between increased ME and CD68 positive areas, in accordance with the results from the visual microscopic analysis.

Table 1
Overlap between manganese-enhancement and immunohistochemical staining

	n	Match	Sensitivity	Prediction
CD68	4	0.34 (±0.16)	0.44 (±0.23)	0.53 (±0.24)
GFAP	4	0.25 (±0.10)	0.27 (±0.12)	0.87 (±0.11)
MAP-2 loss	6	0.28 (±0.08)	0.31 (±0.09)	0.74 (±0.09)

Shows the results of a computer based comparison of immunohistochemical stainings and manganese-enhancement in the thalamus. Match gives the degree of overlap between the areas of manganese-enhancement and histological staining. Sensitivity gives the probability of manganese-enhancement of a pixel, given positive histological staining. Prediction gives the probability of positive staining on histology when a pixel is manganese-enhanced. The relative small area of CD68 positive staining made the predictive value very sensitive to errors in geometric overlap between MRI and histology. (Mean ± S.E.M).

Discussion

In the present study we have shown increased manganese-enhancement (ME) on T_1-weighted images in specific brain areas seven days after hypoxic–ischemic injury in the neonatal rat. High signal intensity on T_1-weighted images as well as reduced T_2-values were seen in the dorsolateral thalamus and parts of hippocampus and the remaining cortex of the injured hemisphere in pups that were injected with $MnCl_2$. Increased ME in these areas co-localized with reactive astrocytes, dying neurons and activated microglia/macrophages on immunohistochemical analysis, with the best spatial agreement with the activated microglia/macrophages.

Increased manganese-enhancement only detectable on day 7

In order to study pathological processes with MEMRI, the pathological ME always has to be compared to the normal physiological enhancement of the brain tissue architecture as shown by several studies (Wadghiri et al., 2004; Kuo et al., 2005; Watanabe et al., 2002; de Sousa et al., 2007). The strength of the current animal model is that only one hemisphere is injured, while the other is considered physiologically normal. In this study we have calculated a relative contrast parameter (RC) as a semi quantitative measure of the relative signal intensity and manganese enhancement in the two hemispheres. This also compensates for any variations in SI between days and animals. Considering the fact that RC was consistent with zero in Sham+Mn pups at all time points, any deviation of RC from zero in the injured animals was most likely due to different tissue characteristics and/or differences in manganese uptake in the two hemispheres and not to any acquisition artefacts or inhomogeneity of the B_1.

In the thalamus of the injured hemisphere, a specific increase in ME was observed on day 7 in the HI+Mn group (positive RC significantly different from shams). In hippocampus and cortex of the injured hemisphere, the positive and significantly higher RC among HI+Mn than among HI+Vehicle on day 7 indicates the presence of manganese in these structures, but is difficult to distinguish from the normal uptake in the uninjured hemisphere, as RC was not significantly different from shams.

The differences in RC between HI+Mn and HI+Vehicle pups on day 1 are interesting. The positive RC among HI+Vehicle pups indicates reduction of T_1 in the injured structures, compared to the uninjured hemisphere, which contradicts a study that showed increased T_1 (Qiao et al., 2004). The increase in T_2 in the same areas is more in accordance with the previous study, but the simultaneous high signal on T_1-weighted images is somewhat puzzling. Increased proton density in the injured hemisphere may be one explanation. Another may be that paramagnetic effects of degraded haemoglobin gives hyperintensity on T_1-weighting, while oedema of the tissue gives a predominantly T_2 increase. However, the exact cause of this finding remains unclear. Furthermore, assuming the same underlying tissue-changes in HI+Mn pups, the consistently lower RC among HI+Mn pups than among HI+Vehicle pups at day 1 can actually be interpreted as a lower Mn^{2+} uptake in the injured hemisphere compared to the uninjured hemisphere among HI+Mn pups at this time-point. Considering this, the temporal trends of RC in cortex, hippocampus and thalamus among HI+Mn pups suggest increasing Mn^{2+} concentrations from day 1 till day 7, which is also in accordance with the trends in signal intensity.

No increased manganese-enhancement at time of maximum neuronal death

Immunohistochemical analysis 1 and 3 days after HI showed widespread cell death and apoptosis in the affected hemisphere, in accordance with results from previous studies that cell death peaks 24–72 h after hypoxia–ischemia (Nakajima et al., 2000; Northington et al., 2001; Vannucci and Vannucci, 2005). The lack of increased ME at time of maximum neuronal death is in contrast with the results by Aoki et al, who found increased ME immediately after ischemia in the adult rat (Aoki et al., 2003, 2004). However, differences in animal model and MEMRI methodology make it difficult to compare the studies. Intra-arterial injection of $MnCl_2$ with disruption of the BBB with mannitol shortly after ischemia in the study by Aoki et al. (2003, 2004) may lead to a much higher availability of Mn^{2+} in the ischemic areas and less unspecific uptake in normal tissue compared to a slow diffusion of Mn^{2+} over the choroid plexus. The intentional distribution of Mn^{2+} to the brain tissue via choroid plexus in our model was confirmed on MRI on day 1 by better contrast of brain tissue architecture and generally higher signal on T_1-weighted images approximately 18 h after IP injection of $MnCl_2$. This is in accordance with previous studies (Wadghiri et al., 2004; Kuo et al., 2005; Watanabe et al., 2002; de Sousa et al., 2007). Some leakage of Mn^{2+} across the immature neonatal blood brain barrier (BBB) could also be expected, and this may have been further potentiated by the effect of hypoxia–ischemia (Takeda, 2003). Although caution must be exercised when comparing signal intensity between animals, even when the physical conditions during scanning are the same, the higher signal intensity on T_1-weighted images in the injured hemisphere on day 1 among HI+Mn pups than among HI+Vehicle pups indicates the presence of some Mn^{2+} in the injured brain tissue among HI+Mn pups. However, any specific Mn^{2+} uptake into dying neurons on day 1 or 3 seems to have been too small to give any significant T_1 contrast compared to normal tissue. One limitation of this study was that we were not able to quantify the concentration of Mn^{2+} in tissue. For future studies, quantification of T_1 could increase the sensitivity and give more clarity to the present concentration of Mn^{2+}in tissue.

Increased manganese-enhancement seven days after hypoxia–ischemia relates to inflammation

A process of delayed neuronal cell death in the dorsolateral thalamus several days after the initial injury has previously been reported by others (Northington et al., 2001, 2005; Vannucci and Hagberg, 2004; Ohno et al., 1994). Consistent with this, histology on day 7 in our study showed high degree of neuronal loss and high concentrations of dying neurons with some apoptotic cells especially in the dorsolateral thalamus, but also in areas of the remaining cortex and hippocampus. The increased ME found in the same areas suggested that increased ME visualized brain tissue with neuronal death. However, the increased ME was far better co-localized with areas with glial cell activation and inflammation than with apoptotic and dying neurons. The best co-localization was with activated microglia/macrophages, which were largely confined to the areas with ME, whereas the reactive astrocytes were found in a larger area than the increased ME. This co-localization and probable relation between activated microglia/macrophages and ME has also been reported in a MEMRI-study of cathepsin D-deficient mice (Haapanen et al., 2007). Moreover, the agreement between activated microglia and increased ME in our study was further supported by two animals that showed low density of activated microglia and almost no ME in the thalamus. However, one animal showed little ME with a high density of activated microglia, but this may be explained by reduced absorption or distribution of $MnCl_2$, for instance if the IP injection went into the gut or bladder or by differences in slice thickness and resolution between histology and MR-image slices or partial volume effects on MRI. Furthermore, the increase in ME from day 1 till day 7 was paralleled by the increase in activated microglia/macrophages, especially in the dorsolateral thalamus. This suggests that the appearance of increased ME in injured areas 7 days after HI and $MnCl_2$ injection could be explained by accumulation of Mn^{2+} in microglia/macrophages rather than specific uptake into dying neurons.

Increased manganese-enhancement may represent accumulation in phagocytes

Reactive astrocytes, activated microglia and macrophages all have the capability of phagocytosis in the aftermath of brain injury (Ito et al., 2007). A hypothesis that could explain our histological and MRI results is that during the first days after the hypoxic–ischemic insult these cells phagocytose dead cells and cell debris containing small amounts of Mn^{2+} in the large areas of early injury, resulting in an accumulation of Mn^{2+} in the phagocytes with time. When the phagocytosing cells are no longer needed in the areas with early injury that have been cleared of dead cells and debris, they may

migrate to areas with delayed cell death — among these the dorsolateral thalamus. Arrival of numerous manganese-laden phagocytes to the injury areas of the thalamus would give high concentrations of Mn^{2+} and a localized T_1-shortening effect on MRI and may hence explain the late increased ME and the high concentrations of activated microglia we observe on day 7.

Circulating macrophages that are also stained by anti-CD68 antibody have a peak infiltration of the injury site between 3 and 6 days after brain ischemia (Schilling et al., 2003; Tanaka et al., 2003; Ohno et al., 1994). These cells may have taken up Mn^{2+} while in the blood stream and contributed to the increased ME on day 7 that coincides well with their late infiltration. Since $MnCl_2$ is rapidly cleared from the circulating blood volume after a systemic injection, at least in the adult rat (Zheng et al., 2000), such an accumulation of Mn^{2+} in circulating macrophages must most likely have occurred during the first day after injection. Based on the estimates from Zheng et al. and assuming the approximately same kinetics for an IP injection of 40 mg/kg, the calculated time to return to baseline level of Mn^{2+} in our rat pups could be approximately 16 h. However, whether the pharmacokinetics of $MnCl_2$ after systemic injection is the same in the neonatal as the adult rat is unknown, and this needs further investigation.

Possible active uptake of Mn^{2+} one week after hypoxia–ischemia

Rapid clearance of Mn^{2+} from the blood makes any active uptake directly from the blood into the brain one week after the injection seem unlikely. However, to investigate whether the ME we observed on day 7 after HI and $MnCl_2$ injection could be due to active uptake at the time, we injected $MnCl_2$ IP in 3 animals on day 6 after HI (not previously injected with $MnCl_2$) and imaged them repeatedly during the following week. Increased signal around the edge of the injury area of the dorsolateral thalamus was seen on day 7, progressing towards a more uniformly increased signal in the whole injury area during the following days (Fig. 5). Since free Mn^{2+} or protein bound Mn^{2+} diffuses very rapidly across liquids, it is unlikely that the increasing ME from the edge to the centre of the area could be explained by passive diffusion of Mn^{2+}. These results therefore indicate that there may be a small active uptake in the area around day 7 and during the following week.

In a study by Fujioka et al., high signal was found on T_1-w-imaging in stroke areas after 1 week. They related this to increased induction of manganese superoxide dismutase (Mn-SOD) and glutamine synthetase (GS) in reactive astrocytes in the injured area (Fujioka et al., 2003). Increased induction of Mn-SOD occurring one week after a focal cortical lesion has been reported by another study (Bidmon et al., 1998). In our study, reactive astrocytes were found in the areas of ME alongside the activated microglia and could therefore be involved in an active Mn^{2+} uptake around one week after hypoxia–ischemia. Induction of GS and Mn-SOD in astrocytes and neurons seen after hypoxia–ischemia in the brain (Gunter et al., 2006; Takeda, 2003; Lindenau et al., 2000; Wedler and Denman, 1984) can be further potentiated by the release of free-oxygen radicals and glutamate from activated microglia in these areas and hence contribute to the late ME seen in this study. However, the increased signal intensity and the ME in animals on day 6 (HI+Mn6) never reached the level observed in animals injected 6 h after HI (HI+Mn). This suggests that the ME seen on day 7 in HI+Mn pups is mostly due to a steady accumulation of Mn^{2+} during the 7 days after injection, probably by activated microglia/macrophages, rather than an active uptake around day 7.

Reduction of T_2 is not only related to manganese

In both HI+Mn and HI+Vehicle pups there were reduced T_2-values in the thalamus of the injured hemisphere compared to the contralateral hemisphere. This reduction is contrary to previous studies which have found normal or increased T_2-levels in ischemic areas (Meng et al., 2006; Wegener et al., 2006). However, the results might be explained by the large injury that our pups suffered, as large injuries may lead to hemorrhagic infarctions and small bleeding in the tissue with subsequent iron deposits in phagocytes giving a T_2-reduction and T_2*-effect (Weber et al., 2005). Furthermore, the T_2 among HI+Mn pups was more reduced compared to the HI+Vehicle pups. Some of this reduction could be explained by a T_2-effect caused by the high concentration of Mn^{2+} in the area (Silva et al., 2004). There was a good co-localization of T_2-reduction and increased signal intensity on T_1-weighted images in the dorsolateral thalamus on visual examination (Fig. 6), where the pixel-wise comparison showed a quantified match of 53%. The lack of a complete match on pixel-wise analysis may in part be accounted for by differences in geometric distortions of the T_1- and T_2-sequences, partial volume effects and uncertainty in the geometric co-localization of images. The overlapping areas of ME and T_2-reduction are however interesting and although it is outside the scope of this study, a possible interpretation is that it may represent an interaction between iron and Mn^{2+}-uptake by astrocytes through up-regulation of divalent metal transporter (DMT-1) as previously reported in another setting (Erikson and Aschner, 2006).

Future and clinical implications

This study has shown that manganese-enhanced MRI (MEMRI) may be a useful tool in future studies to follow the cellular development of brain injury and detecting inflammatory processes related to delayed neuronal death over time in the newborn animal. Furthermore, MEMRI may also be utilised to evaluate the effect of anti-inflammatory treatments of hypoxic–ischemic injury in the neonatal brain *in vivo*. The results of this study suggest that late ME may be related specifically to inflammatory processes rather than cell death. Whether increased ME can be seen in relation to inflammation in other disease models without massive cell death remains to be investigated. However, MEMRI may prove to be a valuable tool to detect and follow brain inflammation in other disease models as well. It should be stressed that comparison of the MRI to histological examinations is mandatory to be able to interpret the specificity of ME in a given animal model.

Clinical use of MEMRI is still limited by safety issues concerning cardio- and neurotoxic effects of high dose manganese. Although our study was not designed for addressing this issue, no adverse effects of $MnCl_2$ were observed among the pups. In the future, use of low dose Mn^{2+} or Mn^{2+}-chelates as contrast agent for MEMRI of brain in human patients may become a reality when the safety of such applications has been established. *In vivo* high-resolution images of inflammation in human brains would be extremely valuable in investigating a number of different diseases including stroke and neurodegenerative diseases such as Alzheimer's.

Conclusions

During the first days after hypoxia–ischemia, there was no increased manganese-enhancement detected on MRI in areas of massive neuronal death in the injured hemisphere. Therefore, the method of MEMRI used in this study does not seem applicable for depiction of neuronal death per se. However, late increased manganese-enhancement was shown in brain areas with delayed neuronal death and inflammation seven days after hypoxia–ischemia. The areas with late manganese-enhancement corresponded best with areas with high concentrations of activated microglia on immunohistochemistry. The late manganese-enhancement may therefore be related to accumulation of manganese in activated microglia. However, other cell types may be involved and further studies are needed to reveal the specific mechanisms causing the late manganese-enhancement.

Acknowledgments

The authors would like to thank FUGE Molecular Imaging Center for technical support and use of imaging facilities. We would also thank Frank van Bel and Floris Groenendal at the University Medical Center Utrecht for help with the animal model, planning the study and valuable discussion of the results. This study was financially supported by a grant from the Medical Faculty at Norwegian University of Science and Technology.

References

Ankarcrona, M., Dypbukt, J.M., Bonfoco, E., Zhivotovsky, B., Orrenius, S., Lipton, S.A., Nicotera, P., 1995. Glutamate-induced neuronal death: a succession of necrosis or apoptosis depending on mitochondrial function. Neuron 15, 961–973.

Aoki, I., Ebisu, T., Tanaka, C., Katsuta, K., Fujikawa, A., Umeda, M., Fukunaga, M., Takegami, T., Shapiro, E.M., Naruse, S., 2003. Detection of the anoxic depolarization of focal ischemia using manganese enhanced MRI. Magn. Reson. Med. 50, 7–12.

Aoki, I., Naruse, S., Tanaka, C., 2004. Manganese-enhanced magnetic resonance imaging (MEMRI) of brain activity and applications to early detection of brain ischemia. NMR Biomed. 17, 569–580.

Bidmon, H.J., Kato, K., Schleicher, A., Witte, O.W., Zilles, K., Traystman, R.J., 1998. Transient increase of manganese–superoxide dismutase in remote brain areas after focal photothrombotic cortical lesion. Stroke 29, 203–211.

Erikson, K.M., Aschner, M., 2006. Increased manganese uptake by primary astrocyte cultures with altered iron status is mediated primarily by divalent metal transporter. Neurotoxicology 27, 125–130.

Ferriero, D.M., 2004. Neonatal brain injury. N. Engl. J. Med. 351, 1985–1995.

Fujioka, M., Taoka, T., Matsuo, Y., Mishima, K., Ogoshi, K., Kondo, Y., Tsuda, M., Fujiwara, M., Asano, T., Sakaki, T., Miyasaki, A., Park, D., Siesjo, B.K., 2003. Magnetic resonance imaging shows delayed ischemic striatal neurodegeneration. Ann. Neurol. 54, 732–747.

Geddes, R., Vannucci, R.C., Vannucci, S.J., 2001. Delayed cerebral atrophy following moderate hypoxia–ischemia in the immature rat. Dev. Neurosci., 23, 180–185.

Gonzalez, R.C., Woods, R.E., Eddins, S.L., 2004. Digital Image Processing Using Matlab. Pearson Education Inc., Pearson Prentice Hall, Upper Saddle River, New Jersey, USA.

Gunter, T.E., Gavin, C.E., Aschner, M., Gunter, K.K., 2006. Speciation of manganese in cells and mitochondria: a search for the proximal cause of manganese neurotoxicity. Neurotoxocology 27, 765–776.

Haapanen, A., Ramadan, U.A., Autti, T., Joensuu, R., Tyynelä, J., 2007. In vivo MRI reveals the dynamics of pathological changes in the brains of cathepsin D-deficient mice and correlates changes in manganese-enhanced MRI with microglial activation. Magn. Reson. Imag. 25, 1024–1031.

Ito, U., Nagasao, J., Kawakami, E., Oyanagi, K., 2007. Fate of disseminated dead neurons in the cortical ischemic penumbra. Ultrastructure indicating a novel scavenger mechanism of microglia and astrocytes. Stroke 38, 2577–2583.

Kristián, T., Siesjö, B.K., 1998. Calcium in ischemic cell death. Stroke 29, 705–718.

Koretsky, A.P., Silva, A.C., 2004. Manganese-enhanced magnetic resonance imaging (MEMRI). NMR Biomed. 17, 527–531.

Kuo, Y.T., Herlihy, A.H., So, P.W., Bhakoo, K.K., Bell, J.D., 2005. In vivo measurement of T1 relaxation times in mouse brain associated with different modes of systemic administration of manganese chloride. J. Magn. Reson. Imag. 21, 334–339.

Lindenau, J., Noack, H., Possel, H., Asayama, K., Wolf, G., 2000. Cellular distribution of superoxide dismutases in the rat CNS. Glia 29, 25–34.

McLean, C., Ferriero, D., 2004. Mechanisms of hypoxic–ischemic injury in the term infant. Semin. Perinatol. 28, 425–432.

McRae, A., Gilland, E., Bona, E., Hagberg, H., 1995. Microglia activation after neonatal hypoxic–ischemia. Dev. Brain Res. 84, 245–252.

Meng, S., Qiao, M., Scobie, K., Tomanek, B., Tuor, U.I., 2006. Evolution of magnetic resonance imaging changes associated with cerebral hypoxia–ischemia and a relatively selective white matter injury in neonatal rats. Pediatr. Res. 59, 554–559.

Nakajima, W., Ishida, A., Lange, M.S., Gabrielson, K.L., Wilson, M.A., Martin, L.J., Blue, M. E., Johnston, M.V., 2000. Apoptosis has a prolonged role in the neurodegeneration after hypoxic ischemia in the newborn rat. J. Neurosci. 20, 7994–8004.

Northington, F.J., Ferriero, D.M., Graham, E.M., Traystman, R.J., Martin, L.J., 2001. Early neurodegeneration after hypoxia–ischemia in neonatal rat is necrosis while delayed neuronal death is apoptosis. Neurobiol. Dis. 8, 207–219.

Northington, F.J., Graham, E.M., Martin, L.J., 2005. Apoptosis in perinatal hypoxic–ischemic brain injury: how important is it and should it be inhibited? Brain. Res. Brain. Res. Rev. 50, 244–257.

Ohno, M., Aotani, H., Shimada, M., 1994. Glial responses to hypoxic/ischemic encephalopathy in neonatal rat cerebrum. Dev. Brain. Res. 84, 294–298.

Paxinos, G., Watson, C., 1998. The Rat Brain in Stereotaxic Coordinates, 4th ed. Academic Press, San Diego, CA.

Qiao, M., Latta, P., Meng, S., Tomanek, B., Tuor, U.I., 2004. Development of acute edema following cerebral hypoxia–ischemia in neonatal compared with juvenile rats using magnetic resonance imaging. Pediatr Res. 55, 101–106.

Rice, J.E., Vannucci, R.C., Brierley, J.B., 1981. The influence of immaturity on hypoxic–ischemic brain damage in the rat. Ann. Neurol. 9, 131–141.

Schilling, M., Besselmann, M., Leonhard, C., Mueller, M., Ringelstein, E.B., Kiefer, R., 2003. Microglial activation precedes and predominates over macrophage infiltration in transient focal cerebral ischemia: a study in green fluorescent protein transgenic bone marrow chimeric mice. Exp. Neurol. 183, 25–33.

Silva, A.C., Lee, J.H., Aoki, I., Koretsky, A.P., 2004. Manganese-enhanced magnetic resonance imaging (MEMRI): methodological and practical considerations. NMR Biomed. 17, 532–543.

de Sousa, P.L., de Souza, S.L., Silva, A.C., de Souza, R.E., de Castro, R.M., 2007. Manganese-enhanced magnetic resonance imaging (MEMRI) of rat brain after systemic administration of MnCl2: changes in T1 relaxation times during postnatal development. J. Magn. Reson. Imag. 25, 32–38.

Takeda, A., 2003. Manganese action in brain function. Brain. Res. Brain. Res. Rev. 41, 79–87.

Tanaka, R., Komine-Kobayashi, M., Mochizuki, H., et al., 2003. Migration of enhanced green fluorescent protein expressing bone marrow-derived microglia/macrophage into the mouse brain following permanent focal ischemia. Neuroscience 117, 531–539.

Vannucci, S.J., Hagberg, H., 2004. Hypoxia–ischemia in the immature brain. J. Experim. Biol. 207, 3149–3154.

Vannucci, R.C., Perlman, J.M., 1997. Interventions for perinatal hypoxic–ischemic encephalopathy. Pediatrics 100, 1004–1014.

Vannucci, R.C., Vannucci, S.J., 2005. Perinatal hypoxic–ischemic brain damage: evolution of an animal model. Dev. Neurosci. 27, 81–86.

Wadghiri, Y.Z., Blind, J.A., Duan, X., Moreno, C., Yu, X., Joyner, A.L., Turnbull, D.H., 2004. Manganese-enhanced magnetic resonance imaging (MEMRI) of mouse brain development. NMR Biomed. 17, 613–619.

Watanabe, T., Natt, O., Boretius, S., Frahm, J., Michaelis, T., 2002. In vivo 3D MRI staining of mouse brain after subcutaneous application of $MnCl_2$. Magn. Reson. Med. 48, 852–859.

Wedler, F., Denman, R., 1984. Glutamine synthetase: the major Mn(II) enzyme in mammalian brain. Curr. Top. Cell. Regul. 24, 153–169.

Weber, R., Wegener, S., Ramos-Cabrer, P., Wiedermann, D., Hoehn, M., 2005. MRI detection of macrophage activity after experimental stroke in rats: new indicators for late appearance of vascular degradation? Magn. Reson. Med. 54, 59–66.

Wegener, S., Weber, R., Ramos-Cabrer, P., Uhlenkueken, U., Sprenger, C., Wiedermann, D., Villringer, A., Hoehn, M., 2006. Temporal profile of T2-weighted MRI distinguishes between pannecrosis and selective neuronal death after transient focal cerebral ischemia in the rat. J. Cereb. Blood Flow Metab. 26, 38–47.

Won, S.J., Kim, D.Y., Gwag, B.J., 2002. Cellular and molecular pathways of ischemic neuronal death. J. Biochem. Mol. Biol. 35, 67–86.

Zheng, W., Kim, H., Zhao, Q., 2000. Comparative toxicokinetics of manganese chloride and methylcyclopentadienyl manganese tricarbonyl (MMT) in Sprague–Dawley rats. Toxicol. Sci. 54, 295–301.

Dissertations at the Faculty of Medicine, NTNU

1977

1. Knut Joachim Berg: EFFECT OF ACETYLSALICYLIC ACID ON RENAL FUNCTION
2. Karl Erik Viken and Arne Ødegaard: STUDIES ON HUMAN MONOCYTES CULTURED *IN VITRO*

1978

3. Karel Bjørn Cyvin: CONGENITAL DISLOCATION OF THE HIP JOINT.
4. Alf O. Brubakk: METHODS FOR STUDYING FLOW DYNAMICS IN THE LEFT VENTRICLE AND THE AORTA IN MAN.

1979

5. Geirmund Unsgaard: CYTOSTATIC AND IMMUNOREGULATORY ABILITIES OF HUMAN BLOOD MONOCYTES CULTURED IN VITRO

1980

6. Størker Jørstad: URAEMIC TOXINS
7. Arne Olav Jenssen: SOME RHEOLOGICAL, CHEMICAL AND STRUCTURAL PROPERTIES OF MUCOID SPUTUM FROM PATIENTS WITH CHRONIC OBSTRUCTIVE BRONCHITIS

1981

8. Jens Hammerstrøm: CYTOSTATIC AND CYTOLYTIC ACTIVITY OF HUMAN MONOCYTES AND EFFUSION MACROPHAGES AGAINST TUMOR CELLS *IN VITRO*

1983

9. Tore Syversen: EFFECTS OF METHYLMERCURY ON RAT BRAIN PROTEIN.
10. Torbjørn Iversen: SQUAMOUS CELL CARCINOMA OF THE VULVA.

1984

11. Tor-Erik Widerøe: ASPECTS OF CONTINUOUS AMBULATORY PERITONEAL DIALYSIS.
12. Anton Hole: ALTERATIONS OF MONOCYTE AND LYMPHOCYTE FUNCTIONS IN REALTION TO SURGERY UNDER EPIDURAL OR GENERAL ANAESTHESIA.
13. Terje Terjesen: FRACTURE HEALING AND STRESS-PROTECTION AFTER METAL PLATE FIXATION AND EXTERNAL FIXATION.
14. Carsten Saunte: CLUSTER HEADACHE SYNDROME.
15. Inggard Lereim: TRAFFIC ACCIDENTS AND THEIR CONSEQUENCES.
16. Bjørn Magne Eggen: STUDIES IN CYTOTOXICITY IN HUMAN ADHERENT MONONUCLEAR BLOOD CELLS.
17. Trond Haug: FACTORS REGULATING BEHAVIORAL EFFECTS OG DRUGS.

1985

18. Sven Erik Gisvold: RESUSCITATION AFTER COMPLETE GLOBAL BRAIN ISCHEMIA.
19. Terje Espevik: THE CYTOSKELETON OF HUMAN MONOCYTES.
20. Lars Bevanger: STUDIES OF THE Ibc (c) PROTEIN ANTIGENS OF GROUP B STREPTOCOCCI.
21. Ole-Jan Iversen: RETROVIRUS-LIKE PARTICLES IN THE PATHOGENESIS OF PSORIASIS.
22. Lasse Eriksen: EVALUATION AND TREATMENT OF ALCOHOL DEPENDENT BEHAVIOUR.
23. Per I. Lundmo: ANDROGEN METABOLISM IN THE PROSTATE.

1986

24. Dagfinn Berntzen: ANALYSIS AND MANAGEMENT OF EXPERIMENTAL AND CLINICAL PAIN.
25. Odd Arnold Kildahl-Andersen: PRODUCTION AND CHARACTERIZATION OF MONOCYTE-DERIVED CYTOTOXIN AND ITS ROLE IN MONOCYTE-MEDIATED CYTOTOXICITY.
26. Ola Dale: VOLATILE ANAESTHETICS.

1987

27. Per Martin Kleveland: STUDIES ON GASTRIN.
28. Audun N. Øksendal: THE CALCIUM PARADOX AND THE HEART.
29. Vilhjalmur R. Finsen: HIP FRACTURES

1988

30. Rigmor Austgulen: TUMOR NECROSIS FACTOR: A MONOCYTE-DERIVED REGULATOR OF CELLULAR GROWTH.
31. Tom-Harald Edna: HEAD INJURIES ADMITTED TO HOSPITAL.
32. Joseph D. Borsi: NEW ASPECTS OF THE CLINICAL PHARMACOKINETICS OF METHOTREXATE.
33. Olav F. M. Sellevold: GLUCOCORTICOIDS IN MYOCARDIAL PROTECTION.
34. Terje Skjærpe: NONINVASIVE QUANTITATION OF GLOBAL PARAMETERS ON LEFT VENTRICULAR FUNCTION: THE SYSTOLIC PULMONARY ARTERY PRESSURE AND CARDIAC OUTPUT.
35. Eyvind Rødahl: STUDIES OF IMMUNE COMPLEXES AND RETROVIRUS-LIKE ANTIGENS IN PATIENTS WITH ANKYLOSING SPONDYLITIS.
36. Ketil Thorstensen: STUDIES ON THE MECHANISMS OF CELLULAR UPTAKE OF IRON FROM TRANSFERRIN.
37. Anna Midelfart: STUDIES OF THE MECHANISMS OF ION AND FLUID TRANSPORT IN THE BOVINE CORNEA.
38. Eirik Helseth: GROWTH AND PLASMINOGEN ACTIVATOR ACTIVITY OF HUMAN GLIOMAS AND BRAIN METASTASES - WITH SPECIAL REFERENCE TO TRANSFORMING GROWTH FACTOR BETA AND THE EPIDERMAL GROWTH FACTOR RECEPTOR.
39. Petter C. Borchgrevink: MAGNESIUM AND THE ISCHEMIC HEART.
40. Kjell-Arne Rein: THE EFFECT OF EXTRACORPOREAL CIRCULATION ON SUBCUTANEOUS TRANSCAPILLARY FLUID BALANCE.
41. Arne Kristian Sandvik: RAT GASTRIC HISTAMINE.
42. Carl Bredo Dahl: ANIMAL MODELS IN PSYCHIATRY.

1989

43. Torbjørn A. Fredriksen: CERVICOGENIC HEADACHE.
44. Rolf A. Walstad: CEFTAZIDIME.
45. Rolf Salvesen: THE PUPIL IN CLUSTER HEADACHE.
46. Nils Petter Jørgensen: DRUG EXPOSURE IN EARLY PREGNANCY.
47. Johan C. Ræder: PREMEDICATION AND GENERAL ANAESTHESIA IN OUTPATIENT GYNECOLOGICAL SURGERY.
48. M. R. Shalaby: IMMUNOREGULATORY PROPERTIES OF TNF-α AND THE RELATED CYTOKINES.
49. Anders Waage: THE COMPLEX PATTERN OF CYTOKINES IN SEPTIC SHOCK.
50. Bjarne Christian Eriksen: ELECTROSTIMULATION OF THE PELVIC FLOOR IN FEMALE URINARY INCONTINENCE.
51. Tore B. Halvorsen: PROGNOSTIC FACTORS IN COLORECTAL CANCER.

1990

52. Asbjørn Nordby: CELLULAR TOXICITY OF ROENTGEN CONTRAST MEDIA.
53. Kåre E. Tvedt: X-RAY MICROANALYSIS OF BIOLOGICAL MATERIAL.
54. Tore C. Stiles: COGNITIVE VULNERABILITY FACTORS IN THE DEVELOPMENT AND MAINTENANCE OF DEPRESSION.
55. Eva Hofsli: TUMOR NECROSIS FACTOR AND MULTIDRUG RESISTANCE.
56. Helge S. Haarstad: TROPHIC EFFECTS OF CHOLECYSTOKININ AND SECRETIN ON THE RAT PANCREAS.
57. Lars Engebretsen: TREATMENT OF ACUTE ANTERIOR CRUCIATE LIGAMENT INJURIES.
58. Tarjei Rygnestad: DELIBERATE SELF-POISONING IN TRONDHEIM.
59. Arne Z. Henriksen: STUDIES ON CONSERVED ANTIGENIC DOMAINS ON MAJOR OUTER MEMBRANE PROTEINS FROM ENTEROBACTERIA.
60. Steinar Westin: UNEMPLOYMENT AND HEALTH: Medical and social consequences of a factory closure in a ten-year controlled follow-up study.
61. Ylva Sahlin: INJURY REGISTRATION, a tool for accident preventive work.
62. Helge Bjørnstad Pettersen: BIOSYNTHESIS OF COMPLEMENT BY HUMAN ALVEOLAR MACROPHAGES WITH SPECIAL REFERENCE TO SARCOIDOSIS.
63. Berit Schei: TRAPPED IN PAINFUL LOVE.
64. Lars J. Vatten: PROSPECTIVE STUDIES OF THE RISK OF BREAST CANCER IN A COHORT OF NORWEGIAN WOMAN.

1991

65. Kåre Bergh: APPLICATIONS OF ANTI-C5a SPECIFIC MONOCLONAL ANTIBODIES FOR THE ASSESSMENT OF COMPLEMENT ACTIVATION.
66. Svein Svenningsen: THE CLINICAL SIGNIFICANCE OF INCREASED FEMORAL ANTEVERSION.
67. Olbjørn Klepp: NONSEMINOMATOUS GERM CELL TESTIS CANCER: THERAPEUTIC OUTCOME AND PROGNOSTIC FACTORS.
68. Trond Sand: THE EFFECTS OF CLICK POLARITY ON BRAINSTEM AUDITORY EVOKED POTENTIALS AMPLITUDE, DISPERSION, AND LATENCY VARIABLES.
69. Kjetil B. Åsbakk: STUDIES OF A PROTEIN FROM PSORIATIC SCALE, PSO P27, WITH RESPECT TO ITS POTENTIAL ROLE IN IMMUNE REACTIONS IN PSORIASIS.
70. Arnulf Hestnes: STUDIES ON DOWN´S SYNDROME.
71. Randi Nygaard: LONG-TERM SURVIVAL IN CHILDHOOD LEUKEMIA.
72. Bjørn Hagen: THIO-TEPA.
73. Svein Anda: EVALUATION OF THE HIP JOINT BY COMPUTED TOMOGRAMPHY AND ULTRASONOGRAPHY.

1992

74. Martin Svartberg: AN INVESTIGATION OF PROCESS AND OUTCOME OF SHORT-TERM PSYCHODYNAMIC PSYCHOTHERAPY.
75. Stig Arild Slørdahl: AORTIC REGURGITATION.
76. Harold C Sexton: STUDIES RELATING TO THE TREATMENT OF SYMPTOMATIC NON-PSYCHOTIC PATIENTS.
77. Maurice B. Vincent: VASOACTIVE PEPTIDES IN THE OCULAR/FOREHEAD AREA.
78. Terje Johannessen: CONTROLLED TRIALS IN SINGLE SUBJECTS.
79. Turid Nilsen: PYROPHOSPHATE IN HEPATOCYTE IRON METABOLISM.
80. Olav Haraldseth: NMR SPECTROSCOPY OF CEREBRAL ISCHEMIA AND REPERFUSION IN RAT.
81. Eiliv Brenna: REGULATION OF FUNCTION AND GROWTH OF THE OXYNTIC MUCOSA.

1993

82. Gunnar Bovim: CERVICOGENIC HEADACHE.
83. Jarl Arne Kahn: ASSISTED PROCREATION.
84. Bjørn Naume: IMMUNOREGULATORY EFFECTS OF CYTOKINES ON NK CELLS.
85. Rune Wiseth: AORTIC VALVE REPLACEMENT.
86. Jie Ming Shen: BLOOD FLOW VELOCITY AND RESPIRATORY STUDIES.
87. Piotr Kruszewski: SUNCT SYNDROME WITH SPECIAL REFERENCE TO THE AUTONOMIC NERVOUS SYSTEM.
88. Mette Haase Moen: ENDOMETRIOSIS.
89. Anne Vik: VASCULAR GAS EMBOLISM DURING AIR INFUSION AND AFTER DECOMPRESSION IN PIGS.
90. Lars Jacob Stovner: THE CHIARI TYPE I MALFORMATION.
91. Kjell Å. Salvesen: ROUTINE ULTRASONOGRAPHY IN UTERO AND DEVELOPMENT IN CHILDHOOD.

1994

92. Nina-Beate Liabakk: DEVELOPMENT OF IMMUNOASSAYS FOR TNF AND ITS SOLUBLE RECEPTORS.
93. Sverre Helge Torp: *erb*B ONCOGENES IN HUMAN GLIOMAS AND MENINGIOMAS.
94. Olav M. Linaker: MENTAL RETARDATION AND PSYCHIATRY. Past and present.
95. Per Oscar Feet: INCREASED ANTIDEPRESSANT AND ANTIPANIC EFFECT IN COMBINED TREATMENT WITH DIXYRAZINE AND TRICYCLIC ANTIDEPRESSANTS.
96. Stein Olav Samstad: CROSS SECTIONAL FLOW VELOCITY PROFILES FROM TWO-DIMENSIONAL DOPPLER ULTRASOUND: Studies on early mitral blood flow.
97. Bjørn Backe: STUDIES IN ANTENATAL CARE.
98. Gerd Inger Ringdal: QUALITY OF LIFE IN CANCER PATIENTS.
99. Torvid Kiserud: THE DUCTUS VENOSUS IN THE HUMAN FETUS.
100. Hans E. Fjøsne: HORMONAL REGULATION OF PROSTATIC METABOLISM.
101. Eylert Brodtkorb: CLINICAL ASPECTS OF EPILEPSY IN THE MENTALLY RETARDED.
102. Roar Juul: PEPTIDERGIC MECHANISMS IN HUMAN SUBARACHNOID HEMORRHAGE.
103. Unni Syversen: CHROMOGRANIN A. Phsysiological and Clinical Role.

1995

104. Odd Gunnar Brakstad: THERMOSTABLE NUCLEASE AND THE *nuc* GENE IN THE DIAGNOSIS OF *Staphylococcus aureus* INFECTIONS.
105. Terje Engan: NUCLEAR MAGNETIC RESONANCE (NMR) SPECTROSCOPY OF PLASMA IN MALIGNANT DISEASE.
106. Kirsten Rasmussen: VIOLENCE IN THE MENTALLY DISORDERED.
107. Finn Egil Skjeldestad: INDUCED ABORTION: Timetrends and Determinants.
108. Roar Stenseth: THORACIC EPIDURAL ANALGESIA IN AORTOCORONARY BYPASS SURGERY.
109. Arild Faxvaag: STUDIES OF IMMUNE CELL FUNCTION *in mice infected with* MURINE RETROVIRUS.

1996

110. Svend Aakhus: NONINVASIVE COMPUTERIZED ASSESSMENT OF LEFT VENTRICULAR FUNCTION AND SYSTEMIC ARTERIAL PROPERTIES. Methodology and some clinical applications.
111. Klaus-Dieter Bolz: INTRAVASCULAR ULTRASONOGRAPHY.
112. Petter Aadahl: CARDIOVASCULAR EFFECTS OF THORACIC AORTIC CROSS-CLAMPING.
113. Sigurd Steinshamn: CYTOKINE MEDIATORS DURING GRANULOCYTOPENIC INFECTIONS.
114. Hans Stifoss-Hanssen: SEEKING MEANING OR HAPPINESS?
115. Anne Kvikstad: LIFE CHANGE EVENTS AND MARITAL STATUS IN RELATION TO RISK AND PROGNOSIS OF CANCER.
116. Torbjørn Grøntvedt: TREATMENT OF ACUTE AND CHRONIC ANTERIOR CRUCIATE LIGAMENT INJURIES. A clinical and biomechanical study.
117. Sigrid Hørven Wigers: CLINICAL STUDIES OF FIBROMYALGIA WITH FOCUS ON ETIOLOGY, TREATMENT AND OUTCOME.
118. Jan Schjøtt: MYOCARDIAL PROTECTION: Functional and Metabolic Characteristics of Two Endogenous Protective Principles.
119. Marit Martinussen: STUDIES OF INTESTINAL BLOOD FLOW AND ITS RELATION TO TRANSITIONAL CIRCULATORY ADAPATION IN NEWBORN INFANTS.
120. Tomm B. Müller: MAGNETIC RESONANCE IMAGING IN FOCAL CEREBRAL ISCHEMIA.
121. Rune Haaverstad: OEDEMA FORMATION OF THE LOWER EXTREMITIES.
122. Magne Børset: THE ROLE OF CYTOKINES IN MULTIPLE MYELOMA, WITH SPECIAL REFERENCE TO HEPATOCYTE GROWTH FACTOR.
123. Geir Smedslund: A THEORETICAL AND EMPIRICAL INVESTIGATION OF SMOKING, STRESS AND DISEASE: RESULTS FROM A POPULATION SURVEY.

1997

124. Torstein Vik: GROWTH, MORBIDITY, AND PSYCHOMOTOR DEVELOPMENT IN INFANTS WHO WERE GROWTH RETARDED *IN UTERO*.
125. Siri Forsmo: ASPECTS AND CONSEQUENCES OF OPPORTUNISTIC SCREENING FOR CERVICAL CANCER. Results based on data from three Norwegian counties.
126. Jon S. Skranes: CEREBRAL MRI AND NEURODEVELOPMENTAL OUTCOME IN VERY LOW BIRTH WEIGHT (VLBW) CHILDREN. A follow-up study of a geographically based year cohort of VLBW children at ages one and six years.
127. Knut Bjørnstad: COMPUTERIZED ECHOCARDIOGRAPHY FOR EVALUTION OF CORONARY ARTERY DISEASE.
128. Grethe Elisabeth Borchgrevink: DIAGNOSIS AND TREATMENT OF WHIPLASH/NECK SPRAIN INJURIES CAUSED BY CAR ACCIDENTS.
129. Tor Elsås: NEUROPEPTIDES AND NITRIC OXIDE SYNTHASE IN OCULAR AUTONOMIC AND SENSORY NERVES.
130. Rolf W. Gråwe: EPIDEMIOLOGICAL AND NEUROPSYCHOLOGICAL PERSPECTIVES ON SCHIZOPHRENIA.
131. Tonje Strømholm: CEREBRAL HAEMODYNAMICS DURING THORACIC AORTIC CROSSCLAMPING. An experimental study in pigs.

1998

132. Martinus Bråten: STUDIES ON SOME PROBLEMS REALTED TO INTRAMEDULLARY NAILING OF FEMORAL FRACTURES.
133. Ståle Nordgård: PROLIFERATIVE ACTIVITY AND DNA CONTENT AS PROGNOSTIC INDICATORS IN ADENOID CYSTIC CARCINOMA OF THE HEAD AND NECK.

134. Egil Lien: SOLUBLE RECEPTORS FOR **TNF** AND **LPS**: RELEASE PATTERN AND POSSIBLE SIGNIFICANCE IN DISEASE.
135. Marit Bjørgaas: HYPOGLYCAEMIA IN CHILDREN WITH DIABETES MELLITUS
136. Frank Skorpen: GENETIC AND FUNCTIONAL ANALYSES OF DNA REPAIR IN HUMAN CELLS.
137. Juan A. Pareja: SUNCT SYNDROME. ON THE CLINICAL PICTURE. ITS DISTINCTION FROM OTHER, SIMILAR HEADACHES.
138. Anders Angelsen: NEUROENDOCRINE CELLS IN HUMAN PROSTATIC CARCINOMAS AND THE PROSTATIC COMPLEX OF RAT, GUINEA PIG, CAT AND DOG.
139. Fabio Antonaci: CHRONIC PAROXYSMAL HEMICRANIA AND HEMICRANIA CONTINUA: TWO DIFFERENT ENTITIES?
140. Sven M. Carlsen: ENDOCRINE AND METABOLIC EFFECTS OF METFORMIN WITH SPECIAL EMPHASIS ON CARDIOVASCULAR RISK FACTORES.

1999

141. Terje A. Murberg: DEPRESSIVE SYMPTOMS AND COPING AMONG PATIENTS WITH CONGESTIVE HEART FAILURE.
142. Harm-Gerd Karl Blaas: THE EMBRYONIC EXAMINATION. Ultrasound studies on the development of the human embryo.
143. Noèmi Becser Andersen:THE CEPHALIC SENSORY NERVES IN UNILATERAL HEADACHES. Anatomical background and neurophysiological evaluation.
144. Eli-Janne Fiskerstrand: LASER TREATMENT OF PORT WINE STAINS. A study of the efficacy and limitations of the pulsed dye laser. Clinical and morfological analyses aimed at improving the therapeutic outcome.
145. Bård Kulseng: A STUDY OF ALGINATE CAPSULE PROPERTIES AND CYTOKINES IN RELATION TO INSULIN DEPENDENT DIABETES MELLITUS.
146. Terje Haug: STRUCTURE AND REGULATION OF THE HUMAN UNG GENE ENCODING URACIL-DNA GLYCOSYLASE.
147. Heidi Brurok: MANGANESE AND THE HEART. A Magic Metal with Diagnostic and Therapeutic Possibilites.
148. Agnes Kathrine Lie: DIAGNOSIS AND PREVALENCE OF HUMAN PAPILLOMAVIRUS INFECTION IN CERVICAL INTRAEPITELIAL NEOPLASIA. Relationship to Cell Cycle Regulatory Proteins and HLA DQBI Genes.
149. Ronald Mårvik: PHARMACOLOGICAL, PHYSIOLOGICAL AND PATHOPHYSIOLOGICAL STUDIES ON ISOLATED STOMACS.
150. Ketil Jarl Holen: THE ROLE OF ULTRASONOGRAPHY IN THE DIAGNOSIS AND TREATMENT OF HIP DYSPLASIA IN NEWBORNS.
151. Irene Hetlevik: THE ROLE OF CLINICAL GUIDELINES IN CARDIOVASCULAR RISK INTERVENTION IN GENERAL PRACTICE.
152. Katarina Tunòn: ULTRASOUND AND PREDICTION OF GESTATIONAL AGE.
153. Johannes Soma: INTERACTION BETWEEN THE LEFT VENTRICLE AND THE SYSTEMIC ARTERIES.
154. Arild Aamodt: DEVELOPMENT AND PRE-CLINICAL EVALUATION OF A CUSTOM-MADE FEMORAL STEM.
155. Agnar Tegnander: DIAGNOSIS AND FOLLOW-UP OF CHILDREN WITH SUSPECTED OR KNOWN HIP DYSPLASIA.
156. Bent Indredavik: STROKE UNIT TREATMENT: SHORT AND LONG-TERM EFFECTS
157. Jolanta Vanagaite Vingen: PHOTOPHOBIA AND PHONOPHOBIA IN PRIMARY HEADACHES

2000

158. Ola Dalsegg Sæther: PATHOPHYSIOLOGY DURING PROXIMAL AORTIC CROSS-CLAMPING CLINICAL AND EXPERIMENTAL STUDIES
159. xxxxxxxxx (blind number)
160. Christina Vogt Isaksen: PRENATAL ULTRASOUND AND POSTMORTEM FINDINGS – A TEN YEAR CORRELATIVE STUDY OF FETUSES AND INFANTS WITH DEVELOPMENTAL ANOMALIES.
161. Holger Seidel: HIGH-DOSE METHOTREXATE THERAPY IN CHILDREN WITH ACUTE LYMPHOCYTIC LEUKEMIA: DOSE, CONCENTRATION, AND EFFECT CONSIDERATIONS.
162. Stein Hallan: IMPLEMENTATION OF MODERN MEDICAL DECISION ANALYSIS INTO CLINICAL DIAGNOSIS AND TREATMENT.

163. Malcolm Sue-Chu: INVASIVE AND NON-INVASIVE STUDIES IN CROSS-COUNTRY SKIERS WITH ASTHMA-LIKE SYMPTOMS.
164. Ole-Lars Brekke: EFFECTS OF ANTIOXIDANTS AND FATTY ACIDS ON TUMOR NECROSIS FACTOR-INDUCED CYTOTOXICITY.
165. Jan Lundbom: AORTOCORONARY BYPASS SURGERY: CLINICAL ASPECTS, COST CONSIDERATIONS AND WORKING ABILITY.
166. John-Anker Zwart: LUMBAR NERVE ROOT COMPRESSION, BIOCHEMICAL AND NEUROPHYSIOLOGICAL ASPECTS.
167. Geir Falck: HYPEROSMOLALITY AND THE HEART.
168. Eirik Skogvoll: CARDIAC ARREST Incidence, Intervention and Outcome.
169. Dalius Bansevicius: SHOULDER-NECK REGION IN CERTAIN HEADACHES AND CHRONIC PAIN SYNDROMES.
170. Bettina Kinge: REFRACTIVE ERRORS AND BIOMETRIC CHANGES AMONG UNIVERSITY STUDENTS IN NORWAY.
171. Gunnar Qvigstad: CONSEQUENCES OF HYPERGASTRINEMIA IN MAN
172. Hanne Ellekjær: EPIDEMIOLOGICAL STUDIES OF STROKE IN A NORWEGIAN POPULATION. INCIDENCE, RISK FACTORS AND PROGNOSIS
173. Hilde Grimstad: VIOLENCE AGAINST WOMEN AND PREGNANCY OUTCOME.
174. Astrid Hjelde: SURFACE TENSION AND COMPLEMENT ACTIVATION: Factors influencing bubble formation and bubble effects after decompression.
175. Kjell A. Kvistad: MR IN BREAST CANCER – A CLINICAL STUDY.
176. Ivar Rossvoll: ELECTIVE ORTHOPAEDIC SURGERY IN A DEFINED POPULATION. Studies on demand, waiting time for treatment and incapacity for work.
177. Carina Seidel: PROGNOSTIC VALUE AND BIOLOGICAL EFFECTS OF HEPATOCYTE GROWTH FACTOR AND SYNDECAN-1 IN MULTIPLE MYELOMA.

2001

178. Alexander Wahba: THE INFLUENCE OF CARDIOPULMONARY BYPASS ON PLATELET FUNCTION AND BLOOD COAGULATION – DETERMINANTS AND CLINICAL CONSEQUENSES
179. Marcus Schmitt-Egenolf: THE RELEVANCE OF THE MAJOR hISTOCOMPATIBILITY COMPLEX FOR THE GENETICS OF PSORIASIS
180. Odrun Arna Gederaas: BIOLOGICAL MECHANISMS INVOLVED IN 5-AMINOLEVULINIC ACID BASED PHOTODYNAMIC THERAPY
181. Pål Richard Romundstad: CANCER INCIDENCE AMONG NORWEGIAN ALUMINIUM WORKERS
182. Henrik Hjorth-Hansen: NOVEL CYTOKINES IN GROWTH CONTROL AND BONE DISEASE OF MULTIPLE MYELOMA
183. Gunnar Morken: SEASONAL VARIATION OF HUMAN MOOD AND BEHAVIOUR
184. Bjørn Olav Haugen: MEASUREMENT OF CARDIAC OUTPUT AND STUDIES OF VELOCITY PROFILES IN AORTIC AND MITRAL FLOW USING TWO- AND THREE-DIMENSIONAL COLOUR FLOW IMAGING
185. Geir Bråthen: THE CLASSIFICATION AND CLINICAL DIAGNOSIS OF ALCOHOL-RELATED SEIZURES
186. Knut Ivar Aasarød: RENAL INVOLVEMENT IN INFLAMMATORY RHEUMATIC DISEASE. A Study of Renal Disease in Wegener's Granulomatosis and in Primary Sjögren's Syndrome
187. Trude Helen Flo: RESEPTORS INVOLVED IN CELL ACTIVATION BY DEFINED URONIC ACID POLYMERS AND BACTERIAL COMPONENTS
188. Bodil Kavli: HUMAN URACIL-DNA GLYCOSYLASES FROM THE UNG GENE: STRUCTRUAL BASIS FOR SUBSTRATE SPECIFICITY AND REPAIR
189. Liv Thommesen: MOLECULAR MECHANISMS INVOLVED IN TNF- AND GASTRIN-MEDIATED GENE REGULATION
190. Turid Lingaas Holmen: SMOKING AND HEALTH IN ADOLESCENCE; THE NORD-TRØNDELAG HEALTH STUDY, 1995-97
191. Øyvind Hjertner: MULTIPLE MYELOMA: INTERACTIONS BETWEEN MALIGNANT PLASMA CELLS AND THE BONE MICROENVIRONMENT
192. Asbjørn Støylen: STRAIN RATE IMAGING OF THE LEFT VENTRICLE BY ULTRASOUND. FEASIBILITY, CLINICAL VALIDATION AND PHYSIOLOGICAL ASPECTS

193. Kristian Midthjell: DIABETES IN ADULTS IN NORD-TRØNDELAG. PUBLIC HEALTH ASPECTS OF DIABETES MELLITUS IN A LARGE, NON-SELECTED NORWEGIAN POPULATION.
194. Guanglin Cui: FUNCTIONAL ASPECTS OF THE ECL CELL IN RODENTS
195. Ulrik Wisløff: CARDIAC EFFECTS OF AEROBIC ENDURANCE TRAINING: HYPERTROPHY, CONTRACTILITY AND CALCUIM HANDLING IN NORMAL AND FAILING HEART
196. Øyvind Halaas: MECHANISMS OF IMMUNOMODULATION AND CELL-MEDIATED CYTOTOXICITY INDUCED BY BACTERIAL PRODUCTS
197. Tore Amundsen: PERFUSION MR IMAGING IN THE DIAGNOSIS OF PULMONARY EMBOLISM
198. Nanna Kurtze: THE SIGNIFICANCE OF ANXIETY AND DEPRESSION IN FATIQUE AND PATTERNS OF PAIN AMONG INDIVIDUALS DIAGNOSED WITH FIBROMYALGIA: RELATIONS WITH QUALITY OF LIFE, FUNCTIONAL DISABILITY, LIFESTYLE, EMPLOYMENT STATUS, CO-MORBIDITY AND GENDER
199. Tom Ivar Lund Nilsen: PROSPECTIVE STUDIES OF CANCER RISK IN NORD-TRØNDELAG: THE HUNT STUDY. Associations with anthropometric, socioeconomic, and lifestyle risk factors
200. Asta Kristine Håberg: A NEW APPROACH TO THE STUDY OF MIDDLE CEREBRAL ARTERY OCCLUSION IN THE RAT USING MAGNETIC RESONANCE TECHNIQUES

2002

201. Knut Jørgen Arntzen: PREGNANCY AND CYTOKINES
202. Henrik Døllner: INFLAMMATORY MEDIATORS IN PERINATAL INFECTIONS
203. Asta Bye: LOW FAT, LOW LACTOSE DIET USED AS PROPHYLACTIC TREATMENT OF ACUTE INTESTINAL REACTIONS DURING PELVIC RADIOTHERAPY. A PROSPECTIVE RANDOMISED STUDY.
204. Sylvester Moyo: STUDIES ON STREPTOCOCCUS AGALACTIAE (GROUP B STREPTOCOCCUS) SURFACE-ANCHORED MARKERS WITH EMPHASIS ON STRAINS AND HUMAN SERA FROM ZIMBABWE.
205. Knut Hagen: HEAD-HUNT: THE EPIDEMIOLOGY OF HEADACHE IN NORD-TRØNDELAG
206. Li Lixin: ON THE REGULATION AND ROLE OF UNCOUPLING PROTEIN-2 IN INSULIN PRODUCING ß-CELLS
207. Anne Hildur Henriksen: SYMPTOMS OF ALLERGY AND ASTHMA VERSUS MARKERS OF LOWER AIRWAY INFLAMMATION AMONG ADOLESCENTS
208. Egil Andreas Fors: NON-MALIGNANT PAIN IN RELATION TO PSYCHOLOGICAL AND ENVIRONTENTAL FACTORS. EXPERIENTAL AND CLINICAL STUDES OF PAIN WITH FOCUS ON FIBROMYALGIA
209. Pål Klepstad: MORPHINE FOR CANCER PAIN
210. Ingunn Bakke: MECHANISMS AND CONSEQUENCES OF PEROXISOME PROLIFERATOR-INDUCED HYPERFUNCTION OF THE RAT GASTRIN PRODUCING CELL
211. Ingrid Susann Gribbestad: MAGNETIC RESONANCE IMAGING AND SPECTROSCOPY OF BREAST CANCER
212. Rønnaug Astri Ødegård: PREECLAMPSIA – MATERNAL RISK FACTORS AND FETAL GROWTH
213. Johan Haux: STUDIES ON CYTOTOXICITY INDUCED BY HUMAN NATURAL KILLER CELLS AND DIGITOXIN
214. Turid Suzanne Berg-Nielsen: PARENTING PRACTICES AND MENTALLY DISORDERED ADOLESCENTS
215. Astrid Rydning: BLOOD FLOW AS A PROTECTIVE FACTOR FOR THE STOMACH MUCOSA. AN EXPERIMENTAL STUDY ON THE ROLE OF MAST CELLS AND SENSORY AFFERENT NEURONS

2003

216. Jan Pål Loennechen: HEART FAILURE AFTER MYOCARDIAL INFARCTION. Regional Differences, Myocyte Function, Gene Expression, and Response to Cariporide, Losartan, and Exercise Training.
217. Elisabeth Qvigstad: EFFECTS OF FATTY ACIDS AND OVER-STIMULATION ON INSULIN SECRETION IN MAN

218. Arne Åsberg: EPIDEMIOLOGICAL STUDIES IN HEREDITARY HEMOCHROMATOSIS: PREVALENCE, MORBIDITY AND BENEFIT OF SCREENING.
219. Johan Fredrik Skomsvoll: REPRODUCTIVE OUTCOME IN WOMEN WITH RHEUMATIC DISEASE. A population registry based study of the effects of inflammatory rheumatic disease and connective tissue disease on reproductive outcome in Norwegian women in 1967-1995.
220. Siv Mørkved: URINARY INCONTINENCE DURING PREGNANCY AND AFTER DELIVERY: EFFECT OF PELVIC FLOOR MUSCLE TRAINING IN PREVENTION AND TREATMENT
221. Marit S. Jordhøy: THE IMPACT OF COMPREHENSIVE PALLIATIVE CARE
222. Tom Christian Martinsen: HYPERGASTRINEMIA AND HYPOACIDITY IN RODENTS – CAUSES AND CONSEQUENCES
223. Solveig Tingulstad: CENTRALIZATION OF PRIMARY SURGERY FOR OVARAIN CANCER. FEASIBILITY AND IMPACT ON SURVIVAL
224. Haytham Eloqayli: METABOLIC CHANGES IN THE BRAIN CAUSED BY EPILEPTIC SEIZURES
225. Torunn Bruland: STUDIES OF EARLY RETROVIRUS-HOST INTERACTIONS – VIRAL DETERMINANTS FOR PATHOGENESIS AND THE INFLUENCE OF SEX ON THE SUSCEPTIBILITY TO FRIEND MURINE LEUKAEMIA VIRUS INFECTION
226. Torstein Hole: DOPPLER ECHOCARDIOGRAPHIC EVALUATION OF LEFT VENTRICULAR FUNCTION IN PATIENTS WITH ACUTE MYOCARDIAL INFARCTION
227. Vibeke Nossum: THE EFFECT OF VASCULAR BUBBLES ON ENDOTHELIAL FUNCTION
228. Sigurd Fasting: ROUTINE BASED RECORDING OF ADVERSE EVENTS DURING ANAESTHESIA – APPLICATION IN QUALITY IMPROVEMENT AND SAFETY
229. Solfrid Romundstad: EPIDEMIOLOGICAL STUDIES OF MICROALBUMINURIA. THE NORD-TRØNDELAG HEALTH STUDY 1995-97 (HUNT 2)
230. Geir Torheim: PROCESSING OF DYNAMIC DATA SETS IN MAGNETIC RESONANCE IMAGING
231. Catrine Ahlén: SKIN INFECTIONS IN OCCUPATIONAL SATURATION DIVERS IN THE NORTH SEA AND THE IMPACT OF THE ENVIRONMENT
232. Arnulf Langhammer: RESPIRATORY SYMPTOMS, LUNG FUNCTION AND BONE MINERAL DENSITY IN A COMPREHENSIVE POPULATION SURVEY. THE NORD-TRØNDELAG HEALTH STUDY 1995-97. THE BRONCHIAL OBSTRUCTION IN NORD-TRØNDELAG STUDY
233. Einar Kjelsås: EATING DISORDERS AND PHYSICAL ACTIVITY IN NON-CLINICAL SAMPLES
234. Arne Wibe: RECTAL CANCER TREATMENT IN NORWAY – STANDARDISATION OF SURGERY AND QUALITY ASSURANCE

2004

235. Eivind Witsø: BONE GRAFT AS AN ANTIBIOTIC CARRIER
236. Anne Mari Sund: DEVELOPMENT OF DEPRESSIVE SYMPTOMS IN EARLY ADOLESCENCE
237. Hallvard Lærum: EVALUATION OF ELECTRONIC MEDICAL RECORDS – A CLINICAL TASK PERSPECTIVE
238. Gustav Mikkelsen: ACCESSIBILITY OF INFORMATION IN ELECTRONIC PATIENT RECORDS; AN EVALUATION OF THE ROLE OF DATA QUALITY
239. Steinar Krokstad: SOCIOECONOMIC INEQUALITIES IN HEALTH AND DISABILITY. SOCIAL EPIDEMIOLOGY IN THE NORD-TRØNDELAG HEALTH STUDY (HUNT), NORWAY
240. Arne Kristian Myhre: NORMAL VARIATION IN ANOGENITAL ANATOMY AND MICROBIOLOGY IN NON-ABUSED PRESCHOOL CHILDREN
241. Ingunn Dybedal: NEGATIVE REGULATORS OF HEMATOPOIETEC STEM AND PROGENITOR CELLS
242. Beate Sitter: TISSUE CHARACTERIZATION BY HIGH RESOLUTION MAGIC ANGLE SPINNING MR SPECTROSCOPY
243. Per Arne Aas: MACROMOLECULAR MAINTENANCE IN HUMAN CELLS – REPAIR OF URACIL IN DNA AND METHYLATIONS IN DNA AND RNA
244. Anna Bofin: FINE NEEDLE ASPIRATION CYTOLOGY IN THE PRIMARY INVESTIGATION OF BREAST TUMOURS AND IN THE DETERMINATION OF TREATMENT STRATEGIES

245. Jim Aage Nøttestad: DEINSTITUTIONALIZATION AND MENTAL HEALTH CHANGES AMONG PEOPLE WITH MENTAL RETARDATION
246. Reidar Fossmark: GASTRIC CANCER IN JAPANESE COTTON RATS
247. Wibeke Nordhøy: MANGANESE AND THE HEART, INTRACELLULAR MR RELAXATION AND WATER EXCHANGE ACROSS THE CARDIAC CELL MEMBRANE

2005

248. Sturla Molden: QUANTITATIVE ANALYSES OF SINGLE UNITS RECORDED FROM THE HIPPOCAMPUS AND ENTORHINAL CORTEX OF BEHAVING RATS
249. Wenche Brenne Drøyvold: EPIDEMIOLOGICAL STUDIES ON WEIGHT CHANGE AND HEALTH IN A LARGE POPULATION. THE NORD-TRØNDELAG HEALTH STUDY (HUNT)
250. Ragnhild Støen: ENDOTHELIUM-DEPENDENT VASODILATION IN THE FEMORAL ARTERY OF DEVELOPING PIGLETS
251. Aslak Steinsbekk: HOMEOPATHY IN THE PREVENTION OF UPPER RESPIRATORY TRACT INFECTIONS IN CHILDREN
252. Hill-Aina Steffenach: MEMORY IN HIPPOCAMPAL AND CORTICO-HIPPOCAMPAL CIRCUITS
253. Eystein Stordal: ASPECTS OF THE EPIDEMIOLOGY OF DEPRESSIONS BASED ON SELF-RATING IN A LARGE GENERAL HEALTH STUDY (THE HUNT-2 STUDY)
254. Viggo Pettersen: FROM MUSCLES TO SINGING: THE ACTIVITY OF ACCESSORY BREATHING MUSCLES AND THORAX MOVEMENT IN CLASSICAL SINGING
255. Marianne Fyhn: SPATIAL MAPS IN THE HIPPOCAMPUS AND ENTORHINAL CORTEX
256. Robert Valderhaug: OBSESSIVE-COMPULSIVE DISORDER AMONG CHILDREN AND ADOLESCENTS: CHARACTERISTICS AND PSYCHOLOGICAL MANAGEMENT OF PATIENTS IN OUTPATIENT PSYCHIATRIC CLINICS
257. Erik Skaaheim Haug: INFRARENAL ABDOMINAL AORTIC ANEURYSMS – COMORBIDITY AND RESULTS FOLLOWING OPEN SURGERY
258. Daniel Kondziella: GLIAL-NEURONAL INTERACTIONS IN EXPERIMENTAL BRAIN DISORDERS
259. Vegard Heimly Brun: ROUTES TO SPATIAL MEMORY IN HIPPOCAMPAL PLACE CELLS
260. Kenneth McMillan: PHYSIOLOGICAL ASSESSMENT AND TRAINING OF ENDURANCE AND STRENGTH IN PROFESSIONAL YOUTH SOCCER PLAYERS
261. Marit Sæbø Indredavik: MENTAL HEALTH AND CEREBRAL MAGNETIC RESONANCE IMAGING IN ADOLESCENTS WITH LOW BIRTH WEIGHT
262. Ole Johan Kemi: ON THE CELLULAR BASIS OF AEROBIC FITNESS, INTENSITY-DEPENDENCE AND TIME-COURSE OF CARDIOMYOCYTE AND ENDOTHELIAL ADAPTATIONS TO EXERCISE TRAINING
263. Eszter Vanky: POLYCYSTIC OVARY SYNDROME – METFORMIN TREATMENT IN PREGNANCY
264. Hild Fjærtoft: EXTENDED STROKE UNIT SERVICE AND EARLY SUPPORTED DISCHARGE. SHORT AND LONG-TERM EFFECTS
265. Grete Dyb: POSTTRAUMATIC STRESS REACTIONS IN CHILDREN AND ADOLESCENTS
266. Vidar Fykse: SOMATOSTATIN AND THE STOMACH
267. Kirsti Berg: OXIDATIVE STRESS AND THE ISCHEMIC HEART: A STUDY IN PATIENTS UNDERGOING CORONARY REVASCULARIZATION
268. Björn Inge Gustafsson: THE SEROTONIN PRODUCING ENTEROCHROMAFFIN CELL, AND EFFECTS OF HYPERSEROTONINEMIA ON HEART AND BONE

2006

269. Torstein Baade Rø: EFFECTS OF BONE MORPHOGENETIC PROTEINS, HEPATOCYTE GROWTH FACTOR AND INTERLEUKIN-21 IN MULTIPLE MYELOMA
270. May-Britt Tessem: METABOLIC EFFECTS OF ULTRAVIOLET RADIATION ON THE ANTERIOR PART OF THE EYE
271. Anne-Sofie Helvik: COPING AND EVERYDAY LIFE IN A POPULATION OF ADULTS WITH HEARING IMPAIRMENT
272. Therese Standal: MULTIPLE MYELOMA: THE INTERPLAY BETWEEN MALIGNANT PLASMA CELLS AND THE BONE MARROW MICROENVIRONMENT

273. Ingvild Saltvedt: TREATMENT OF ACUTELY SICK, FRAIL ELDERLY PATIENTS IN A GERIATRIC EVALUATION AND MANAGEMENT UNIT – RESULTS FROM A PROSPECTIVE RANDOMISED TRIAL
274. Birger Henning Endreseth: STRATEGIES IN RECTAL CANCER TREATMENT – FOCUS ON EARLY RECTAL CANCER AND THE INFLUENCE OF AGE ON PROGNOSIS
275. Anne Mari Aukan Rokstad: ALGINATE CAPSULES AS BIOREACTORS FOR CELL THERAPY
276. Mansour Akbari: HUMAN BASE EXCISION REPAIR FOR PRESERVATION OF GENOMIC STABILITY
277. Stein Sundstrøm: IMPROVING TREATMENT IN PATIENTS WITH LUNG CANCER – RESULTS FROM TWO MULITCENTRE RANDOMISED STUDIES
278. Hilde Pleym: BLEEDING AFTER CORONARY ARTERY BYPASS SURGERY - STUDIES ON HEMOSTATIC MECHANISMS, PROPHYLACTIC DRUG TREATMENT AND EFFECTS OF AUTOTRANSFUSION
279. Line Merethe Oldervoll: PHYSICAL ACTIVITY AND EXERCISE INTERVENTIONS IN CANCER PATIENTS
280. Boye Welde: THE SIGNIFICANCE OF ENDURANCE TRAINING, RESISTANCE TRAINING AND MOTIVATIONAL STYLES IN ATHLETIC PERFORMANCE AMONG ELITE JUNIOR CROSS-COUNTRY SKIERS
281. Per Olav Vandvik: IRRITABLE BOWEL SYNDROME IN NORWAY, STUDIES OF PREVALENCE, DIAGNOSIS AND CHARACTERISTICS IN GENERAL PRACTICE AND IN THE POPULATION
282. Idar Kirkeby-Garstad: CLINICAL PHYSIOLOGY OF EARLY MOBILIZATION AFTER CARDIAC SURGERY
283. Linn Getz: SUSTAINABLE AND RESPONSIBLE PREVENTIVE MEDICINE. CONCEPTUALISING ETHICAL DILEMMAS ARISING FROM CLINICAL IMPLEMENTATION OF ADVANCING MEDICAL TECHNOLOGY
284. Eva Tegnander: DETECTION OF CONGENITAL HEART DEFECTS IN A NON-SELECTED POPULATION OF 42,381 FETUSES
285. Kristin Gabestad Nørsett: GENE EXPRESSION STUDIES IN GASTROINTESTINAL PATHOPHYSIOLOGY AND NEOPLASIA
286. Per Magnus Haram: GENETIC VS. AQUIRED FITNESS: METABOLIC, VASCULAR AND CARDIOMYOCYTE ADAPTATIONS
287. Agneta Johansson: GENERAL RISK FACTORS FOR GAMBLING PROBLEMS AND THE PREVALENCE OF PATHOLOGICAL GAMBLING IN NORWAY
288. Svein Artur Jensen: THE PREVALENCE OF SYMPTOMATIC ARTERIAL DISEASE OF THE LOWER LIMB
289. Charlotte Björk Ingul: QUANITIFICATION OF REGIONAL MYOCARDIAL FUNCTION BY STRAIN RATE AND STRAIN FOR EVALUATION OF CORONARY ARTERY DISEASE. AUTOMATED VERSUS MANUAL ANALYSIS DURING ACUTE MYOCARDIAL INFARCTION AND DOBUTAMINE STRESS ECHOCARDIOGRAPHY
290. Jakob Nakling: RESULTS AND CONSEQUENCES OF ROUTINE ULTRASOUND SCREENING IN PREGNANCY – A GEOGRAPHIC BASED POPULATION STUDY
291. Anne Engum: DEPRESSION AND ANXIETY – THEIR RELATIONS TO THYROID DYSFUNCTION AND DIABETES IN A LARGE EPIDEMIOLOGICAL STUDY
292. Ottar Bjerkeset: ANXIETY AND DEPRESSION IN THE GENERAL POPULATION: RISK FACTORS, INTERVENTION AND OUTCOME – THE NORD-TRØNDELAG HEALTH STUDY (HUNT)
293. Jon Olav Drogset: RESULTS AFTER SURGICAL TREATMENT OF ANTERIOR CRUCIATE LIGAMENT INJURIES – A CLINICAL STUDY
294. Lars Fosse: MECHANICAL BEHAVIOUR OF COMPACTED MORSELLISED BONE – AN EXPERIMENTAL IN VITRO STUDY
295. Gunilla Klensmeden Fosse: MENTAL HEALTH OF PSYCHIATRIC OUTPATIENTS BULLIED IN CHILDHOOD
296. Paul Jarle Mork: MUSCLE ACTIVITY IN WORK AND LEISURE AND ITS ASSOCIATION TO MUSCULOSKELETAL PAIN
297. Björn Stenström: LESSONS FROM RODENTS: I: MECHANISMS OF OBESITY SURGERY – ROLE OF STOMACH. II: CARCINOGENIC EFFECTS OF *HELICOBACTER PYLORI* AND SNUS IN THE STOMACH

2007

298. Haakon R. Skogseth: INVASIVE PROPERTIES OF CANCER – A TREATMENT TARGET ? IN VITRO STUDIES IN HUMAN PROSTATE CANCER CELL LINES
299. Janniche Hammer: GLUTAMATE METABOLISM AND CYCLING IN MESIAL TEMPORAL LOBE EPILEPSY
300. May Britt Drugli: YOUNG CHILDREN TREATED BECAUSE OF ODD/CD: CONDUCT PROBLEMS AND SOCIAL COMPETENCIES IN DAY-CARE AND SCHOOL SETTINGS
301. Arne Skjold: MAGNETIC RESONANCE KINETICS OF MANGANESE DIPYRIDOXYL DIPHOSPHATE (MnDPDP) IN HUMAN MYOCARDIUM. STUDIES IN HEALTHY VOLUNTEERS AND IN PATIENTS WITH RECENT MYOCARDIAL INFARCTION
302. Siri Malm: LEFT VENTRICULAR SYSTOLIC FUNCTION AND MYOCARDIAL PERFUSION ASSESSED BY CONTRAST ECHOCARDIOGRAPHY
303. Valentina Maria do Rosario Cabral Iversen: MENTAL HEALTH AND PSYCHOLOGICAL ADAPTATION OF CLINICAL AND NON-CLINICAL MIGRANT GROUPS
304. Lasse Løvstakken: SIGNAL PROCESSING IN DIAGNOSTIC ULTRASOUND: ALGORITHMS FOR REAL-TIME ESTIMATION AND VISUALIZATION OF BLOOD FLOW VELOCITY
305. Elisabeth Olstad: GLUTAMATE AND GABA: MAJOR PLAYERS IN NEURONAL METABOLISM
306. Lilian Leistad: THE ROLE OF CYTOKINES AND PHOSPHOLIPASE A_2s IN ARTICULAR CARTILAGE CHONDROCYTES IN RHEUMATOID ARTHRITIS AND OSTEOARTHRITIS
307. Arne Vaaler: EFFECTS OF PSYCHIATRIC INTENSIVE CARE UNIT IN AN ACUTE PSYCIATHRIC WARD
308. Mathias Toft: GENETIC STUDIES OF LRRK2 AND PINK1 IN PARKINSON'S DISEASE
309. Ingrid Løvold Mostad: IMPACT OF DIETARY FAT QUANTITY AND QUALITY IN TYPE 2 DIABETES WITH EMPHASIS ON MARINE N-3 FATTY ACIDS
310. Torill Eidhammer Sjøbakk: MR DETERMINED BRAIN METABOLIC PATTERN IN PATIENTS WITH BRAIN METASTASES AND ADOLESCENTS WITH LOW BIRTH WEIGHT
311. Vidar Beisvåg: PHYSIOLOGICAL GENOMICS OF HEART FAILURE: FROM TECHNOLOGY TO PHYSIOLOGY
312. Olav Magnus Søndenå Fredheim: HEALTH RELATED QUALITY OF LIFE ASSESSMENT AND ASPECTS OF THE CLINICAL PHARMACOLOGY OF METHADONE IN PATIENTS WITH CHRONIC NON-MALIGNANT PAIN
313. Anne Brantberg: FETAL AND PERINATAL IMPLICATIONS OF ANOMALIES IN THE GASTROINTESTINAL TRACT AND THE ABDOMINAL WALL
314. Erik Solligård: GUT LUMINAL MICRODIALYSIS
315. Elin Tollefsen: RESPIRATORY SYMPTOMS IN A COMPREHENSIVE POPULATION BASED STUDY AMONG ADOLESCENTS 13-19 YEARS. YOUNG-HUNT 1995-97 AND 2000-01; THE NORD-TRØNDELAG HEALTH STUDIES (HUNT)
316. Anne-Tove Brenne: GROWTH REGULATION OF MYELOMA CELLS
317. Heidi Knobel: FATIGUE IN CANCER TREATMENT – ASSESSMENT, COURSE AND ETIOLOGY
318. Torbjørn Dahl: CAROTID ARTERY STENOSIS. DIAGNOSTIC AND THERAPEUTIC ASPECTS
319. Inge-Andre Rasmussen jr.: FUNCTIONAL AND DIFFUSION TENSOR MAGNETIC RESONANCE IMAGING IN NEUROSURGICAL PATIENTS
320. Grete Helen Bratberg: PUBERTAL TIMING – ANTECEDENT TO RISK OR RESILIENCE ? EPIDEMIOLOGICAL STUDIES ON GROWTH, MATURATION AND HEALTH RISK BEHAVIOURS; THE YOUNG HUNT STUDY, NORD-TRØNDELAG, NORWAY
321. Sveinung Sørhaug: THE PULMONARY NEUROENDOCRINE SYSTEM. PHYSIOLOGICAL, PATHOLOGICAL AND TUMOURIGENIC ASPECTS
322. Olav Sande Eftedal: ULTRASONIC DETECTION OF DECOMPRESSION INDUCED VASCULAR MICROBUBBLES
323. Rune Bang Leistad: PAIN, AUTONOMIC ACTIVATION AND MUSCULAR ACTIVITY RELATED TO EXPERIMENTALLY-INDUCED COGNITIVE STRESS IN HEADACHE PATIENTS
324. Svein Brekke: TECHNIQUES FOR ENHANCEMENT OF TEMPORAL RESOLUTION IN THREE-DIMENSIONAL ECHOCARDIOGRAPHY
325. Kristian Bernhard Nilsen: AUTONOMIC ACTIVATION AND MUSCLE ACTIVITY IN RELATION TO MUSCULOSKELETAL PAIN

326. Anne Irene Hagen: HEREDITARY BREAST CANCER IN NORWAY. DETECTION AND PROGNOSIS OF BREAST CANCER IN FAMILIES WITH *BRCA1*GENE MUTATION
327. Ingebjørg S. Juel : INTESTINAL INJURY AND RECOVERY AFTER ISCHEMIA. AN EXPERIMENTAL STUDY ON RESTITUTION OF THE SURFACE EPITHELIUM, INTESTINAL PERMEABILITY, AND RELEASE OF BIOMARKERS FROM THE MUCOSA
328. Runa Heimstad: POST-TERM PREGNANCY
329. Jan Egil Afset: ROLE OF ENTEROPATHOGENIC *ESCHERICHIA COLI* IN CHILDHOOD DIARRHOEA IN NORWAY
330. Bent Håvard Hellum: *IN VITRO* INTERACTIONS BETWEEN MEDICINAL DRUGS AND HERBS ON CYTOCHROME P-450 METABOLISM AND P-GLYCOPROTEIN TRANSPORT
331. Morten André Høydal: CARDIAC DYSFUNCTION AND MAXIMAL OXYGEN UPTAKE MYOCARDIAL ADAPTATION TO ENDURANCE TRAINING

2008

332. Andreas Møllerløkken: REDUCTION OF VASCULAR BUBBLES: METHODS TO PREVENT THE ADVERSE EFFECTS OF DECOMPRESSION
333. Anne Hege Aamodt: COMORBIDITY OF HEADACHE AND MIGRAINE IN THE NORD-TRØNDELAG HEALTH STUDY 1995-97
334. Brage Høyem Amundsen: MYOCARDIAL FUNCTION QUANTIFIED BY SPECKLE TRACKING AND TISSUE DOPPLER ECHOCARDIOGRAPHY – VALIDATION AND APPLICATION IN EXERCISE TESTING AND TRAINING
335. Inger Anne Næss: INCIDENCE, MORTALITY AND RISK FACTORS OF FIRST VENOUS THROMBOSIS IN A GENERAL POPULATION. RESULTS FROM THE SECOND NORD-TRØNDELAG HEALTH STUDY (HUNT2)
336. Vegard Bugten: EFFECTS OF POSTOPERATIVE MEASURES AFTER FUNCTIONAL ENDOSCOPIC SINUS SURGERY
337. Morten Bruvold: MANGANESE AND WATER IN CARDIAC MAGNETIC RESONANCE IMAGING
338. Miroslav Fris: THE EFFECT OF SINGLE AND REPEATED ULTRAVIOLET RADIATION ON THE ANTERIOR SEGMENT OF THE RABBIT EYE
339. Svein Arne Aase: METHODS FOR IMPROVING QUALITY AND EFFICIENCY IN QUANTITATIVE ECHOCARDIOGRAPHY – ASPECTS OF USING HIGH FRAME RATE
340. Roger Almvik: ASSESSING THE RISK OF VIOLENCE: DEVELOPMENT AND VALIDATION OF THE BRØSET VIOLENCE CHECKLIST
341. Ottar Sundheim: STRUCTURE-FUNCTION ANALYSIS OF HUMAN ENZYMES INITIATING NUCLEOBASE REPAIR IN DNA AND RNA
342. Anne Mari Undheim: SHORT AND LONG-TERM OUTCOME OF EMOTIONAL AND BEHAVIOURAL PROBLEMS IN YOUNG ADOLESCENTS WITH AND WITHOUT READING DIFFICULTIES
343. Helge Garåsen: THE TRONDHEIM MODEL. IMPROVING THE PROFESSIONAL COMMUNICATION BETWEEN THE VARIOUS LEVELS OF HEALTH CARE SERVICES AND IMPLEMENTATION OF INTERMEDIATE CARE AT A COMMUNITY HOSPITAL COULD PROVIDE BETTER CARE FOR OLDER PATIENTS. SHORT AND LONG TERM EFFECTS
344. Olav A. Foss: "THE ROTATION RATIOS METHOD". A METHOD TO DESCRIBE ALTERED SPATIAL ORIENTATION IN SEQUENTIAL RADIOGRAPHS FROM ONE PELVIS
345. Bjørn Olav Åsvold: THYROID FUNCTION AND CARDIOVASCULAR HEALTH
346. Torun Margareta Melø: NEURONAL GLIAL INTERACTIONS IN EPILEPSY
347. Irina Poliakova Eide: FETAL GROWTH RESTRICTION AND PRE-ECLAMPSIA: SOME CHARACTERISTICS OF FETO-MATERNAL INTERACTIONS IN DECIDUA BASALIS
348. Torunn Askim: RECOVERY AFTER STROKE. ASSESSMENT AND TREATMENT; WITH FOCUS ON MOTOR FUNCTION
349. Ann Elisabeth Åsberg: NEUTROPHIL ACTIVATION IN A ROLLER PUMP MODEL OF CARDIOPULMONARY BYPASS. INFLUENCE ON BIOMATERIAL, PLATELETS AND COMPLEMENT
350. Lars Hagen: REGULATION OF DNA BASE EXCISION REPAIR BY PROTEIN INTERACTIONS AND POST TRANSLATIONAL MODIFICATIONS
351. Sigrun Beate Kjøtrød: POLYCYSTIC OVARY SYNDROME – METFORMIN TREATMENT IN ASSISTED REPRODUCTION

352. Steven Keita Nishiyama: PERSPECTIVES ON LIMB-VASCULAR HETEROGENEITY: IMPLICATIONS FOR HUMAN AGING, SEX, AND EXERCISE
353. Sven Peter Näsholm: ULTRASOUND BEAMS FOR ENHANCED IMAGE QUALITY
354. Jon Ståle Ritland: PRIMARY OPEN-ANGLE GLAUCOMA & EXFOLIATIVE GLAUCOMA. SURVIVAL, COMORBIDITY AND GENETICS
355. Sigrid Botne Sando: ALZHEIMER'S DISEASE IN CENTRAL NORWAY. GENETIC AND EDUCATIONAL ASPECTS
356. Parvinder Kaur: CELLULAR AND MOLECULAR MECHANISMS BEHIND METHYLMERCURY-INDUCED NEUROTOXICITY
357. Ismail Cüneyt Güzey: DOPAMINE AND SEROTONIN RECEPTOR AND TRANSPORTER GENE POLYMORPHISMS AND EXTRAPYRAMIDAL SYMPTOMS. STUDIES IN PARKINSON'S DISEASE AND IN PATIENTS TREATED WITH ANTIPSYCHOTIC OR ANTIDEPRESSANT DRUGS
358. Brit Dybdahl: EXTRA-CELLULAR INDUCIBLE HEAT-SHOCK PROTEIN 70 (Hsp70) – A ROLE IN THE INFLAMMATORY RESPONSE ?
359. Kristoffer Haugarvoll: IDENTIFYING GENETIC CAUSES OF PARKINSON'S DISEASE IN NORWAY
360. Nadra Nilsen: TOLL-LIKE RECEPTOR 2 –EXPRESSION, REGULATION AND SIGNALING
361. Johan Håkon Bjørngaard: PATIENT SATISFACTION WITH OUTPATIENT MENTAL HEALTH SERVICES – THE INFLUENCE OF ORGANIZATIONAL FACTORS.
362. Kjetil Høydal : EFFECTS OF HIGH INTENSITY AEROBIC TRAINING IN HEALTHY SUBJECTS AND CORONARY ARTERY DISEASE PATIENTS; THE IMPORTANCE OF INTENSITY,, DURATION AND FREQUENCY OF TRAINING.
363. Trine Karlsen: TRAINING IS MEDICINE: ENDURANCE AND STRENGTH TRAINING IN CORONARY ARTERY DISEASE AND HEALTH.
364. Marte Thuen: MANGANASE-ENHANCED AND DIFFUSION TENSOR MR IMAGING OF THE NORMAL, INJURED AND REGENERATING RAT VISUAL PATHWAY
365. Cathrine Broberg Vågbø: DIRECT REPAIR OF ALKYLATION DAMAGE IN DNA AND RNA BY 2-OXOGLUTARATE- AND IRON-DEPENDENT DIOXYGENASES
366. Arnt Erik Tjønna: AEROBIC EXERCISE AND CARDIOVASCULAR RISK FACTORS IN OVERWEIGHT AND OBESE ADOLESCENTS AND ADULTS
367. Marianne W. Furnes: FEEDING BEHAVIOR AND BODY WEIGHT DEVELOPMENT: LESSONS FROM RATS
368. Lene N. Johannessen: FUNGAL PRODUCTS AND INFLAMMATORY RESPONSES IN HUMAN MONOCYTES AND EPITHELIAL CELLS
369. Anja Bye: GENE EXPRESSION PROFILING OF *INHERITED* AND *ACQUIRED* MAXIMAL OXYGEN UPTAKE – RELATIONS TO THE METABOLIC SYNDROME.
370. Oluf Dimitri Røe: MALIGNANT MESOTHELIOMA: VIRUS, BIOMARKERS AND GENES. A TRANSLATIONAL APPROACH
371. Ane Cecilie Dale: DIABETES MELLITUS AND FATAL ISCHEMIC HEART DISEASE. ANALYSES FROM THE HUNT1 AND 2 STUDIES
372. Jacob Christian Hølen: PAIN ASSESSMENT IN PALLIATIVE CARE: VALIDATION OF METHODS FOR SELF-REPORT AND BEHAVIOURAL ASSESSMENT
373. Erming Tian: THE GENETIC IMPACTS IN THE ONCOGENESIS OF MULTIPLE MYELOMA
374. Ole Bosnes: KLINISK UTPRØVING AV NORSKE VERSJONER AV NOEN SENTRALE TESTER PÅ KOGNITIV FUNKSJON
375. Ola M. Rygh: 3D ULTRASOUND BASED NEURONAVIGATION IN NEUROSURGERY. A CLINICAL EVALUATION
376. Astrid Kamilla Stunes: ADIPOKINES, PEROXISOME PROFILERATOR ACTIVATED RECEPTOR (PPAR) AGONISTS AND SEROTONIN. COMMON REGULATORS OF BONE AND FAT METABOLISM
377. Silje Engdal: HERBAL REMEDIES USED BY NORWEGIAN CANCER PATIENTS AND THEIR ROLE IN HERB-DRUG INTERACTIONS
378. Kristin Offerdal: IMPROVED ULTRASOUND IMAGING OF THE FETUS AND ITS CONSEQUENCES FOR SEVERE AND LESS SEVERE ANOMALIES
379. Øivind Rognmo: HIGH-INTENSITY AEROBIC EXERCISE AND CARDIOVASCULAR HEALTH
380. Jo-Åsmund Lund: RADIOTHERAPY IN ANAL CARCINOMA AND PROSTATE CANCER

2009

381. Tore Grüner Bjåstad: HIGH FRAME RATE ULTRASOUND IMAGING USING PARALLEL BEAMFORMING
382. Erik Søndenaa: INTELLECTUAL DISABILITIES IN THE CRIMINAL JUSTICE SYSTEM
383. Berit Rostad: SOCIAL INEQUALITIES IN WOMEN'S HEALTH, HUNT 1984-86 AND 1995-97, THE NORD-TRØNDELAG HEALTH STUDY (HUNT)
384. Jonas Crosby: ULTRASOUND-BASED QUANTIFICATION OF MYOCARDIAL DEFORMATION AND ROTATION
385. Erling Tronvik: MIGRAINE, BLOOD PRESSURE AND THE RENIN-ANGIOTENSIN SYSTEM
386. Tom Christensen: BRINGING THE GP TO THE FOREFRONT OF EPR DEVELOPMENT
387. Håkon Bergseng: ASPECTS OF GROUP B STREPTOCOCCUS (GBS) DISEASE IN THE NEWBORN. EPIDEMIOLOGY, CHARACTERISATION OF INVASIVE STRAINS AND EVALUATION OF INTRAPARTUM SCREENING
388. Ronny Myhre: GENETIC STUDIES OF CANDIDATE TENE3S IN PARKINSON'S DISEASE
389. Torbjørn Moe Eggebø: ULTRASOUND AND LABOUR
390. Eivind Wang: TRAINING IS MEDICINE FOR PATIENTS WITH PERIPHERAL ARTERIAL DISEASE
391. Thea Kristin Våtsveen: GENETIC ABERRATIONS IN MYELOMA CELLS
392. Thomas Jozefiak: QUALITY OF LIFE AND MENTAL HEALTH IN CHILDREN AND ADOLESCENTS: CHILD AND PARENT PERSPECTIVES
393. Jens Erik Slagsvold: N-3 POLYUNSATURATED FATTY ACIDS IN HEALTH AND DISEASE – CLINICAL AND MOLECULAR ASPECTS
394. Kristine Misund: A STUDY OF THE TRANSCRIPTIONAL REPRESSOR ICER. REGULATORY NETWORKS IN GASTRIN-INDUCED GENE EXPRESSION
395. Franco M. Impellizzeri: HIGH-INTENSITY TRAINING IN FOOTBALL PLAYERS. EFFECTS ON PHYSICAL AND TECHNICAL PERFORMANCE
396. Kari Hanne Gjeilo: HEALTH-RELATED QUALITY OF LIFE AND CHRONIC PAIN IN PATIENTS UNDERGOING CARDIAC SURGERY
397. Øyvind Hauso: NEUROENDOCRINE ASPECTS OF PHYSIOLOGY AND DISEASE
398. Ingvild Bjellmo Johnsen: INTRACELLULAR SIGNALING MECHANISMS IN THE INNATE IMMUNE RESPONSE TO VIRAL INFECTIONS
399. Linda Tømmerdal Roten: GENETIC PREDISPOSITION FOR DEVELOPMENT OF PREEMCLAMPSIA – CANDIDATE GENE STUDIES IN THE HUNT (NORD-TRØNDELAG HEALTH STUDY) POPULATION
400. Trude Teoline Nausthaug Rakvåg: PHARMACOGENETICS OF MORPHINE IN CANCER PAIN
401. Hanne Lehn: MEMORY FUNCTIONS OF THE HUMAN MEDIAL TEMPORAL LOBE STUDIED WITH fMRI
402. Randi Utne Holt: ADHESION AND MIGRATION OF MYELOMA CELLS – IN VITRO STUDIES –
403. Trygve Solstad: NEURAL REPRESENTATIONS OF EUCLIDEAN SPACE
404. Unn-Merete Fagerli: MULTIPLE MYELOMA CELLS AND CYTOKINES FROM THE BONE MARROW ENVIRONMENT; ASPECTS OF GROWTH REGULATION AND MIGRATION
405. Sigrid Bjørnelv: EATING– AND WEIGHT PROBLEMS IN ADOLESCENTS, THE YOUNG HUNT-STUDY
406. Mari Hoff: CORTICAL HAND BONE LOSS IN RHEUMATOID ARTHRITIS. EVALUATING DIGITAL X-RAY RADIOGRAMMETRY AS OUTCOME MEASURE OF DISEASE ACTIVITY, RESPONSE VARIABLE TO TREATMENT AND PREDICTOR OF BONE DAMAGE
407. Siri Bjørgen: AEROBIC HIGH INTENSITY INTERVAL TRAINING IS AN EFFECTIVE TREATMENT FOR PATIENTS WITH CHRONIC OBSTRUCTIVE PULMONARY DISEASE
408. Susanne Lindqvist: VISION AND BRAIN IN ADOLESCENTS WITH LOW BIRTH WEIGHT
409. Torbjørn Hergum: 3D ULTRASOUND FOR QUANTITATIVE ECHOCARDIOGRAPHY
410. Jørgen Urnes: PATIENT EDUCATION IN GASTRO-OESOPHAGEAL REFLUX DISEASE. VALIDATION OF A DIGESTIVE SYMPTOMS AND IMPACT QUESTIONNAIRE AND A RANDOMISED CONTROLLED TRIAL OF PATIENT EDUCATION

411. Elvar Eyjolfsson: 13C NMRS OF ANIMAL MODELS OF SCHIZOPHRENIA
412. Marius Steiro Fimland: CHRONIC AND ACUTE NEURAL ADAPTATIONS TO STRENGTH TRAINING
413. Øyvind Støren: RUNNING AND CYCLING ECONOMY IN ATHLETES; DETERMINING FACTORS, TRAINING INTERVENTIONS AND TESTING
414. Håkon Hov: HEPATOCYTE GROWTH FACTOR AND ITS RECEPTOR C-MET. AUTOCRINE GROWTH AND SIGNALING IN MULTIPLE MYELOMA CELLS
415. Maria Radtke: ROLE OF AUTOIMMUNITY AND OVERSTIMULATION FOR BETA-CELL DEFICIENCY. EPIDEMIOLOGICAL AND THERAPEUTIC PERSPECTIVES
416. Liv Bente Romundstad: ASSISTED FERTILIZATION IN NORWAY: SAFETY OF THE REPRODUCTIVE TECHNOLOGY
417. Erik Magnus Berntsen: PREOPERATIV PLANNING AND FUNCTIONAL NEURONAVIGATION – WITH FUNCTIONAL MRI AND DIFFUSION TENSOR TRACTOGRAPHY IN PATIENTS WITH BRAIN LESIONS
418. Tonje Strømmen Steigedal: MOLECULAR MECHANISMS OF THE PROLIFERATIVE RESPONSE TO THE HORMONE GASTRIN
419. Vidar Rao: EXTRACORPOREAL PHOTOCHEMOTHERAPY IN PATIENTS WITH CUTANEOUS T CELL LYMPHOMA OR GRAFT-vs-HOST DISEASE
420. Torkild Visnes: DNA EXCISION REPAIR OF URACIL AND 5-FLUOROURACIL IN HUMAN CANCER CELL LINES

2010

421. John Munkhaugen: BLOOD PRESSURE, BODY WEIGHT, AND KIDNEY FUNCTION IN THE NEAR-NORMAL RANGE: NORMALITY, RISK FACTOR OR MORBIDITY ?
422. Ingrid Castberg: PHARMACOKINETICS, DRUG INTERACTIONS AND ADHERENCE TO TREATMENT WITH ANTIPSYCHOTICS: STUDIES IN A NATURALISTIC SETTING
423. Jian Xu: BLOOD-OXYGEN-LEVEL-DEPENDENT-FUNCTIONAL MAGNETIC RESONANCE IMAGING AND DIFFUSION TENSOR IMAGING IN TRAUMATIC BRAIN INJURY RESEARCH
424. Sigmund Simonsen: ACCEPTABLE RISK AND THE REQUIREMENT OF PROPORTIONALITY IN EUROPEAN BIOMEDICAL RESEARCH LAW. WHAT DOES THE REQUIREMENT THAT BIOMEDICAL RESEARCH SHALL NOT INVOLVE RISKS AND BURDENS DISPROPORTIONATE TO ITS POTENTIAL BENEFITS MEAN?
425. Astrid Woodhouse: MOTOR CONTROL IN WHIPLASH AND CHRONIC NON-TRAUMATIC NECK PAIN
426. Line Rørstad Jensen: EVALUATION OF TREATMENT EFFECTS IN CANCER BY MR IMAGING AND SPECTROSCOPY
427. Trine Moholdt: AEROBIC EXERCISE IN CORONARY HEART DISEASE
428. Øystein Olsen: ANALYSIS OF MANGANESE ENHANCED MRI OF THE NORMAL AND INJURED RAT CENTRAL NERVOUS SYSTEM